Supernova Neutrinos and a New Algorithm for Neutrino Transport

Adam Burrows[1], Timothy Young[1], Philip Pinto[1,2], Ron Eastman[2,3], and Todd Thompson[4]

burrows,tyoung,ppinto@as.arizona.edu, reastman@llnl.gov, thomp@physics.arizona.edu

ABSTRACT

We have developed a new implicit, multi–group, time–dependent, spherical neutrino transport algorithm based on the Feautrier variables, the tangent–ray method, and accelerated $\mathbf{\Lambda}$ iteration. The code achieves high angular resolution, is conceptually equivalent to a Boltzmann solver (without redshifts), and solves the transport equation exactly at all optical depths. We summarize and review the neutrino physics of stellar collapse and supernovae and our formulation of the relevant microphysics. In addition, we derive various useful expressions for neutrino source strengths, including those for nucleon–nucleon bremsstrahlung. With this code, we study the character of protoneutron star atmospheres for snapshot post–bounce models, with particular emphasis on their spectra, Eddington factors and angular distributions, phase–space occupancies, and neutrino–matter heating rates. Concerning the latter, we explore the influence of final–state electron blocking, stimulated absorption, velocity terms in the transport equation, neutrino–nucleon scattering asymmetry, and weak magnetism and recoil effects. We also investigate the physical determinants of the ν_μ spectra that emerge from supernova cores and the neutrino heating rates in post–explosion protoneutron star winds. These studies are in preparation for new calculations of spherically symmetric core–collapse supernovae, protoneutron star winds, and neutrino signals, but are also meant to establish a high–accuracy benchmark for future studies of the neutrino atmospheres of evolving protoneutron stars.

Subject headings: supernovae, neutrinos, radiative transfer, atmospheres, spectra

---

[1]Department of Astronomy and Steward Observatory, The University of Arizona, Tucson, AZ 85721

[2]Lawrence Livermore National Laboratory, Livermore, CA 94551

[3]Department of Astronomy and Astrophysics, University of California, Santa Cruz, CA 95064

[4]Department of Physics, The University of Arizona, Tucson, AZ 85721

1. Introduction

With core–collapse supernova explosions, Nature has contrived an elegant means to create compact objects, while at the same time seeding the galaxy with the elements of existence. Neutrinos play a key role in the phenomena of collapse and explosion, for not only are they produced in abundance at the high temperatures and densities achieved in collapse, but they are weakly enough coupled to matter that they transport heat and leptons on a dynamically interesting timescale. It is now thought that neutrino heating of the protoneutron star mantle drives the supernova explosion (Colgate and White 1966; Bethe and Wilson 1985), but only after a post–bounce delay of 100's of milliseconds to one second. During this delay, the quasi–static accreting core, the protoneutron star bounded by the stalled shock wave, radiates neutrinos of all species and the net energy deposition in the semi–transparent "gain region" behind the shock plays a pivotal role in "igniting" the explosion. However, the precise deposition rate depends upon the details of neutrino transfer at low "optical" depths, putting great demands upon the theoretical tools employed to calculate the properties of the neutrino radiation fields. The character of that radiation depends upon neutrino–matter opacities, neutrino production source terms, and neutrino transport. Over the years, neutrino transport theory and the associated microphysics have reached a sophisticated level of refinement (Tubbs and Schramm 1975; Lichtenstadt *et al.* 1978; Bowers and Wilson 1982; Mayle, Wilson, and Schramm 1987; Bludman and Schinder 1988; Bruenn 1985; Janka 1991; Mezzacappa and Bruenn 1993a,b; Messer *et al.* 1998; Yamada, Janka, and Suzuki 1999). However, despite these efforts, recent progress in modeling supernovae, and new insights gained into the character of multi–dimensional neutrino-driven explosions (Herant *et al.* 1994; Burrows, Hayes, and Fryxell 1995; Janka and Müller 1996; Mezzacappa *et al.* 1998), the supernova explosion problem is not solved in detail. We know little about the dependence of the ^{56}Ni yields on progentior mass and composition, the iron–peak nucleosynthesis, the explosion energies, the nascent pulsar kicks, and the asymmetries and mixing in the explosion debris. Furthermore, we still do not know the duration of the post–bounce delay, nor the ensemble of possible neutrino signatures.

In the past, a variety of approximations to the full neutrino transport equations have been employed in complex numerical codes meant to simulate stellar collapse and supernova explosions. These compromises have been deemed necessary because of the severe CPU constraints of such simulations, particularly when those simulations have been multi–dimensional (Herant *et al.* 1994; Burrows, Hayes, and Fryxell 1995; Janka and Müller 1996). A variety of gray approaches, flux limiters, equilibrium assumptions, and approximations to both neutrino source and redistribution terms have been employed, sometimes to good effect. However, given the marginality of the explosions thus far obtained, the fact that there is as yet no unanimity among theorists concerning important issues of principle (cf. Mezzacappa *et al.* 1998), and the manifest importance of neutrinos in collapse phenomenology, a fresh look at neutrino transport and the relevant neutrino physics is in order. It is in that spirit that we have constructed a new implicit, time–dependent, multi–group, multi–angle, multi–species neutrino transfer code to simulate the neutrino radiation

fields in stellar collapse and explosion. This code embodies a different computational philosophy from that used in the pioneering papers by Bruenn (1985) and Mezzacappa (Mezzacappa and Bruenn 1993a,b), but in its use of Feautrier variables and the tangent–ray method it is quite in keeping with traditional photon transport and stellar atmospheres simulations (Mihalas 1980; Mihalas and Mihalas 1984). In this paper, we describe the basic algorithm, discuss and derive the relevant neutrino microphysics, and present high–resolution (in energy, angle, and radius) results for representative post–bounce protoneutron star configurations. Hence, for this first paper in our series on neutrino transport and microphysics we focus on precision neutrino "atmospheres." We present the energy spectra, Eddington factors, angular distributions, phase space densities, and neutrino–matter energy couplings. We also derive or discuss the relevant neutrino physics, some of it new. We calculate the background neutrino radiation fields for two snapshot models, one of which is from the work of Burrows, Hayes, and Fryxell (1995) representing the wind phase that follows explosion (Model W), and one of which (our Model BM) was kindly provided to us by Tony Mezzacappa and is from a multi–group, flux–limited diffusion simulation by Bruenn (Messer *et al.* 1998), 106 milliseconds after the bounce of the core of a Weaver and Woosley (1995) 15 $M_\odot$ star. These are meant to exemplify various protoneutron star structures and phases for the purposes of a detailed scrutiny of the neutrino sector. Consistent dynamical calculations will follow later in the series.

Neutrinos are the major signatures of the inner turmoil of the dense core of the massive star and they carry away the binding energy of the young neutron star, a full 10% of its mass–energy. The detection of collapse neutrinos, their "light curve" and spectra, will allow us to follow in real time the phenomena of stellar death and birth. The supernova, SN1987A, provided a glimpse of what might be possible, but it yielded only 19 events; we can expect the current generation of underground neutrino telescopes to collect thousands of events from a galactic supernova.

In §2, we present the equations and physics of neutrino transport. In §3 we describe our implementation of the Feautrier and tangent–ray schemes, and follow this in §4 with a discussion of accelerated $\mathbf{\Lambda}$ iteration and our approach to the implicit coupling of matter with neutrino radiation. §5 contains a physical derivation of stimulated absorption and §6 summarizes the cross sections we employ for this study. Also in §6 are discussions of dynamic structure factors in neutrino–nucleon scattering and of fully corrected neutrino–nucleus scattering. In §7 we discuss e^+e^- annihilation spectra and rates and in §8 we summarize our $\nu\bar{\nu}$ annihilation equations, taken from the important paper by Janka (1991). We provide in §9 a derivation of the single and pair neutrino rates and spectra for nucleon–nucleon bremsstrahlung, a process that can compete with pair annihilation as a source for ν_μ, $\bar{\nu}_\mu$, ν_τ, and $\bar{\nu}_\tau$ neutrinos. In §10, we present our transport results, including emergent energy spectra, luminosities, specific intensity angular distributions, phase–space occupation factors, energy deposition rates (including those due to $\nu\bar{\nu}$ annihilation), a study of some of the determining factors for the emergent ν_μ spectrum, and a look at the dependence of the emergent spectra on blocking factors, weak magnetism and recoil, aberration and Doppler terms, and stimulated absorption. We also explore some contributions to the neutrino

heating of post–explosion protoneutron star winds.

This paper is meant to contain not only a description of neutrino transfer, our numerical approach, and the new results that flow from it, but to be a tutorial on supernova neutrino physics and microphysics. It is also meant to summarize various useful formulae that others, as they approach the study of supernova neutrino radiation fields, might profitably employ. In assembling the rates and cross sections, we have borrowed liberally from the pioneering investigations of Tubbs and Schramm (1975), Bruenn (1985), Janka (1991), and Mezzacappa (Mezzacappa and Bruenn 1993a,b), but take full responsibility when we have chosen to deviate from the literature, or when we present derivations of new formulae. This subject is rather large, which is why we have chosen to present our results in installments. However, the first installment must perforce have a wide scope. Therefore, we beg the reader's indulgence as we now delve deeply into the art and science of supernova neutrino physics and numerics.

2. Neutrino Transport Equations

We have constructed a new radiation/hydrodynamic code that solves the three equations of hydrodynamics with the equations of multi–group radiative transfer and composition. The hydro code is a one–dimensional Lagrangean realization of the explicit Piecewise–Parabolic Method (PPM) of Colella & Woodward (1984) (Fryxell *et al.* 1991) that is automatically conservative, second–order accurate in space and time, and employs a Riemann solver to handle shocks. Radiation is coupled to the matter between the hydro updates in an implicit, operator–split fashion, employing accelerated $\mathbf{\Lambda}$ iteration (ALI) to facilitate the convergence both of the transport solution and of the temperature and composition changes due to transport. Since in this paper we focus on the transport sector of the code and on precision neutrino atmospheres, we postpone to a later paper a discussion of the full hydrodynamic technique and of time–dependent results in the stellar collapse and supernova context. Here we describe the radiation equations solved, the algorithm developed to solve them, and the philosophy behind our methods. In later sections, we explore the nature of the neutrino radiation fields in the post–bounce and protoneutron star contexts, in particular the angular and spectral distributions and the angular moments. In addition, we study the influence of various terms and physics on the emergent neutrino spectra and on the neutrino–matter coupling in the semi–transparent region between the neutrinospheres and the stalled shock. Energy deposition in this region is thought to be important in igniting and driving the supernova explosion.

Neutrino transport is not an esoteric subject apart from traditional radiative transfer. The same techniques developed for one particle type can be employed for another. For all particles, the solution to the Boltzmann equation is sought. What distinguishes neutrino transport and transfer are the number of neutrino species (six), the particular microphysics of the neutrino–matter interaction (*i.e.,* cross sections, sources), the Fermi statistics of the neutrinos (manifest only in the collision term), and the fact that there is in principle a conserved lepton number. Neutrino

oscillations can alter this, but given the particular neutrino masses and oscillation angles suggested by the recent solar and atmospheric neutrino data, oscillations might not dramatically affect supernova dynamics or the neutrino fields in the core (however, see §10.2.1). (It should be borne in mind that oscillations in the outer envelope of the progenitor massive star or between the supernova and the Earth may alter the signal detected in underground neutrino telescopes.)

There are a variety of ways of writing the transport equation for the specific intensity (I_ν) of the radiation field (Mihalas 1980; Mihalas and Mihalas 1984). In principle, the Boltzmann equation and the transport equation are equivalent, though the former is written in terms of the invariant phase space density ($\mathcal{F}_\nu$), related one–to–one to the specific intensity through the identity:

$$\frac{I(\mu,\varepsilon)}{\varepsilon^3} = \frac{g}{h^3c^2}\mathcal{F}_\nu \ , \tag{1}$$

where $g = 1$ for massless neutrinos, $g = 2$ for photons, ε is the particle's energy, and the other symbols have their standard meanings. Sometimes, it is said that the Boltzmann equation is more general than the transport equation because it contains a $\dot{\mathbf{p}}$ term that for massless particles corresponds to gravitational redshifts. However, there is no reason to exclude such a term from the transport equation and we will not engage in such distinctions.

One form of the transport equation for I_ν in the comoving frame in spherically–symmetric geometry is:

$$\frac{1}{c}\frac{DI_\nu}{Dt} + \frac{\mu}{r^2}\frac{\partial}{\partial r}(r^2 I_\nu) + \frac{\partial}{\partial\mu}\left[(1-\mu^2)\left[\frac{1}{r} + \frac{\mu}{c}\left(\frac{v}{r} - \frac{\partial v}{\partial r}\right)\right] I_\nu\right] - \frac{\partial}{\partial\varepsilon}\left[\varepsilon\left[(1-\mu^2)\frac{v}{cr} + \frac{\mu^2}{c}\frac{\partial v}{\partial r}\right] I_\nu\right]$$
$$+ \left[(3-\mu^2)\frac{v}{cr} + \frac{1+\mu^2}{c}\frac{\partial v}{\partial r}\right] I_\nu + \mathcal{A}_\nu = \eta_\nu - \chi_\nu I_\nu + \frac{\kappa_s}{4\pi}\int \Phi(\mathbf{\Omega},\mathbf{\Omega'})\, I_\nu(\mathbf{\Omega'})\, d\mathbf{\Omega'} \ , \tag{2}$$

where

$$\mathcal{A}_\nu = \frac{a}{c^2}\left[3\mu - (1-\mu^2)\frac{\partial}{\partial\mu} - \varepsilon\frac{\partial}{\partial\varepsilon}\right] I_\nu \, , \tag{3}$$

a is the matter acceleration, $\mu = \cos\theta$, ε is the neutrino energy, and η_ν is the emissivity of the medium. The subscript ν indicates neutrino energy dependence and Φ is an angular phase function for neutrino scattering into the beam. This equation, good to $\mathrm{O}(v/c)$ (where v is the matter velocity and c is the speed of light), assumes azimuthal symmetry and contains the appropriate redshift, aberration, and advection terms due to matter motion, angular redistribution due to scattering into the beam, scattering and absorption out of the beam, and source terms. Eq. (2) does not include energy redistribution upon scattering, to be incorporated in a later version of the code. The various terms represent the additions and subtractions from the beam, the entire equation representing conservation of energy and number. The microphysics and collision terms reside on the right–hand–side and the geometry, aberration, advection, and Doppler shift terms reside on the left.

While eq. (2) contains the relevant terms to $\mathrm{O}(v/c)$, it is a bit ackward to difference. It is also a bit ugly and its various terms are not so cleanly distinguished by their physical roles. Dropping

the acceleration term, we follow Eastman and Pinto (1993) and derive the form of the transport equation we employ in this study. The equation, physically equivalent to the Boltzmann equation (ignoring gravitational redshifts and the acceleration term) for an individual neutrino species, is:

$$\frac{1}{c}\frac{DI_\nu}{Dt} + \mu\frac{\partial I_\nu}{\partial r} + \frac{1-\mu^2}{r}(1-\beta Q\mu)\frac{\partial I_\nu}{\partial \mu} + \frac{\beta}{r}\left(1+Q\mu^2\right)\left(3-\frac{\partial}{\partial \ln\varepsilon}\right) I_\nu$$
$$= \eta_\nu - \chi_\nu I_\nu + \frac{\kappa_s}{4\pi}\int \Phi(\mathbf{\Omega},\mathbf{\Omega'})\, I_\nu(\mathbf{\Omega'})\, d\mathbf{\Omega'} \ , \tag{4}$$

where $Q \equiv \partial \ln v/\partial \ln r - 1$ and all other symbols have their standard meanings. Φ is a phase function for neutrino scattering into the beam. χ_ν is the total extinction coefficient $(= \kappa_a + \kappa_s)$, where κ_a and κ_s contain contributions from all absorption and scattering processes, respectively:

$$\kappa_s = \sum_i n_i\, \sigma_i^s \qquad \text{and} \qquad \kappa_a = \sum_i n_i\, \sigma_i^a \ . \tag{5}$$

Eq. (4) can be rewritten as the corresponding Boltzmann equation for $\mathcal{F}_\nu$:

$$\frac{1}{c}\frac{D\mathcal{F}_\nu}{Dt} + \mu\frac{\partial \mathcal{F}_\nu}{\partial r} + \frac{1-\mu^2}{r}(1-\beta Q\mu)\frac{\partial \mathcal{F}_\nu}{\partial \mu} - \frac{\beta}{r}\left(1+Q\mu^2\right)\frac{\partial \mathcal{F}_\nu}{\partial \ln\varepsilon}$$
$$= \frac{h^3c^2}{g}\left(\frac{\eta_\nu}{\varepsilon^3}\right) - \chi_\nu \mathcal{F}_\nu + \frac{\kappa_s}{4\pi}\int \Phi(\mathbf{\Omega},\mathbf{\Omega'})\, \mathcal{F}_\nu(\mathbf{\Omega'})\, d\Omega' \, , \tag{6}$$

which can be mapped directly, term–by–term, into the Boltzmann equation employed by Messer *et al.* (1998) in their recent work on Boltzmann neutrino transfer. Eq. (6) is the most useful form of the transport equation when studying it using the method of characteristics.

For neutrinos, the phase function for a scattering process i is well approximated by

$$\Phi_i(\mathbf{\Omega},\mathbf{\Omega'}) = \Phi_i(\mathbf{\Omega}\cdot\mathbf{\Omega'}) = \left(1+\delta_i\, \mathbf{\Omega}\cdot\mathbf{\Omega'}\right) = (1+\delta_i\mu) \ , \tag{7}$$

where δ_i is a constant specific to each scattering process and here μ is the angle between the incident and outgoing neutrinos.

Hence, we can write the differential cross section for a scattering process i in terms of the total scattering cross section:

$$\frac{d\sigma_i^s}{d\Omega} = \frac{\sigma_i^s}{4\pi}(1+\delta_i\mu) \ . \tag{8}$$

Subsequently, we drop the superscript s. Eq. (7) implies that the angular redistribution term in eq. (4) becomes

$$\kappa_s J_\nu + \frac{\kappa_s \delta_T}{4\pi}\mathbf{\Omega}\cdot\mathbf{F}_\nu \ , \tag{9}$$

where

$$\delta_T = \frac{\sum_i n_i\, \sigma_i\, \delta_i}{\sum_i n_i\, \sigma_i} \ . \tag{10}$$

F_ν in eq. (9) is the neutrino flux and J_ν is the zeroth moment defined by

$$J_\nu = \frac{1}{2}\int_{-1}^{1} I_\nu \, d\mu = \frac{c}{4\pi} E_\nu \ , \tag{11}$$

where E_ν is the neutrino energy density.

Integrating eq. (4) and $\mathbf{\Omega}\times$ eq. (4) over $d\mathbf{\Omega}$ yields the zeroth and first moment equations, respectively:

$$\frac{1}{c}\frac{DJ_\nu}{Dt} + \frac{1}{r^2}\frac{\partial}{\partial r}(r^2 H_\nu) - \frac{\beta Q}{r}(3P_\nu - J_\nu) + \frac{\beta}{r}\left(3 - \frac{\partial}{\partial \ln\varepsilon}\right)(J_\nu + QP_\nu) = \kappa_a^*(B_\nu - J_\nu) \tag{12}$$

and

$$\begin{aligned}\frac{1}{c}\frac{DH_\nu}{Dt} + \frac{\partial P_\nu}{\partial r} + \frac{3P_\nu - J_\nu}{r} - \frac{\beta Q}{r}(4N_\nu - 2H_\nu) + \frac{\beta}{r}\left(3 - \frac{\partial}{\partial \ln\varepsilon}\right)(H_\nu + QN_\nu) \\ = -\left(\kappa_a^* + \kappa_s - \frac{1}{3}\kappa_s\delta_T\right) H_\nu = -\left(\kappa_a^* + \kappa_{tr}\right) H_\nu \ ,\end{aligned} \tag{13}$$

where H_ν, P_ν, and N_ν are the first, second, and third angular moments given by

$$H_\nu = \frac{1}{2}\int_{-1}^{1} \mu \, I_\nu \, d\mu = \frac{1}{4\pi} F_\nu \ , \tag{14}$$

$$P_\nu = \frac{1}{2}\int_{-1}^{1} \mu^2 \, I_\nu \, d\mu \ , \tag{15}$$

and

$$N_\nu = \frac{1}{2}\int_{-1}^{1} \mu^3 \, I_\nu \, d\mu \ . \tag{16}$$

B_ν is the equilibrium (black body) spectral energy density times $\frac{c}{4\pi}$ and κ_a^* includes the correction for stimulated absorption (see §5). κ_{tr} in eq. (13) is the total transport extinction coefficient and is defined in terms of the individual transport cross sections as $\kappa_{tr} = \sum_i n_i \, \sigma_i^{tr}$. For a particular scattering process i,

$$\sigma_i^{tr} = \int \frac{d\sigma_i}{d\Omega}(1-\mu)\, d\Omega = \sigma_i \left(1 - \frac{1}{3}\delta_i\right) \ . \tag{17}$$

Integrating eq. (12) over energy, we obtain the neutrino energy equation:

$$\frac{DE}{Dt} + \frac{1}{r^2}\frac{\partial}{\partial r}(r^2 F) - \frac{v}{r}(3p-1)QE + 4\frac{v}{r}(1+Qp)E = 4\pi\int_0^\infty \kappa_a^*(B_\nu - J_\nu)\, d\varepsilon \ , \tag{18}$$

where E and F are the integrated neutrino energy density and flux, respectively. p is the energy–integrated Eddington factor, where $p_\nu = P_\nu/J_\nu$. The sums for all neutrino species of the negative of the right–hand–side of eq. (18) and the negative of the ε_ν integral of the right–hand–side of eq. (13) are the energy and momentum source terms in the matter equations. The two equations for the rate of change of the electron fraction (Y_e) due to $e^-/e^+/\nu_e/\bar{\nu}_e$ capture are:

$$\rho \mathcal{N}_{\mathcal{A}} \frac{DY_e}{Dt}_{\pm} = \pm 4\pi \int_0^\infty \kappa_a^* (B_\nu - J_\nu)_\pm \frac{d\varepsilon}{\varepsilon} \,, \tag{19}$$

where the $-$ sign is for the ν_e equation and the $+$ sign is for the $\bar{\nu}_e$ equation. Eqs. (4), (12), and (13) for each neutrino species, along with eqs. (19), are the basic neutrino transport equations that we solve. ρ is the mass density and $\mathcal{N}_{\mathcal{A}}$ is Avogadro's number.

3. Method of Solution: Feautrier and Tangent–Ray Algorithm

We solve the moment eqs. (12) and (13) implicitly for J_ν and H_ν by backwards differencing in time the quantities $J_\nu/\rho^{4/3}$ and $H_\nu/\rho^{2/3}$, backwards differencing in $\ln \varepsilon$ (according to the slope of the characteristic), and combining the spatially differenced equations into one equation for J_ν which is 2nd–order accurate in r. Standard matrix inversion techniques are employed to obtain J_ν, from which H_ν is derived using eq. (13). This equation is manifestly Lagrangean and by solving it the advective derivative is included automatically. $J_\nu/\rho^{4/3}$ and $H_\nu/\rho^{2/3}$ are the natural combinations for adiabatic compression or expansion of a relativistic gas.

Since eqs. (12) and (13) contain the higher–order angular moments P_ν and N_ν, closure relations are needed. These are obtained from a formal integration of the full transport equation (4), written in terms of the Feautrier variables:

$$U_\nu(\mu) = \frac{1}{2}(I_\nu(\mu) + I_\nu(-\mu)) \qquad \text{and} \qquad V_\nu(\mu) = \frac{1}{2}(I_\nu(\mu) - I_\nu(-\mu)) \,, \tag{20}$$

where μ ranges from 0 to 1.

In the isotropic scattering limit ($\delta_T = 0$), these equations for U_ν and V_ν are:

$$\frac{1}{c}\frac{DU_\nu}{Dt} + \mu \frac{\partial V_\nu}{\partial r} - \frac{1-\mu^2}{r} \beta Q \mu \frac{\partial U_\nu}{\partial \mu} + \frac{\beta}{r}\left(3 - \frac{\partial}{\partial \ln \varepsilon}\right)(1 + Q\mu^2) U_\nu = \eta_\nu - \chi_\nu U_\nu + \kappa_s J_\nu \tag{21}$$

and

$$\frac{1}{c}\frac{DV_\nu}{Dt} + \mu \frac{\partial U_\nu}{\partial r} - \frac{1-\mu^2}{r} \beta Q \mu \frac{\partial V_\nu}{\partial \mu} + \frac{\beta}{r}\left(3 - \frac{\partial}{\partial \ln \varepsilon}\right)(1 + Q\mu^2) V_\nu = -\chi_\nu V_\nu \,. \tag{22}$$

From the solution of eqs. (21) and (22), we obtain the full radiation field and the higher–order moments that are then used in eqs. (12) and (13) for J_ν and H_ν. Since eqs. (21) and (22) require the lower–order moment J_ν (and in principle H_ν, *cf.* eq. 9), we iterate this system until we obtain a converged and consistent global solution. Simultaneously, we calculate the $\mathbf{\Lambda}$ operator that maps S_ν, the source function, onto J_ν and employ accelerated $\mathbf{\Lambda}$ iteration (Cannon 1973a,b; Scharmer 1981; Olson, Auer, and Buchler 1986; Eastman and Pinto 1993) to speed the convergence of the temperature and composition updates. Independent of the total optical depth, this generally requires no more than 2 to 3 iterations to obtain an accuracy of a part in 10^6. To maintain stability and reflect the density character of $U_\nu(\mu)$ and the flux character of $V_\nu(\mu)$, we stagger the $U_\nu(\mu)$ and $V_\nu(\mu)$ meshes with respect to one another by half a zone.

It may seem that by solving the moment equations separately and iterating with the solution of the transport equation itself and by not focusing simply on the solution of eqs. (21) and (22) or eq. (4) that we are doing more than is necessary. The advantage of solving the moment equations is that they can be differenced conservatively. Energy conservation is a major problem for most methods, *e.g.*, S_n methods, whereas we can conserve energy in the transport sector of the calculation to as many digits as we are willing to pay for. The advantage of calculating U_ν and V_ν instead of I_ν is that equations (21) and (22) can be differenced in such a way that V_ν will go accurately to $3\mu\partial S_\nu/\partial\tau_\nu$ in the large–optical–depth, diffusion limit, and still remain accurate in the optically–thin, free–streaming limit. Schemes based directly on eq. (2) or (4) have the correct large–optical–depth behavior for U_ν, *i.e.* $U_\nu = S_\nu$, but have round–off trouble computing V_ν, which is important if the only estimate of the flux comes from integrating μV_ν over angle. Typically in such codes above a certain optical depth the diffusion limit is assumed and V_ν is set equal to $3\mu\partial S_\nu/\partial\tau_\nu$.

To solve eqs. (21) and (22), we employ the tangent–ray method (Mihalas and Mihalas 1984). At a reference radial zone, tangents are constructed to each of the interior zones. The angles of the tangent rays to the normal at the reference zone define the angular grid at that zone on which the angular integrations are performed. Eqs. (21) and (22) are integrated along each tangent ray. If there are nx radial zones, the radiation field at the outer zone is resolved with $nx - 1$ angles; as you move inward the number of angles employed decreases linearly. Hence, if there are 100 radial zones, there are as many as 99 angular bins. With reasonable radial gridding, this approach can provide exquisite angular resolution, but at the cost of increased computational overhead. For instance, we have tested our implementation of the tangent–ray method with the Kosirev (spherical Milne) problem for which the absorptive opacity is assumed to be a power law in radius ($\kappa = 1/r^n$). For a variety of integer power laws (*e.g.*, $n = 1.1, 1.3, 1.5, 2, 3, 4$), with from 100 to 500 radial zones, our code is always more accurate than the discrete ordinate method with 24 angles, and better than the discrete ordinate method with 64 angles for $nx = 500$ (also J. Smit, private communication). However, care must be taken to avoid purely geometrical zoning, for which $r_{n+1} = \alpha r_n$, since such zoning biases the angular binning in a systematic way. The result can be that the Eddington and flux factors asymptote at infinity to between 0.96 and 0.98, and not to 1.0. However, purely geometrical zoning is easily avoided in real calculations. Note that the increase in angular resolution with radius which comes naturally from this procedure is quite appropriate to spherical symmetry. At $r = 0$, the radiation field is by definition symmetric and needs no angular resolution. As r becomes large, a small bright central source is increasingly finely resolved.

For dynamical, time–dependent calculations, solving eqs. (21) and (22) by the tangent-ray method at each timestep can be quite slow. Fortunately, as long as the 2'nd and 3'rd angular moments do not change quickly, one need not solve eqs. (21) and (22) at every timestep. Frequently, the solution to the moment equations (12) and (13) with previous values of p_ν and g_ν ($= N_\nu/H_\nu$) can be quite accurate. This is not the case during shock breakout through the neutrinospheres, nor during other very dynamical phases. However, it is the case during much of

the pre–explosion delay and protoneutron star phases, as well as during much of the core collapse phase.

Currently, there are two minor approximations in our algorithm for solving the transport equations (21) and (22). The first is that in calculating the radiation angular moments we assume that scattering into the beam is isotropic, while maintaining the correct transport cross section in the H_ν moment eq. (13). The second approximation involves the assumption of linearity of the characteristics. The 2'nd term in both eqs. (21) and (22) which is proportional to $\partial/\partial\mu$ comes from the aberration experienced in going from the local to a nearby rest frame. The characteristics are not perfectly straight, which can make the calculation more difficult. One cannot simply integrate along a straight–line impact ray. However, these terms are often insignificant because we need only an approximate estimate of U_ν and V_ν and we are using them to compute only the closure coefficients, p_ν and g_ν. Rather than just ignore these two terms, we have substituted

$$\frac{1-\mu^2}{r}\beta Q\mu\frac{\partial U_\nu}{\partial\mu} \approx \frac{3\mu^2-1}{r}\beta Q\mu U_\nu \tag{23}$$

in equation (21) and

$$\frac{1-\mu^2}{r}\beta Q\mu\frac{\partial V_\nu}{\partial\mu} \approx \frac{4\mu^2-2}{r}\beta Q\mu V_\nu \tag{24}$$

in equation (22). The substitution in eq. (23) is derived by integrating the left–hand–side by parts and the substitution in eq. (24) is derived by integrating μ times the left–hand–side by parts. Importantly, the two terms in (23) integrate to the same thing and μ times the two terms in eq. (24) integrate to the same thing. Therefore, both modified equations reduce to the energy and momentum conservation equations.

4. Implicit Coupling to Matter and Accelerated Λ Iteration

Though we are not highlighting in this paper time–dependent calculations, we think it useful to include a discussion of the technique we employ to couple matter with neutrinos. This is done implicitly in operator–split fashion, after each hydro update. For each neutrino species, the scattering and absorption opacities and the emissivities are calculated and fed into the transport solver. A fully converged solution of the transport equations is obtained and this is used to calculate the various terms needed for the implicit update due to transport of the temperature and Y_e. In particular, the derivatives with respect to temperature and Y_e of the right–hand–sides of eqs. (18) and (19) are calculated. For the implicit temperature update at each radial zone, i, a backward–differenced matter energy equation like:

$$\rho C_V\frac{T_i^{k+1}-T_i^k+\Delta T_i}{\Delta t} = -4\pi\int_0^\infty(\eta'-\kappa_a^* J_\nu)\,d\varepsilon - 4\pi\Delta T_i\int_0^\infty\Big(\frac{\partial\eta'}{\partial T}-\frac{\partial\kappa_a^*}{\partial T}J_\nu-\kappa_a^*\frac{\partial J_\nu}{\partial T}\Big)\,d\varepsilon \tag{25}$$

is constructed, where ΔT_i is the temperature change between iterations, T_i^{k+1} is the new temperature, T_i^k is the old temperature, C_V is the specific heat, η' is not corrected for final–state

neutrino blocking (§5), and Δt is the timestep. (In fact, the matter energy is a function of both T and Y_e and there is an extra term in the temperature update equation to account for the entropy change due to the Y_e composition change, but that term is dropped here for clarity, though not in the computations.)

The subtlety with eq. (25) lies in the $\frac{\partial J_\nu}{\partial T}$ term. In general, J_i equals $\mathbf{\Lambda}_{ij} S_j$ at each frequency or energy, where the $\mathbf{\Lambda}$ operator is a matrix coupling different zones. Hence, eq. (25) is a matrix equation with

$$\frac{\partial J_i}{\partial T} = \mathbf{\Lambda}_{ij} \frac{\partial S_j}{\partial T} \,. \tag{26}$$

For simplicity in eq. (25), we have dropped in eq. (26) the $\mathbf{\Gamma}$ operator that couples energy groups. Though we have the option in the code of calculating the full $\mathbf{\Lambda}$ matrix, we use only the diagonal and the two adjacent off–diagonals. It is this truncated tridiagonal $\mathbf{\Lambda}$ operator that we actually employ. Since the S_ν we use in eq. (26), perhaps a bit idiosyncratically, equals η'/κ^*, $\frac{\partial S}{\partial T}$ is given by

$$\frac{\partial S_i}{\partial T} = \Big(\frac{\partial \eta_i'}{\partial T} - S_i \frac{\partial \kappa_i^*}{\partial T}\Big)/\kappa_i^* \,, \tag{27}$$

and this is employed to derive:

$$\frac{\partial J_i}{\partial T} = \mathbf{\Lambda}_{i,i+1} \frac{\partial S_{i+1}}{\partial T} + \mathbf{\Lambda}_{i,i-1} \frac{\partial S_{i-1}}{\partial T} + \mathbf{\Lambda}_{i,i} \frac{\partial S_i}{\partial T} \,. \tag{28}$$

Plugging eq. (28) into eq. (25), we solve for ΔT_i by inverting the tridiagonal matrix. For the ν_e and $\bar{\nu}_e$ species, a similar procedure is followed to obtain ΔY_e from eq. (19). Note that the integral over neutrino energy is performed before the T and Y_e updates, which are not attempted for each energy group individually.

Once ΔT_i and ΔY_e^i are obtained, T_i^{k+1} is set equal to $T_i^k + \Delta T_i$ and $Y_e^{k+1,i}$ is set equal to $Y_e^{k,i} + \Delta Y_e^i$. We then loop back to obtain a new transport solution with the new temperature and Y_e. This procedure is iterated until $\Delta T_i/T_i$ and $\Delta Y_e^i/Y_e^i$ are suitably small (normally 10^{-6}) for all zones, at which time we are left with a completely consistent set of J_ν, H_ν, U_ν, V_ν, T, and Y_e. T_i^k and Y_e^i are not changed during the iteration. The total number of iterations varies between 1 and 7, the latter only when Y_e is changing fast in either the ν_e or the $\bar{\nu}_e$ modules. The various neutrino fluids are updated in series, not in parallel and we generally follow three species: ν_e, $\bar{\nu}_e$, and "ν_μ," the latter representing the sum of ν_μ, $\bar{\nu}_\mu$, ν_τ, and $\bar{\nu}_\tau$ neutrinos. Bunching these four neutrino species into one assumes that their cross sections and source terms are identical, which technically is false, but quantitatively reasonable (see §7). Note that to achieve stable iteration, it is essential for the derivatives in eq. (25) to be accurate. Among other things, this requires good derviatives of $\hat{\mu}$ $(= \mu_n - \mu_p)$ with respect to T and Y_e. Analytic derivatives are preferred, but numerical derivatives for most quantities seem to work.

As stated previously, to achieve rapid convergence of the transport iteration we employ ALI, accelerated $\mathbf{\Lambda}$ iteration (Cannon 1973a,b; Scharmer 1981; Olson, Auer, and Buchler 1986). This

entails an approximation that improves during the iteration. In particular, we use

$$J_\nu^{k+1} = J_\nu^k + \mathbf{\Lambda}^k (S_\nu^{k+1} - S_\nu^k) \,, \tag{29}$$

where $\mathbf{\Lambda}^k$ is the retarded $\mathbf{\Lambda}$ operator. We use only its diagonal and first off–diagonal terms. This procedure accelerates and stabilizes the iteration, even if the optical depth is large and the scattering albedo is high.

5. Stimulated Absorption

The concept of stimulated emission for photons is well understood and studied, but the corresponding concept of stimulated *absorption* for neutrinos is not so well appreciated. This may be because its simple origin in Fermi blocking and the Pauli exclusion principle in the context of *net* emission is not often explained. The *net* emission of a neutrino is simply the difference between the emissivity and the absorption of the medium:

$$\mathcal{J}_{net} = \eta_\nu - \kappa_a I_\nu \ . \tag{30}$$

All absorption processes involving fermions will be inhibited by Pauli blocking due to final–state occupancy. Hence, η_ν in eqs. (30) and (4) includes a blocking term, $(1 - \mathcal{F}_\nu)$ (Bruenn 1985). $\mathcal{F}_\nu$ is the invariant distribution function for the neutrino, whether or not it is in chemical equilibrium.

We can derive stimulated absorption using Fermi's Golden rule. For example, the net collision term for the process, $\nu_e n \leftrightarrow e^- p$, is:

$$\begin{aligned} \mathcal{C}_{\nu_e n \leftrightarrow e^- p} &= \int \frac{d^3\vec{p}_{\nu_e}}{(2\pi)^3} \int \frac{d^3\vec{p}_n}{(2\pi)^3} \int \frac{d^3\vec{p}_p}{(2\pi)^3} \int \frac{d^3\vec{p}_e}{(2\pi)^3} \left(\sum_s |\mathcal{M}|^2 \right) \\ &\times \ \Xi(\nu_e n \leftrightarrow e^- p)\ (2\pi)^4\, \delta^4(\mathbf{p}_{\nu_e} + \mathbf{p}_n - \mathbf{p}_p - \mathbf{p}_e) \ , \end{aligned} \tag{31}$$

where $\mathbf{p}$ is a four-vector and

$$\Xi(\nu_e n \leftrightarrow e^- p) = \mathcal{F}_{\nu_e} \mathcal{F}_n (1 - \mathcal{F}_e)(1 - \mathcal{F}_p) - \mathcal{F}_e \mathcal{F}_p (1 - \mathcal{F}_n)(1 - \mathcal{F}_{\nu_e}) \ . \tag{32}$$

The final–state blocking terms in eq. (32) are manifest, in particular that for the ν_e neutrino. Algebraic manipulations convert $\Xi(\nu_e n \leftrightarrow e^- p)$ in eq. (32) into:

$$\begin{aligned} \Xi(\nu_e n \leftrightarrow e^- p) &= \mathcal{F}_n (1 - \mathcal{F}_e)(1 - \mathcal{F}_p) \left[\frac{\mathcal{F}'_{\nu_e}}{1 - \mathcal{F}'_{\nu_e}} (1 - \mathcal{F}_{\nu_e}) - \mathcal{F}_{\nu_e} \right] \\ &= \frac{\mathcal{F}_n (1 - \mathcal{F}_e)(1 - \mathcal{F}_p)}{1 - \mathcal{F}'_{\nu_e}} \left[\mathcal{F}'_{\nu_e} - \mathcal{F}_{\nu_e} \right] \ , \end{aligned} \tag{33}$$

where

$$\mathcal{F}'_{\nu_e} = [e^{(\varepsilon_{\nu_e} - (\mu_e - \hat{\mu}))\beta} + 1]^{-1} \tag{34}$$

is an equilibrium distribution function for the ν_e neutrino and it has been assumed that only the electron, proton, and neutron are in thermal equilibrium. Note that in $\mathcal{F}'_{\nu_e}$ there is no explicit reference to a neutrino chemical potential, though of course in beta equilibrium it is equal to $\mu_e - \hat{\mu}$. There is no need to construct or refer to a neutrino chemical potential in neutrino transfer.

Using eq. (1), we see that eq. (33) naturally leads to:

$$\mathcal{J}_{net} = \frac{\kappa_a}{1 - \mathcal{F}'_\nu} (B_\nu - I_\nu) = \kappa^*_a (B_\nu - I_\nu) \ . \tag{35}$$

This is akin to the right-hand-side of eq. (12). If neutrinos were bosons, we would have found a $(1 + \mathcal{F}'_\nu)$ in the denominator, but the form of eq. (35) in which I_ν is manifestly driven to B_ν, the equilibrium intensity, would have been retained. From eqs. (33) and (35), we see that the stimulated absorption correction to κ_a is $1/(1 - \mathcal{F}'_\nu)$. If we want to retain the form of the collision term as expressed in eqs. (30) or (4), the physics is unaltered and stimulated absorption is not needed as a concept, as long as η_ν in eq. (4) contains the neutrino Pauli blocking term, $(1 - \mathcal{F}_\nu)$, without the prime. However, by writing the collision term in the form of eq. (35), with κ_a corrected for stimulated absorption, we have a net source term that clearly drives I_ν to equilibrium. The timescale is $1/c\kappa^*_a$. Though the derivation of the stimulated absorption correction we have provided here is for the $\nu_e n \leftrightarrow e^- p$ process, this correction is quite general and applies to all neutrino absorption opacities.

Kirchhoff's Law, expressing detailed balance, is:

$$\kappa_a = \eta_\nu / B_\nu \text{ or } \kappa^*_a = \eta'_\nu / B_\nu \ , \tag{36}$$

where η'_ν is not corrected for final–state neutrino blocking. Furthermore, the net emissivity can be written as the sum of its *spontaneous* and *induced* components:

$$\eta_\nu = \kappa_a \left[\frac{B_\nu}{1 \pm \mathcal{F}'_\nu} + \left(1 - \frac{1}{1 \pm \mathcal{F}'_\nu} \right) I_\nu \right] \ , \tag{37}$$

where + or − is used for bosons or fermions, respectively.

6. Neutrino Cross Sections

Neutrino–matter cross sections, both for scattering and for absorption, play the central role in neutrino transport. The major processes are the super–allowed charged–current absorptions of ν_e and $\bar{\nu}_e$ neutrinos on free nucleons, neutral–current scattering off of free nucleons, alpha particles, and nuclei (Freedman 1974), neutrino–electron/positron scattering, neutrino–nucleus absorption, neutrino–neutrino scattering, neutrino–antineutrino absorption, and the inverses of various neutrino production processes such as nucleon–nucleon bremsstrahlung and the modified URCA process ($\nu_e + n + n \rightarrow e^- + p + n$). Compared with photon–matter interactions, neutrino–matter interactions are relatively simple functions of incident neutrino energy. Resonances play

little or no role and continuum processes dominate. Nice summaries of the various neutrino cross sections of relevance in supernova theory are given in Tubbs and Schramm (1975) and in Bruenn (1985). In particular, Bruenn (1985) discusses in detail neutrino–electron scattering and neutrino–antineutrino processes using the full energy redistribution formalism. He also provides a serviceable approximation to the neutrino–nucleus absorption cross section (Fuller 1982; Fuller, Fowler, and Newman 1983; Aufderheide *et al.* 1994). Since during the delay and protoneutron star phases on which we focus in this paper the radiation fields and spectra of ν_e and $\bar{\nu}_e$ neutrinos do not depend on these processes, we do not dwell on them here. Recall that for a neutrino energy of $\sim$10 MeV the ratio of the charged–current cross section to the ν_e–electron scattering cross section is $\sim$100. However, neutrino–electron scattering does play a role, along with neutrino–nucleon scattering and nucleon–nucleon bremsstrahlung, in the energy equilibration of emergent ν_μ neutrinos, though the relative contribution of each has yet to be determined. In this context, our current lack of an energy redistribution algorithm should be borne in mind. Nevertheless, our general conclusions concerning the ν_μ neutrinos, their softer than previously-believed spectra, their angular distributions and moments, the potential role of bremsstrahlung in their production, and the role of their high scattering albedos, will only be strengthened when competent energy redistribution is included.

Below, we list and discuss many of the cross sections we employ in our calculations. Though we assume that all scatterings are elastic, in §6.5 we provide some straightforward formulae that can be used to properly handle ineleastic scattering off of nucleons in the atmospheres of protoneutron stars. These formulae include in a self–consistent way final–state nucleon blocking. In addition, a variety of useful facts and equations are presented to clarify and summarize the major neutrino–matter interactions. In sections 7, 8, and 9 we discuss aspects of e^+e^- annihilation, $\nu\bar{\nu}$ annihilation, and nucleon–nucelon bremsstrahlung. Collectively, these sections encapsulate the microphysics most relevant to neutrino atmospheres and core–collapse supernovae.

6.1. $\nu_e + n \rightarrow e^- + p$:

The cross section per baryon for ν_e neutrino absorption on free neutrons is larger than that for any other process. Given the large abundance of free neutrons in protoneutron star atmospheres, this process is central to ν_e neutrino transport. A convenient reference neutrino cross section is σ_o, given by

$$\sigma_o = \frac{4G^2(m_e c^2)^2}{\pi(\hbar c)^4} \simeq 1.705 \times 10^{-44}\, cm^2 \ . \tag{38}$$

The total $\nu_e - n$ absorption cross section is then given by

$$\sigma^a_{\nu_e n} = \sigma_o \left(\frac{1+3g_A^2}{4}\right) \left(\frac{\varepsilon_{\nu_e} + \Delta_{np}}{m_e c^2}\right)^2 \left[1 - \left(\frac{m_e c^2}{\varepsilon_{\nu_e} + \Delta_{np}}\right)^2\right]^{1/2} W_M \ , \tag{39}$$

where g_A is the axial–vector coupling constant (~ -1.26), $\Delta_{np} = m_n c^2 - m_p c^2 = 1.29332$ MeV, and for a collision in which the electron gets all of the kinetic energy $\varepsilon_{e^-} = \varepsilon_{\nu_e} + \Delta_{np}$. W_M

is the correction for weak magnetism and recoil (Vogel 1984) and is approximately equal to $(1 + 1.1\varepsilon_{\nu_e}/m_nc^2)$. At $\varepsilon_{\nu_e} = 20$ MeV, this correction is only $\sim 2.5\%$. We include it here for symmetry's sake, since the corresponding correction ($W_{\bar{M}}$) for $\bar{\nu}_e$ neutrino absorption on protons is $(1 - 7.1\varepsilon_{\bar{\nu}_e}/m_nc^2)$, which at 20 MeV is a large -15%. To calculate κ_a^*, $\sigma^a_{\nu_e n}$ must be multiplied by the stimulated absorption correction, $1/(1 - \mathcal{F}'_{\nu_e})$, and final–state blocking by the electrons and the protons à la eq. (33) must be included.

6.2. $\bar{\nu}_e + p \rightarrow e^+ + n$:

The total $\bar{\nu}_e - p$ absorption cross section is given by

$$\sigma^a_{\bar{\nu}_e p} = \sigma_o \left(\frac{1 + 3g_A^2}{4}\right) \left(\frac{\varepsilon_{\bar{\nu}_e} - \Delta_{np}}{m_ec^2}\right)^2 \left[1 - \left(\frac{m_ec^2}{\varepsilon_{\bar{\nu}_e} - \Delta_{np}}\right)^2\right]^{1/2} W_{\bar{M}}\,, \tag{40}$$

where $\varepsilon_{e^+} = \varepsilon_{\bar{\nu}_e} - \Delta_{np}$ and $W_{\bar{M}}$ is the weak magnetism/recoil correction given in §6.1. Note that $W_{\bar{M}}$ is as large as many other corrections and should not be ignored. To calculate κ_a^*, $\sigma^a_{\bar{\nu}_e p}$ must also be corrected for stimulated absorption and final–state blocking. However, the sign of $\mu_e - \hat{\mu}$ in the stimulated absorption correction for $\bar{\nu}_e$ neutrinos is flipped, as is the sign of μ_e in the positron blocking term. Hence, as a consequence of the severe electron lepton asymmetry in core–collapse supernovae, both coefficients are very close to one. Note that the $\bar{\nu}_e + p \rightarrow e^+ + n$ process dominates the supernova neutrino signal in proton–rich underground neutrino telescopes on Earth, such as Super Kamiokande, LVD, and MACRO, a fact that emphasizes the interesting complementarities between emission at the supernova and detection in Čerenkov and scintillation facilities.

6.3. $\nu_i + p \rightarrow \nu_i + p$:

The total $\nu_i - p$ scattering cross section for all neutrino species is:

$$\sigma_p = \frac{\sigma_o}{4}\left(\frac{\varepsilon_\nu}{m_ec^2}\right)^2 \left(4\sin^4\theta_W - 2\sin^2\theta_W + \frac{(1 + 3g_A^2)}{4}\right)\,, \tag{41}$$

where θ_W is the Weinberg angle and $\sin^2\theta_W \simeq 0.23$. In terms of $C'_V = 1/2 + 2\sin^2\theta_W$ and $C'_A = 1/2$, eq. (41) becomes (Schinder 1990):

$$\sigma_p = \frac{\sigma_o}{4}\left(\frac{\varepsilon_\nu}{m_ec^2}\right)^2 \left[(C'_V - 1)^2 + 3g_A^2(C'_A - 1)^2\right]. \tag{42}$$

From eq. (8) we obtain the differential cross section:

$$\frac{d\sigma_p}{d\Omega} = \frac{\sigma_p}{4\pi}(1 + \delta_p\mu)\,, \tag{43}$$

where

$$\delta_p = \frac{(C'_V - 1)^2 - g_A^2(C'_A - 1)^2}{(C'_V - 1)^2 + 3g_A^2(C'_A - 1)^2} \ . \tag{44}$$

Note that δ_p, and δ_n below, are negative ($\delta_p \sim -0.2$ and $\delta_n \sim -0.1$) and, hence, that these processes are backward–peaked.

The transport cross section is simply

$$\sigma_p^{tr} = \frac{\sigma_o}{6}\left(\frac{\varepsilon_\nu}{m_e c^2}\right)^2 \left[(C'_V - 1)^2 + 5g_A^2(C'_A - 1)^2\right] \ . \tag{45}$$

6.4. $\nu_i + n \rightarrow \nu_i + n$:

The total $\nu_i - n$ scattering cross section is:

$$\sigma_n = \frac{\sigma_o}{4}\left(\frac{\varepsilon_\nu}{m_e c^2}\right)^2 \left(\frac{1 + 3g_A^2}{4}\right) \ . \tag{46}$$

From eq. (8), we obtain the differential cross section

$$\frac{d\sigma_n}{d\Omega} = \frac{\sigma_n}{4\pi}(1 + \delta_n \mu) \ , \tag{47}$$

where

$$\delta_n = \frac{1 - g_A^2}{1 + 3g_A^2} \ . \tag{48}$$

The transport cross section is

$$\sigma_n^{tr} = \frac{\sigma_o}{4}\left(\frac{\varepsilon_\nu}{m_e c^2}\right)^2 \left(\frac{1 + 5g_A^2}{6}\right) \ . \tag{49}$$

The fact that δ_p and δ_n are negative and, as a consequence, that σ_i^{tr} is greater than σ_i increases the neutrino–matter energy coupling rate for a given neutrino flux in the semi–transparent region. This increase in inverse flux factor (J_ν / H_ν) is but one effect that can be studied with the transport tools we have developed and are developing.

6.5. Dynamic Structure Factors for Neutrino–Nucleon Interactions

Recent explorations into the effects of many–body correlations on neutrino–matter opacities at high densities have revealed that for densities above 10^{14} gm cm^{-3} both the charged–current and the neutral–current interaction rates are decreased by a factor of perhaps 2 to 5, depending on the density and the equation of state (Burrows and Sawyer 1998a,b; Reddy *et al.* 1998; Yamada 1998). Furthermore, it has been shown that the rate of energy transfer due to neutral–current scattering

off of nucleons exceeds that due to ν_μ–electron scattering (Janka *et al.* 1996). Previously, it had been assumed that neutrino–nucleon scattering was elastic (Lamb and Pethick 1976). However, these recent reappraisals reveal that the product of the underestimated energy transfer per neutrino–nucleon scattering with cross section exceeds the corresponding quantity for neutrino–electron scattering. Since ν_e and $\bar{\nu}_e$ neutrinos participate in super–allowed charged–current absorptions on nucleons, neutrino–nucleon scattering has little effect on their rate of equilibration. However, such scattering would seem to be important for ν_μ and ν_τ equilibration. Since the many–body correlation suppressions appear only above neutrinosphere densities ($\sim 10^{11} - 10^{13}$ gm cm^{-3}), it is only the kinematic effect, and not the interaction effect, that need be considered when studying the emergent spectra. We have not yet incorporated energy redistribution into our transport scheme, but we provide the relevant dynamical structure factor ($S(q,\omega)$) for completeness. Without interactions, $S(q,\omega)$ for neutrino–nucleon scattering is simply

$$S(q,\omega) = 2\int \frac{d^3p}{(2\pi)^3}\mathcal{F}(|\mathbf{p}|)(1-\mathcal{F}(|\mathbf{p}+\mathbf{q}|))2\pi\delta(\omega+\epsilon_{\mathbf{p}}-\epsilon_{\mathbf{p}+\mathbf{q}})\,, \tag{50}$$

where $\mathcal{F}(|\mathbf{p}|)$ is the nucleon Fermi–Dirac distribution function, $\epsilon_{\mathbf{p}}$ is the nucleon energy, ω is the energy transfer to the medium, and $\mathbf{q}$ is the momentum transfer. The magnitude of $\mathbf{q}$ is related to ω and E_1, the incident neutrino energy, through the neutrino scattering angle, θ, by the expression,

$$q = [E_1^2 + (E_1-\omega)^2 - 2E_1(E_1-\omega)\cos\theta]^{1/2}\,. \tag{51}$$

In the elastic limit and ignoring final–state nucleon blocking, $S(q,\omega) = 2\pi\delta(\omega)n_n$, the expected result, where n_n is the nucleon's number density.

The neutral current scattering rate off of either neutrons or protons is (Burrows and Sawyer 1998),

$$\frac{d^2\Gamma}{d\omega d\cos\theta} = (4\pi^2)^{-1}G_W^2(E_1-\omega)^2[1-\mathcal{F}_\nu(E_1-\omega)]\mathcal{I}_{\rm NC}\,, \tag{52}$$

where

$$\mathcal{I}_{\rm NC} = \Big[(1+\cos\theta)V + (3-\cos\theta)A\Big]S(q,\omega) \tag{53}$$

and

$$S(q,\omega) \;\;=\;\; 2{\rm Im}\Pi^{(0)}(1-{\rm e}^{-\beta\omega})^{-1}\,. \tag{54}$$

V and A are the applicable vector and axial–vector coupling terms (see §6.3 and §6.4) and $\beta = 1/kT$. The free polarization function, $\Pi^{(0)}$, contains the full kinematics of the scattering, as well as blocking due to the final–state nucleon, and the relevant imaginary part of $\Pi^{(0)}$ is given by:

$${\rm Im}\Pi^{(0)}(q,\omega) = \frac{m^2}{2\pi q\beta}\log\left[\frac{1+e^{-Q_+^2+\beta\mu}}{1+e^{-Q_+^2+\beta\mu-\beta\omega}}\right]\,, \tag{55}$$

where

$$Q_\pm = \left(\frac{m\beta}{2}\right)^{1/2}\left(\mp\frac{\omega}{q}+\frac{q}{2m}\right) \tag{56}$$

μ is the nucleon chemical potential, and m is the nucleon mass. The dynamical structure factor, $S(q,\omega)$, contains all of the information necessary to handle angular and energy redistribution due to scattering. The corresponding term on the right–hand–side of the transport equation (eq. 4) is:

$$\mathcal{S}[\mathcal{F}_\nu] = (2\pi)^{-3} G_W^2 \int d^3p'_\nu \, \mathcal{I}_{\rm NC} \left\{ [1-\mathcal{F}_\nu(E_1)]\mathcal{F}'_\nu(E_1-\omega)e^{-\beta\omega} - \mathcal{F}_\nu(E_1)[1-\mathcal{F}'_\nu(E_1-\omega)] \right\} , \quad (57)$$

where p'_ν is the final state neutrino momentum. This term would supercede the elastic scattering terms now on the right–hand–side of eq. (4).

In the non-degenerate nucleon limit, eq. (55) can be expanded to lowest order in Q_+^2 to obtain, using eq. (54), an approximation to the dynamical structure factor:

$$S(q,\omega) \;\; = \;\; \frac{n(2\pi m\beta)^{1/2}}{q} \, e^{-Q_+^2} , \quad (58)$$

where n is the nucleon number density. This says that for a given momentum transfer the dynamical structure factor is approximately a Gaussian in ω.

For charged–current absorption process, $\nu_e + n \rightarrow e^- + p$, ${\rm Im}\Pi^{(0)}(q,\omega)$ is given by a similar expression:

$${\rm Im}\Pi^{(0)}(q,\omega) = \frac{m^2}{2\pi\beta q} \log\Big[\frac{1+e^{-Q_+^2+\beta\mu_n}}{1+e^{-Q_+^2+\beta\mu_p-\beta\omega}} \Big] . \quad (59)$$

Eq. (59) inserted into eq. (54) with a $(1-e^{-\beta(\omega+\hat{\mu})})$, as is appropriate for the charged–current process, substituted for $(1-e^{-\beta\omega})$, results in an expression that is a bit more general than the one employed to date by most practitioners, *i.e.*, $S = (X_n - X_p)/(1-e^{-\hat{\mu}/T})$. In the non-degenerate nucleon limit, the structure factor for the charged–current process can be approximated by eq. (58) with $n = n_n$. Note that for the structure factor of a charged-current interaction one must distinguish between the initial– and the final–state nucleons and, hence, between their chemical potentials. To obtain the structure factor for the $\bar{\nu}_e$ absorption process, one simply permutes μ_n and μ_p in eq. (59) and substitutes $-\hat{\mu}$ for $\hat{\mu}$ in the $(1-e^{-\beta(\omega+\hat{\mu})})$ term.

6.6. $\nu_i + A \rightarrow \nu_i + A$:

In the post–bounce phase, nuclei exist in the unshocked region and temporarily in a cap of nuclei just exterior to the nucleon/nucleus phase transition near 0.5×nuclear density. However, at the high entropies in shocked protoneutron star atmospheres there are no nuclei. There are alpha particles, but their fractional abundances are generally low, growing to interesting levels due to reassociation of free nucleons just interior to the shock only at late times. Hence, $\nu_i - A$ processes are of secondary importance after bounce, except at the highest neutrino energies for

which the neutrinosphere is exterior to the shock. Nevertheless, for completeness and because it is important during infall and collapse, we include here a discussion of $\nu_i - A$ scattering, with its various corrections.

The differential $\nu_i - A$ neutral–current scattering cross section may be expressed as:

$$\frac{d\sigma_A}{d\Omega} = \frac{\sigma_o}{64\pi}\left(\frac{\varepsilon_\nu}{m_e c^2}\right)^2 A^2 \left\{\mathcal{W}\mathcal{C}_{FF} + \mathcal{C}_{LOS}\right\}^2 \langle \mathcal{S}_{ion}\rangle \left(1+\mu\right) , \tag{60}$$

where

$$\mathcal{W} = 1 - \frac{2Z}{A}(1 - 2\sin^2\theta_W) , \tag{61}$$

Z is the atomic number, A is the atomic weight, and $\langle \mathcal{S}_{ion}\rangle$ is the ion–ion correlation function, determined mostly by the Coulomb interaction between the nuclei during infall (Horowitz 1997).

Leinson *et al.* (1988) have investigated the electron polarization correction, $\mathcal{C}_{LOS}$, and find that

$$\mathcal{C}_{LOS} = \frac{Z}{A}\left(\frac{1 + 4\sin^2\theta_W}{1 + (kr_D)^2}\right) , \tag{62}$$

where the Debye radius is

$$r_D = \sqrt{\frac{\pi\hbar^2 c}{4\alpha p_F E_F}} , \tag{63}$$

$k^2 = |\mathbf{p} - \mathbf{p}'|^2 = 2(\varepsilon_\nu/c)^2(1-\mu)$, p_F and E_F are the electron Fermi momentum and energy, and α is the fine–structure constant ($\simeq 137^{-1}$). Note that $r_D \sim 10\hbar/p_F$ in the ultra–relativistic limit ($p_F >> m_e c$). The $\mathcal{C}_{LOS}$ term is important only for low neutrino energies, generally below ~ 5 MeV.

Following Tubbs and Schramm (1975) and Burrows *et al.* (1981), the form factor term, $\mathcal{C}_{FF}$, in eq. (60) can be approximated by:

$$\mathcal{C}_{FF} = e^{-y(1-\mu)/2} , \tag{64}$$

where

$$y = \frac{2}{3}\varepsilon_\nu^2 \langle r^2\rangle/(\hbar c)^2 \simeq \left(\frac{\varepsilon_\nu}{56\,\mathrm{MeV}}\right)^2 \left(\frac{A}{100}\right)^{2/3} ,$$

and $\langle r^2\rangle^{1/2}$ is the *rms* radius of the nucleus. $\mathcal{C}_{FF}$ differs from 1 for large A and ε_ν, when the de Broglie wavelength of the neutrino is smaller than the nuclear radius.

When $\langle \mathcal{S}_{ion}\rangle = \mathcal{C}_{FF} = \mathcal{C}_{LOS} = 1$, we have simple coherent Freedman (1974) scattering. The physics of the polarization, ion–ion correlation, and form factor corrections to coherent scattering is interesting in its own right, but has little effect on supernovae (Bruenn and Mezzacappa 1997).

6.7. $\nu_i + e^- \rightarrow \nu_i + e^-$:

The differential and total scattering cross sections for $\nu_i - e^-$ scattering are (Sehgal 1974):

$$\frac{d\sigma_{e^-}}{d\varepsilon_{e^-}} = \frac{1}{2}\frac{\sigma_o}{m_e c^2}\left[A_i + \left(1 - \frac{\varepsilon_{e^-}}{\varepsilon_{\nu_i}}\right)^2 B_i\right] \tag{65}$$

and

$$\sigma_{e^-} = \frac{1}{2}\sigma_o \Lambda_i \left(\frac{\varepsilon_{\nu_i}}{m_e c^2} + \frac{1}{2}\right) \ , \tag{66}$$

where

$$\Lambda_i = \frac{1}{4}\left(A_i + \frac{1}{3}B_i\right) \ ,$$

$$A_i = (C_V + C_A)^2 \, ,$$

and

$$B_i = (C_V - C_A)^2 \, .$$

$C_V = 1/2 + 2\sin^2\theta_W$ for ν_e and $\bar{\nu}_e$ neutrinos, $C_V = -1/2 + 2\sin^2\theta_W$ for ν_μ, ν_τ, $\bar{\nu}_\mu$, and $\bar{\nu}_\tau$ neutrinos, $C_A = +1/2$ for ν_e, $\bar{\nu}_\mu$, and $\bar{\nu}_\tau$ neutrinos and $C_A = -1/2$ for $\bar{\nu}_e$, ν_μ, and ν_τ neutrinos. Neutrino–electron cross sections, in particular those for "ν_μ" neutrinos, are small compared to those for ν–nucleon scattering (see §6.4 and §6.3). Generally, neutrino cross sections depend upon the square of the center–of–momentum energy of the neutrino, s, but neutrino–electron cross sections are linear, not quadratic, in ε_{ν_i} because the small mass of the electron makes $s \approx 2\varepsilon_{\nu_i}\varepsilon_{e^-}$. Furthermore, due to the partial electron degeneracy of protoneutron star atmospheres, neutrino–electron cross sections are diminished by final–state electron blocking. We postpone to a later version of our code the proper incorporation of energy redistribution due to ν–e^- scattering and point the reader to Mezzacappa and Bruenn (1993a,b) for a nice discussion of the appropriate numerics.

7. e^+e^- Annihilation

Ignoring phase space blocking of neutrinos in the final state and taking the relativistic limit ($m_e \rightarrow 0$), the total electron–positron annihilation rate into neutrino–antineutrino pairs can be written in terms of the electron and positron phase space densities (Dicus 1972):

$$Q_{\nu_e\bar{\nu}_e} = K_i \left(\frac{1}{m_e c^2}\right)^2 \left(\frac{1}{\hbar c}\right)^6 \int\int \mathcal{F}_{e^-}\mathcal{F}_{e^+}(\varepsilon_{e^-}^4\varepsilon_{e^+}^3 + \varepsilon_{e^-}^3\varepsilon_{e^+}^4)\, d\varepsilon_{e^-}\, d\varepsilon_{e^+} \ , \tag{67}$$

where $K_i = (1/18\pi^4)c\sigma_o(C_V^2 + C_A^2)$. Again, $C_V = 1/2 + 2\sin^2\theta_W$ for electron types, $C_V = -1/2 + 2\sin^2\theta_W$ for mu and tau types, and $C_A^2 = (1/2)^2$. Rewriting eq. (67) in terms of the Fermi integral $F_n(\eta)$, we obtain:

$$Q_{\nu_e\bar{\nu}_e} = K_i\,(kT)\left(\frac{kT}{m_e c^2}\right)^2 \left(\frac{kT}{\hbar c}\right)^6 [F_4(\eta_e)F_3(-\eta_e) + F_4(-\eta_e)F_3(\eta_e)] \ , \tag{68}$$

where $\eta_e \equiv \mu_e/kT$ and

$$F_n(\eta) \equiv \int_0^\infty \frac{x^n}{e^{x-\eta}+1}\,dx\ . \tag{69}$$

Integrating eq. (67), we obtain

$$Q_{\nu_e\bar{\nu}_e} \simeq 9.7615\times 10^{24}\,\left[\frac{kT}{\mathrm{MeV}}\right]^9 f(\eta_e)\ \mathrm{ergs\,cm^{-3}s^{-1}}\,, \tag{70}$$

where

$$f(\eta_e) = \frac{F_4(\eta_e)F_3(-\eta_e)+F_4(-\eta_e)F_3(\eta_e)}{2F_4(0)F_3(0)}\ . \tag{71}$$

For $\nu_\mu\bar{\nu}_\mu$ and $\nu_\tau\bar{\nu}_\tau$ production combined,

$$Q_{\nu_{\mu,\tau}\bar{\nu}_{\mu,\tau}} \simeq 4.1724\times 10^{24}\,\left[\frac{kT}{\mathrm{MeV}}\right]^9 f(\eta_e)\ \mathrm{ergs\,cm^{-3}s^{-1}}\,. \tag{72}$$

One can easily derive the spectrum of the total radiated neutrino energy (ε_T) by inserting a delta function ($\int \delta(\varepsilon_T - \varepsilon_{e^-} - \varepsilon_{e^+})d\varepsilon_T$) into eq. (67). Recall that the total energy of the neutrinos in the final state is equal to the sum of the electron and positron energies in the initial state. Integrating first over ε_{e^+} to annihilate the delta function and then over ε_{e^-} to leave a function of ε_T, one obtains:

$$\frac{dQ}{d\varepsilon_T} = K_i\left(\frac{1}{m_e c^2}\right)^2\left(\frac{1}{\hbar c}\right)^6\int_0^{\varepsilon_T}\varepsilon_T(\varepsilon_T-\varepsilon_{e^-})^3\varepsilon_{e^-}^3\mathcal{F}_{e^-}[\varepsilon_{e^-}]\mathcal{F}_{e^+}[\varepsilon_T-\varepsilon_{e^-}]\,d\varepsilon_{e^-}\ . \tag{73}$$

The numerical evalution of eq. (73) is straightforward. The average of ε_T is equal to:

$$\langle\varepsilon_T\rangle = \Big(\frac{F_4(\eta_e)}{F_3(\eta_e)}+\frac{F_4(-\eta_e)}{F_3(-\eta_e)}\Big)T\,, \tag{74}$$

which near $\eta_e \sim 0$ is $\sim 8T$ and for $\eta_e >> 1$ is $\sim 4T(1+\eta_e/5)$.

However, while the total energy loss rate (eq. 70) and the spectrum of ε_T pose no great mathematical problems, the production spectrum of an individual neutrino is not so easily reduced to a simple integral or to an analytic expression. This is due primarily to the awkward integration of the angular phase space terms, while subject to the momentum conservation delta function, and to the explicit dependence of the matrix elements on the electron/neutrino angles. From Dicus (1972), averaging over initial states and summing over final states, the matrix element for the $e^+e^- \to \nu\bar{\nu}$ process in the $m_e = 0$ limit is:

$$\frac{1}{4}\sum_s |\mathcal{M}|^2 = 16G^2[(C_V+C_A)^2\mathbf{p}\cdot\mathbf{q}_{\bar{\nu}}\,\mathbf{p}'\cdot\mathbf{q}_\nu + (C_V-C_A)^2\mathbf{p}\cdot\mathbf{q}_\nu\,\mathbf{p}'\cdot\mathbf{q}_{\bar{\nu}}]\ , \tag{75}$$

where p and p' are the four-momenta of the electron and positron, respectively, and q_ν and $q_{\bar{\nu}}$ are the four-momenta of the neutrino and antineutrino, respectively. Using the formalism of Bruenn

(1985, correcting for the typo in his eq. C67) and Fermi's Golden rule, expanding the production kernel in the traditional truncated Legendre series, performing the trivial angular integrals, taking the non–trivial angular integrals from Bruenn (1985), and ignoring final–state neutrino blocking, we obtain for the single–neutrino source spectrum due to e^+e^- annihilation:

$$\frac{dQ}{d\varepsilon_\nu} = \frac{8\pi^2}{(2\pi\hbar c)^6}\,\varepsilon_\nu^3 \int_0^\infty d\varepsilon_{\bar\nu}\,\varepsilon_{\bar\nu}^2\,\Phi_0^p(\varepsilon_\nu,\varepsilon_{\bar\nu})\ , \tag{76}$$

where

$$\Phi_0^p(\varepsilon_\nu,\varepsilon_{\bar\nu}) = \frac{G^2}{\pi}\int_0^{\varepsilon_\nu+\varepsilon_{\bar\nu}} d\varepsilon_{e^-}\mathcal{F}_{e^-}[\varepsilon_{e^-}]\mathcal{F}_{e^+}[\varepsilon_\nu+\varepsilon_{\bar\nu}-\varepsilon_{e^-}]\,H_0(\varepsilon_\nu,\varepsilon_{\bar\nu},\varepsilon_{e^-})\ , \tag{77}$$

and

$$H_0(\varepsilon_\nu,\varepsilon_{\bar\nu},\varepsilon_{e^-}) = (C_V+C_A)^2\,J_0^I(\varepsilon_\nu,\varepsilon_{\bar\nu},\varepsilon_{e^-}) + (C_V-C_A)^2\,J_0^{II}(\varepsilon_\nu,\varepsilon_{\bar\nu},\varepsilon_{e^-})\ . \tag{78}$$

The J_0s in eq. (78) come from the more obdurate angular integrals required by the dot products in eq. (75) and the momentum delta function (Bruenn 1985) and have the symmetry:

$$J_0^I(\varepsilon_\nu,\varepsilon_{\bar\nu},\varepsilon_{e^-}) = J_0^{II}(\varepsilon_{\bar\nu},\varepsilon_\nu,\varepsilon_{e^-})\ . \tag{79}$$

From eqs. (76) and (78), we see that the differences between the spectra of the ν_e and ν_μ neutrinos flow solely from their correspondingly different values of $(C_V+C_A)^2$ and $(C_V-C_A)^2$. We use 4–point Gauss–Legendre integration to calculate eq. (77) and 16–point Gauss–Laguerre integration to calculate eq. (76).

At small η_e, the e^+e^- annihilation spectra and total energy loss rates for the ν_e and $\bar\nu_e$ neutrinos are similar, as are the average emitted ν_e and $\bar\nu_e$ neutrino energies. However, as η_e increases, both the total energy radiated in $\bar\nu_e$ neutrinos and the average $\bar\nu_e$ energy start to lag the corresponding quantities for the ν_e neutrinos. This is true despite the fact that the total number of ν_e and $\bar\nu_e$ neutrinos radiated is the same. Figure 1 depicts the relationship between $\langle\varepsilon_i\rangle/T$ and η_e for ν_e, $\bar\nu_e$, ν_μ, and $\bar\nu_\mu$ neutrinos, as well as for the average of the total (eq. 74). Note that if final–state blocking is ignored $\langle\varepsilon_i\rangle/T$ is a function of η_e alone, becoming linear with η_e at high η_e and one half of eq. (74) (~ 4.0) at low η_e. Note also that $\langle\varepsilon_{\nu_\mu}\rangle/T$ and $\langle\varepsilon_{\bar\nu_\mu}\rangle/T$ are closer to one another than are $\langle\varepsilon_{\nu_e}\rangle/T$ and $\langle\varepsilon_{\bar\nu_e}\rangle/T$. Figure 2 depicts our calculation of the e^+e^- annihilation energy spectra for ν_e, $\bar\nu_e$, ν_μ, and $\bar\nu_\mu$ neutrinos at various radii (hence, T, ρ, and Y_e) in the multi–group flux–limited diffusion (MGFLD) calculation of Bruenn and Mezzacappa (see Messer *et al.* 1998) at 106 milliseconds after the bounce of the core of model s15s7b of Weaver and Woosley (1995). Herein, we refer to this snapshot of the Bruenn and Mezzacappa model as our Model BM. In Figure 2, η_e ranges from ~ 1.7 to ~ 5.1. As Figure 2 demonstrates, the individual production spectra vary in peak strength, in peak energy, and in low–energy shape, but they are quite similar on the high–energy tail. Due to the parity–violating matrix element for the $e^+e^- \rightarrow \nu\bar\nu$ process and the fact that η_e is positive, the antineutrino spectra of all species are softer than the neutrino spectra. The pair sums of the integrals under these curves are given by eqs. (70) and (72). For $\eta_e = 0$, 50% of the pair energy emission of electron types is in $\bar\nu_e$ neutrinos, but at $\eta_e = 10$ only 42% of this total energy is in $\bar\nu_e$ neutrinos. However, at $\eta_e = 10$, the

$\bar{\nu}_\mu$ neutrinos still constitute 48.5% of the $\nu_\mu/\bar{\nu}_\mu$ pair emission. These differences reflect differences in the corresponding coupling constants C_V and C_A.

At low η_e, an analytic approximation to the pair source spectrum of the ν_e neutrinos due to Bowers and Wilson (1982), good to about 5% for $\eta_e < 2.0$ and for which $\langle \varepsilon_{\nu_e} \rangle$ is close to half of eq. (74), is

$$\frac{dQ_{\nu_e}}{d\varepsilon_{\nu_e}} \propto \frac{\varepsilon_{\nu_e}^4}{e^{\beta \varepsilon_{\nu_e}} + 1} \,. \tag{80}$$

This approximation breaks down at higher η_es, as Figure 1 clearly implies.

8. $\nu_i \bar{\nu}_i$ Annihilation

In the limit of high temperatures and ignoring electron phase space blocking, the $\nu_i \bar{\nu}_i$ annihilation rate into e^+e^- pairs can be written (Janka 1991):

$$Q_{\nu_i \bar{\nu}_i} = 4 K_i \pi^4 \left(\frac{1}{m_e c^2} \right) \left(\frac{4\pi}{c} \right)^2 \int\int \Phi' \, J_{\nu_i} J_{\bar{\nu}_i} (\varepsilon_{\nu_i} + \varepsilon_{\bar{\nu}_i}) \, d\varepsilon_{\nu_i} \, d\varepsilon_{\bar{\nu}_i} \,, \tag{81}$$

where J_ν is the zeroth moment of the radiation field, ε_ν is the neutrino energy, K_i is defined as before (*i.e.*, $K_i = (1/18\pi^4) c \sigma_o (C_V^2 + C_A^2)$), and

$$\Phi' \left(\langle \mu_{\nu_i} \rangle, \langle \mu_{\bar{\nu}_i} \rangle, p_{\nu_i}, p_{\bar{\nu}_i} \right) = \frac{3}{4} \left[1 - 2 \langle \mu_{\nu_i} \rangle \langle \mu_{\bar{\nu}_i} \rangle + p_{\nu_i} p_{\bar{\nu}_i} + \frac{1}{2} (1 - p_{\nu_i})(1 - p_{\bar{\nu}_i}) \right] \,, \tag{82}$$

where the flux factor $\langle \mu_{\nu_i} \rangle = H_\nu / J_\nu$ and the Eddington factor $p_\nu = \langle \mu_{\nu_i}^2 \rangle = P_\nu / J_\nu$. Eq. (81) can be rewritten in terms of the invariant distribution functions $\mathcal{F}_\nu$:

$$Q_{\nu_i \bar{\nu}_i} = K_i \left(\frac{1}{m_e c^2} \right)^2 \left(\frac{1}{\hbar c} \right)^6 \int\int \Phi' \, \mathcal{F}_{\nu_i} \mathcal{F}_{\bar{\nu}_i} (\varepsilon_{\nu_i}^4 \varepsilon_{\bar{\nu}_i}^3 + \varepsilon_{\nu_i}^3 \varepsilon_{\bar{\nu}_i}^4) \, d\varepsilon_{\nu_i} \, d\varepsilon_{\bar{\nu}_i} \,. \tag{83}$$

Note that when the radiation field is isotropic ($\Phi' = 1$) and when $\eta_e = 0$ the total rate for e^+e^- annihilation given in eq. (67) equals that for $\nu_i \bar{\nu}_i$ annihilation given in eq. (83), as expected.

9. Nucleon–Nucleon Bremsstrahlung

A production process for neutrino/anti-neutrino pairs that has received but little attention to date in the supernova context is neutral-current nucleon–nucleon bremsstrahlung ($n_1 + n_2 \rightarrow n_3 + n_4 + \nu\bar{\nu}$). It importance in the cooling of old neutron stars, for which the nucleons are quite degenerate, has been recognized for years (Flowers, Sutherland, and Bond 1975), but only in the last few years has it been studied for its potential importance in the atmospheres of protoneutron stars and supernovae (Hannestad and Raffelt 1998; Burrows 1997; Suzuki

1993). Neutron–neutron, proton–proton, and neutron–proton bremsstrahlung are all important, with the latter the most important for symmetric matter. As a source of ν_e and $\bar{\nu}_e$ neutrinos, nucleon–nucleon bremsstrahlung can not compete with the charged–current capture processes. However, for a range of temperatures and densities realized in supernova cores, it may compete with e^+e^- annihilation as a source for ν_μ, $\bar{\nu}_\mu$, ν_τ, and $\bar{\nu}_\tau$ neutrinos ("ν_μ"s). The major obstacles to obtaining accurate estimates of the emissivity of this process are our poor knowledge of the nucleon–nucleon potential, of the degree of suitability of the Born Approximation, and of the magnitude of many–body effects (Hannestad and Raffelt 1998; Raffelt and Seckel 1991; Brinkman and Turner 1988). Since the nucleons in protoneutron star atmospheres are not degenerate, we present here a calculation of the total and differential emissivities of this process in that limit and assume a one-pion exchange (OPE) potential model to calculate the nuclear matrix element. To acknowledge ignorance, we encourage that a fudge factor of order unity, but perhaps as low as 0.1, be appended to the rate. The formalism we employ has been heavily influenced by those of Brinkman and Turner (1988) and Hannestad and Raffelt (1998), to which the reader is referred for details and further explanations.

Our focus is on obtaining a useful single–neutrino final–state emission (source) spectrum, as well as a final–state pair energy spectrum and the total emission rate. For this, we start with Fermi's Golden Rule for the total rate per neutrino species:

$$Q_{nb} = \int \Big[\prod_{i=1}^{4} \frac{d^3\vec{p}_i}{(2\pi)^3}\Big] \frac{d^3\vec{q}_\nu}{(2\pi)^3 2\omega_\nu} \frac{d^3\vec{q}_{\bar{\nu}}}{(2\pi)^3 2\omega_{\bar{\nu}}} \omega \sum_s |\mathcal{M}|^2 \delta^4(\mathbf{P}) \mathcal{F}_1 \mathcal{F}_2 (1-\mathcal{F}_3)(1-\mathcal{F}_4)\,, \tag{84}$$

where $\delta^4(\mathbf{P})$ is four–momentum conservation delta function, ω is the energy of the final–state neutrino pair, $(\omega_\nu,\vec{q}_\nu)$ and $(\omega_{\bar{\nu}},\vec{q}_{\bar{\nu}})$ are the energy and momentum of the neutrino and anti–neutrino, respectively, and $\vec{p}_i$ is the momentum of nucleon i. Final–state neutrino and anti–neutrino blocking have been dropped.

The necessary ingredients for the integration of eq. (84) are the matrix element for the interaction and a workable procedure for handling the phase space terms, constrained by the conservation laws. We follow Brinkmann and Turner (1988) for both of these elements. In particular, we assume for the $n + n \rightarrow n + n + \nu\bar{\nu}$ process that the matrix element is:

$$\sum_s |\mathcal{M}|^2 = \frac{64}{4} G^2 (f/m_\pi)^4 g_A^2 \Big[\Big(\frac{k^2}{k^2 + m_\pi^2}\Big)^2 + \ldots \Big] \frac{\omega_\nu \omega_{\bar{\nu}}}{\omega^2} \quad = \quad A \frac{\omega_\nu \omega_{\bar{\nu}}}{\omega^2}\,, \tag{85}$$

where the 4 in the denominator accounts for the spin average for identical nucleons, G is the weak coupling constant, f (~ 1.0) is the pion–nucleon coupling constant, g_A is the axial–vector coupling constant, the term in brackets is from the OPE propagator plus exchange and cross terms, k is the nucleon momemtum transfer, and m_π is the pion mass. In eq. (85), we have dropped $\vec{q}_\nu \cdot \vec{k}$ terms from the weak part of the total matrix element. To further simplify the calculation, we set the "propagator" term equal to a constant ζ, a number of order unity, and absorb into ζ all interaction ambiguities. The constant A in eq. (85) remains.

Inserting a $\int \delta(\omega - \omega_\nu - \omega_{\bar{\nu}})d\omega$ by the neutrino phase space terms times $\omega\omega_\nu\omega_{\bar{\nu}}/\omega^2$ and integrating over $\omega_{\bar{\nu}}$ yields:

$$\int \omega \frac{\omega_\nu \omega_{\bar{\nu}}}{\omega^2} \frac{d^3\vec{q}_\nu}{(2\pi)^3 2\omega_\nu} \frac{d^3\vec{q}_{\bar{\nu}}}{(2\pi)^3 2\omega_{\bar{\nu}}} \rightarrow \frac{1}{(2\pi)^4} \int_0^\infty \int_0^\omega \frac{\omega_\nu^2(\omega - \omega_\nu)^2}{\omega} d\omega_\nu d\omega \,, \tag{86}$$

where again ω equals $(\omega_\nu + \omega_{\bar{\nu}})$. If we integrate over ω_ν, we can derive the ω spectrum. A further integration over ω will result in the total volumetric energy emission rate. If we delay such an integration, after the nucleon phase space sector has been reduced to a function of ω and if we multiply eq. (84) and/or eq. (86) by ω_ν/ω, an integration over ω from ω_ν to infinity will leave the emission spectrum for the single final–state neutrino. This is of central use in multi–energy group transport calculations and with this differential emissivity and Kirchhoff's Law (§5) we can derive an absorptive opacity.

Whatever our final goal, we need to reduce the nucleon phase space integrals and to do this we use the coordinates and approach of Brinkmann and Turner (1988). We define new momenta: $p_+ = (p_1 + p_2)/2$, $p_- = (p_1 - p_2)/2$, $p_{3c} = p_3 - p_+$, and $p_{4c} = p_4 - p_+$, where nucleons 1 and 2 are in the initial state. Useful direction cosines are $\gamma_1 = p_+ \cdot p_-/|p_+||p_-|$ and $\gamma_c = p_+ \cdot p_{3c}/|p_+||p_{3c}|$. Defining $u_i = p_i^2/2mT$ and using energy and momentum conservation, we can show that:

$$\begin{aligned} d^3p_1 d^3p_2 &= 8 d^3p_+ d^3p_- \\ \omega &= 2T(u_- - u_{3c}) \\ u_{1,2} &= u_+ + u_- \pm 2(u_+ u_-)^{1/2}\gamma_1 \\ u_{3,4} &= u_+ + u_{3c} \pm 2(u_+ u_{3c})^{1/2}\gamma_c \,. \end{aligned} \tag{87}$$

In the non–degenerate limit, the $\mathcal{F}_1\mathcal{F}_2(1-\mathcal{F}_3)(1-\mathcal{F}_4)$ term reduces to $e^{2y}e^{-(u_+ + u_-)}$, where y is the nucleon degeneracy factor. Using eq. (87), we see that the quantity $(u_+ + u_-)$ is independent of both γ_1 and γ_c. This is a great simplification and makes the angle integrations trivial. Annihilating d^3p_4 with the momentum delta function in eq. (84), noting that $p_i^2 dp = \frac{(2mT)^{1/2}}{2} u_i^{1/2} du_i$, pairing the remaining energy delta function with u_-, and integrating u_+ from 0 to ∞, we obtain:

$$dQ_{nb} = \frac{Am^{4.5}}{2^8 \times 3 \times 5\pi^{8.5}} T^{7.5} e^{2y} e^{-\omega/T} (\omega/T)^4 \Big[\int_0^\infty e^{-x}(x^2 + x\omega/T)^{1/2} dx \Big] d\omega \,. \tag{88}$$

The variable x over which we are integrating in eq. (88) is equal to $2u_{3c}$. That integral is analytic and yields:

$$\int_0^\infty e^{-x}(x^2 + x\omega/T)^{1/2} dx = \eta e^\eta K_1(\eta) \,, \tag{89}$$

where K_1 is the standard modified Bessel function of imaginary argument, related to the Hankel functions, and $\eta = \omega/2T$. Hence, the ω spectrum is given by:

$$\frac{dQ_{nb}}{d\omega} \propto e^{-\omega/2T} \omega^5 K_1(\omega/2T) \,. \tag{90}$$

It can easily be shown that $\langle\omega\rangle = 4.364T$ (Raffelt and Seckel 1991). Integrating eq. (88) over ω and using the thermodynamic identity in the non–degenerate limit:

$$e^y = \Big(\frac{2\pi}{mT}\Big)^{3/2} n_n/2\,, \tag{91}$$

where n_n is the density of neutrons (in this case), we derive for the total neutron–neutron bremsstrahlung emissivity of a single neutrino pair:

$$Q_{nb} = 2.08 \times 10^{30} \zeta (X_n \rho_{14})^2 (\frac{T}{\rm MeV})^{5.5}\,{\rm ergs\,cm^{-3}\,s^{-1}}\,, \tag{92}$$

where ρ_{14} is the mass density in units of 10^{14} gm cm^{-3} and X_n is the neutron mass fraction. Interestingly, this is within 30% of the result in Suzuki (1993), even though he has substituted, without much justification, $(1 + \omega/2T)$ for the integral in eq. (88). ($[1 + (\pi\eta/2)^{1/2}]$ is a better approximation.) The proton–proton and neutron–proton processes can be handled similarly and the total bremsstrahlung rate is then obtained by substituting $X_n^2 + X_p^2 + \frac{14}{3} X_n X_p$ for X_n^2 in eq. (92) (Brinkmann and Turner 1988). At $X_n = X_p = 0.5$, taking the ratio of augmented eq. (92) to eq. (72), we obtain the promising ratio: $\sim 2\zeta\rho_{13}^2 (6MeV/T)^{3.5}$. Setting the correction factor ζ equal to ~ 0.5 (Hannestad and Raffelt 1998), we find near and just below the ν_μ neutrinosphere, that bremsstrahlung may be comparable to classical pair production.

If in eq. (86) we do not integrate over ω_ν, but at the end of the calculation we integrate over ω from ω_ν to ∞, after some manipulation we obtain the single neutrino emissivity spectrum:

$$\frac{dQ_{nb}}{d\omega_\nu} = 2C\Big(\frac{Q_{nb}}{T^4}\Big)\omega_\nu^3 \int_{\eta_\nu}^{\infty} \frac{e^{-\eta}}{\eta} K_1(\eta)(\eta - \eta_\nu)^2 d\eta = 2C\Big(\frac{Q_{nb}}{T^4}\Big)\omega_\nu^3 \int_1^{\infty} \frac{e^{-2\eta_\nu \xi}}{\xi^3}(\xi^2 - \xi)^{1/2} d\xi\,, \tag{93}$$

where $\eta_\nu = \omega_\nu/2T$, C is the normalization constant equal to $\frac{3\times5\times7\times11}{2^{11}}$ ($\cong 0.564$), and for the second expression we have used the integral representation of $K_1(\eta)$ and reversed the order of integration. In eq. (93), Q_{nb} is the emissivity for the pair.

Eq. (93) is the approximate neutrino emission spectrum due to nucleon–nucleon bremsstrahlung. A useful fit to eq. (93), good to better than 3% over the full range of important values of η_ν, is:

$$\frac{dQ_{nb}}{d\omega_\nu} \cong \frac{0.234 Q_{nb}}{T}\Big(\frac{\omega_\nu}{T}\Big)^{2.4} e^{-1.1\omega_\nu/T}\,. \tag{94}$$

10. Basic Neutrino Transport Results

The formalism and microphysics described in §2 through §9 were used to calculate the neutrino radiation fields for two snapshot profiles in temperature, density, electron fraction, and velocity. One of these is from the work of Burrows, Hayes, and Fryxell (1995) and represents the wind phase that follows explosion (Model W). The second profile (our Model BM) was kindly provided to us by Tony Mezzacappa and is from a multi–group, flux–limited diffusion simulation

by Bruenn (Messer *et al.* 1998), 106 milliseconds after the bounce of the core of the Weaver and Woosley (1995) 15 $M_\odot$ star. Since Messer *et al.* (1998) have already published their results for this model, in order to facilitate comparison we highlight our results for Model BM. Note that our focus is on neutrino atmospheres and not on completely self–consistent profiles and their evolution. Hence, differences between the equations of state and microphysics employed in two different dynamical calculations, in particular any differences between the $\hat{\mu}$s, will translate at a given epoch into differences in composition and thermal profiles. Post–processing one group's snapshots with the code of another can lead to differences in the neutrino fields that are larger than the differences in their thermal profiles. The ν_e and $\bar{\nu}_e$ neutrino luminosity profiles and spectra are particularly sensitive to differences between the $\hat{\mu}$s used and to small differences between the resulting Y_e profiles. To rationalize our results we have turned on the Y_e coupling for about 5 milliseiconds to allow it to relax to our new transport algorithm and its microphysics. This results in more consistent ν_e and $\bar{\nu}_e$ luminosities and spectra.

We concentrate on the generic features of the energy, angle, and spatial distributions of the various neutrino radiation fields. We use 50 energy groups, concentrating them below 50 MeV, so that the emergent spectra are well–resolved. The models have 120 spatial grid points out to a radius of about 300 kilometers and we interpolate in the various original models to resolve important features, such as the neutrinospheres and the shock wave (for Model BM). Since we are using the tangent–ray method to set up and determine the angular grid, we employ from 119 to a few angular groups. In the code, we can establish an arbitrary number of "core rays" in the interior to increase the angular coverage at small radii, but we found that we did not need to exercise this option.

The temperature (T), density (ρ), and Y_e profiles for the two models are shown in Figure 3. Model BM is a pre–explosion protoneutron star in a stalled shock configuration, while Model W is a snapshot of a post–explosion neutrino–driven wind that expands off of the protoneutron star after explosion. In Model W from Burrows, Hayes, and Fryxell (1995), Y_e asymptotes to a value determined by the the competition between ν_e and $\bar{\nu}_e$ neutrino absorption, e^- and e^+ capture on nucleons, and the speed of expansion. This situation is similar to that found in a gas–dynamic laser or freeze out in the early universe. The actual asymptotic Y_e and acceleration timescale will depend, in a self–consistent calculation, on the details of the neutrino–matter coupling and radiation fields and will be the subject of a future paper. Also shown on the lower panel of Figure 3 are the neutron, proton, and alpha particle mass fractions that bear on the physics of wind acceleration and the viability of this wind as a site for the r–process (Woosley and Hoffman 1992; Qian and Woosley 1996).

10.1. Optical Depths and Scattering Albedos versus Radius and Energy

The integrated depth versus radius or interior mass provides a measure of the global context of any transport problem. Figures 4 through 6 show the depth versus radius and neutrino energy for

ν_e, $\bar{\nu}_e$, and ν_μ neutrinos with energies from 5 to 30 MeV in Model BM. This is not the Rosseland mean which, due to the much higher average neutrino energies in the deep interior, reaches a value greater than 10^5 at the center. The position of the shock wave is manifest. Figures 4 through 6 demonstrate that the position of the neutrinosphere ($\tau \sim 2/3$) is a stiff function of neutrino energy. For ν_e neutrinos and the energies depicted in the figures, the radii of the neutrinospheres range from ~ 50 kilometers to $\sim$130 kilometers, more than a factor of two. For the $\bar{\nu}_e$ and ν_μ neutrinos, the range is as broad, though due to the weaker neutrino–matter coupling for these neutrinos the radii are correspondingly smaller. These facts emphasize the dubious merit of referring to a single neutrinosphere for a given species. Figure 7 depicts the positions of the neutrinospheres versus energy and type. In Model BM, while 10 MeV ν_e neutrinos decouple at $\sim$80 kilometers, 100 MeV neutrinos decouple as far out as the position of the shock. This situation has a bearing on the strength of the high–energy spectral tail. Note that for the ν_e and $\bar{\nu}_e$ neutrinos the gain region for Model BM, between $\sim$110 kilometers and the shock, resides at optical depths below ~ 0.1 near the peak of their respective emergent spectra (see §10.2). For slightly higher neutrino energies, the optical depth of this region is correspondingly higher. Hence, energy deposition in this semi–transparent region is problematic and requires a full transport code to study adequately.

Figures 4 through 7 refer to the total optical depth, but while this is a useful measure in transport it is important to distinguish absorption from scattering. The scattering albedo is the a priori probability that an interaction is a scattering (κ_ν/χ_ν). It is a function of composition, neutrino energy, neutrino type, and final–state blocking. For ν_e neutrinos, the excess of neutrons over protons in the free–nucleon, high–entropy region interior to the shock results in an albedo near 0.25, while for the $\bar{\nu}_e$ neutrinos it is $0.5 - 0.6$. Figure 8 depicts the Model BM scattering albedos versus radius as a function of energy for ν_e and $\bar{\nu}_e$ neutrinos. In the interior, the absorption process, $\nu_e + n \rightarrow e^- + p$, is suppressed by blocking due to final–state electrons. This results in an elevated scattering albedo for the lower energy ν_e neutrinos. For ν_μ neutrinos in Model BM, scattering predominates and exterior to 20 kilometers the albedo is above 0.95. This high scattering albedo for the ν_μ neutrinos makes its transport a thermalization depth problem that can not be easily handled with flux limiters.

10.2. Emergent Spectra, Luminosities, and Heating Rates

The emergent neutrino spectra and luminosities are functions of progenitor and they evolve. Generally, the spectra after bounce harden with time (Mayle, Wilson, and Schramm 1987), but after hundreds of milliseconds or as accretion reverses into explosion (or otherwise subsides), the spectra start to soften. The residue then cools inexorably over many seconds, like a clinker plucked from a smelter (Burrows and Lattimer 1986). Our Models are merely snapshots, but they serve as contexts in which to study the influence of various effects and physics. In addition, the results can serve as benchmarks against which to compare those from approximate schemes. The luminosity profiles and spectra for Model BM are depicted in Figures 9 and 10, respectively. The ν_μ neutrino

luminosity includes that due to ν_μ, $\bar{\nu}_\mu$, ν_τ, and $\bar{\nu}_\tau$ neutrinos. The steeper rise and plateau of the ν_μ luminosity is a consequence of the small scattering albedo and deeper point of energy decoupling, even though the $\tau = 2/3$ surface is at larger radii (Figure 6). The peaks in the ν_e and $\bar{\nu}_e$ luminosities mark the inner radius of the gain region, which resides where the luminosity slope is negative. The rapid variation in ν_e luminosity at smaller radii is a consequence of the variation in the temperature slope in the original model, itself presumably a consequence of sparse zoning.

The asymptotic ν_e and $\bar{\nu}_e$ luminosities are 4.3×10^{51} ergs s^{-1} and 3.1×10^{51} ergs s^{-1}, respectively, 13% higher and 9% lower than the corresponding "BOLTZTRAN" numbers from Messer *et al.* (1998). Much of the difference can be ascribed to the slightly different Y_e profile we obtain after relaxation. Our emergent spectra for Model BM are given in Figure 10. The hardness hierarchy of $\nu_e < \bar{\nu}_e < \nu_\mu$ is manifest, as is the dominance of ν_μ neutrinos at high energies. The ν_e and $\bar{\nu}_e$ spectra can be fit by a Fermi–Dirac distribution with temperatures and ηs of 2.22 MeV and 3.16 for the ν_e neutrinos and 2.80 MeV and 3.48 for the $\bar{\nu}_e$ neutrinos. The best Fermi–Dirac fit to the ν_μ neutrino spectrum has a negative η, which might as well be $-\infty$. Note that the emergent ν_μ spectrum shown in Figure 10 was calculated with the bremsstrahlung ζ set equal to one. The dependence of the ν_μ spectrum on ζ will be explored in §10.5.

The corresponding energy–integrated inverse flux factors ($\int J_\nu d\varepsilon / \int H_\nu d\varepsilon$) for Model BM are plotted versus radius in Figure 11. Figure 12 depicts the unintegrated ν_e flux factors (J_ν / H_ν) at given radii versus neutrino energy. Since neutrino–matter heating terms are proportional to J_ν, the higher the flux factor the more efficiently a given energy flux (luminosity) heats the matter in the semi–transparent gain region. Different transport algorithms result in different flux factors, so getting this term right can be important to the viability of the neutrino–driven supernova mechanism (Mezzacappa *et al.* 1998) and to the acceleration and entropy of the post–explosion wind (Burrows 1998a,b). In addition, the harder the spectrum, the stronger the neutrino–matter coupling, so the ν_e and $\bar{\nu}_e$ neutrino spectra versus radius around and exterior to the neutrinospheres have a direct bearing on the heating rate.

Figures 13 and 14 portray the H_ν and J_ν spectra as the ν_e and $\bar{\nu}_e$ neutrinos decouple. As these figures show, at large radii H_ν and J_ν are the same, but at depth J_ν is much larger than H_ν. The precise values of J_ν as the neutrinos decouple determine the matter heating rate. The energy–integrated heating and cooling rates versus radius for Model BM for all neutrino species individually are given in Figure 15. The positions of radiative equilibrium are indicated with a large dot and the inner radius of the gain region for each neutrino is denoted by an X. Note that the gain region identified on Figure 15 coincides with the gain region determined from the luminosity plot (Figure 9). Also included on Figure 15 are the heating rates due to $\nu_e - \bar{\nu}_e$ annihilation and to $\nu_\mu - \bar{\nu}_\mu$ and $\nu_\tau - \bar{\nu}_\tau$ annihilation (eq. 81). Aside from being competitive in the irrelevant unshocked regime, heating due to neutrino pair annihilation is meager, at best. In addition, due to the fuzziness of the neutrinospheres, the heating rate per cm^{-3} does not follow the $1/r^8$ law that might have been appropriate for a sharp neutrinosphere. The difference between the heating and cooling curves, the "net gain," for Model BM is given by a solid line in Figure 16,

to be compared with Figure 8 of Messer *et al.* (1998). We obtain comparable, but slightly more, heating than they.

10.2.1. Neutrino Oscillations

Using the standard neutrino physics, heating due to ν_μ neutrinos is quite modest, as Figure 15 demonstrates. However, if, as the solar and atmospheric neutrino puzzles are indicating, neutrinos oscillate among themselves, then neutrino transport and heating can be altered. Oscillations between the ν_μ and ν_τ types are a wash, since their interactions and spectra are similar. On the other hand, oscillations between ν_e neutrinos and ν_μ or ν_τ neutrinos might indeed alter the magnitude of neutrino–matter heating in the semi–transparent region. The probability that a neutrino has oscillated into another neutrino after traveling a distance L is given by the standard formula:

$$P = sin^2 2\theta_o sin^2\Big(\frac{1.27 \times 10^3 \Delta m^2(\mathrm{eV}) L(\mathrm{km})}{E(\mathrm{MeV})}\Big)\,, \tag{95}$$

where θ_o is the mixing angle. Hence, for the Δm of $\sim 3 \times 10^{-3}$ eV/c^2 suggested for the ν_μ neutrino by one solution to the solar neutrino problem (Suzuki 1998), L_{osc} for a phase change of $\sim \pi$ at a neutrino energy of 10 MeV is $\sim 2 \times 10^3$ kilometers. This is too large to make much difference in core collapse. However, if $\Delta m^2 \sim 3 \times 10^{-3}$ (eV/c^2)^2, as suggested by the atmospheric neutrino data (Totsuka *et al.* 1998), then L_{osc} is a few kilometers at energies of $5 - 20$ MeV. If, contrary to the current thinking, the ν_e neutrinos are involved in the atmospheric deficit, and if mixing is maximal ($sin^2 2\theta_o \cong 1$), then the ν_e spectrum will harden and the neutrino–matter heating rate could be enhanced. However, there are mitigating effects. Oscillation from ν_μ or ν_τ to ν_e neutrinos will also go in the opposite direction. The importance of neutrino oscillations depends upon the relative magnitudes of the oscillation length and the mean–free–paths. If the mean–free–path is smaller than the oscillation length ($1/\chi_\nu < L_{osc}$), then every scattering will reset the oscillation clock and the neutrino will rarely make the transition to its partner. However, as the neutrinos decouple, their mean–free–paths increase, eventually to the point where this inequality must be violated. Hence, at low optical depths, oscillations between either ν_μ or ν_τ and ν_e neutrinos will result in a harder ν_e spectrum and in an enhanced neutrino–matter heating rate in the semi–transparent region. If, on the other hand, the oscillation length is smaller than the mean–free–path (and if the mixing angle is large), then at depth the diffusivity of the two oscillating radiation fields will be similar, though the source strengths will still be very different. In this case, the effective mean–free–path will be something like the average of those of the oscillating pair; the ν_e neutrino will diffuse more quickly and will decouple with a harder spectrum and the ν_μ or ν_τ neutrino will diffuse more slowly and will decouple with a softer spectrum, than if the neutrinos did not oscillate. This situation too is likely to lead to enhanced energy transfer from the inner core to the outer core and, since this is the essence of the neutrino–driven mechanism, there may indeed be interesting consequences for the supernova. Clearly, a fuller study of the possible effects of neutrino oscillations is called for.

10.3. Angular Distributions, Intensities, and Phase–Space Densities

At best, flux limiters only crudely capture the angular distribution of a radiation field above a photosphere. In addition, they do a poor job of providing flux factors and angle–dependent statistical factors and can artificially accelerate the transition from isotropy to free–streaming in the $\tau < 1$ region. This is particularly true for neutrinos, with their extended neutrinospheres. In this light, we present various measures of our derived angular distributions. Figures 17 through 19 portray the Model BM Eddington factors (P_ν/J_ν) versus radius for ν_e, $\bar{\nu}_e$, and ν_μ neutrinos, at particle energies from 5 to 30 or 40 MeV. As we would expect from the decoupling hierarchy, the ν_μ Eddington factors start their rise from the isotropic value of 1/3 from the deepest layers. However, for all neutrino species, particularly for the $\bar{\nu}_e$ and ν_μ neutrinos, the Eddington factor is a stiff function of energy and only gradually makes the transition from 1/3 to 0.75 over a region that can be 50 to 150 kilometers wide. Many flux limiters would effect this same transition within 30 kilometers.

Polar plots depicting the corresponding angular distributions of the Model BM specific intensity (I_ν) fields for a neutrino energy of 15 MeV are given in Figures 20 through 22. The transition from isotropy to forward–peaked is clear, as is the gradual nature of that transition. Complementary to these intensity plots are Figures 23 through 25 of the corresponding phase–space densities ($\mathcal{F}_\nu$) versus energy at various radii and for the various neutrino species. Depicted are the phase–space densities along the 0° and 90° directions. For the ν_e neutrinos, the degree of degeneracy at depth is clear; one can almost read the ν_e chemical potentials off the graph. From Figure 24, we see that the occupancy of the $\bar{\nu}_e$ neutrino states is generically low, but from Figure 25 we see that at depth and for low energies the occupancy of the ν_μ neutrino states can approach 0.5. However, blocking due to final–state ν_μ occupancy is generally unimportant, since the peak energies of the pair source functions are always significantly above the energies at which $\mathcal{F}_\nu$ is high. Hence, the neglect of final–state neutrino blocking in our pair annihilation formalism (§7) is partially supported.

Figures 23 through 25 also convey a sense of the angular dependence of $\mathcal{F}_\nu$. At depth, since the radiation fields are isotropic, the 0° and 90° curves are the same. However, with increasing radius and at lower energies, deviations from isotropy manifest themselves; transverse beams are less occupied than forward beams. As expected, at low optical depths this differential effect is quite pronounced. Using a maximum entropy approach, Cernohorsky and Bludman (1994) have shown that a flux limiter can incorporate the statistics of the transported particle and that there are different preferred limiters for fermions and bosons. However, the differences between these limiters are manifest only at high values of $\mathcal{F}_\nu$. Figures 23, 24, and 25 show that the packing density is sufficiently small at low optical depths that the distinction between the fermion and boson limiters of Cernohorsky and Bludman all but disappears, particularly at the higher energies and for the more transverse directions. Nevertheless, if one did not use a full transport code, it would make sense when following neutrinos to employ a fermion, as opposed to a boson, limiter. We defer a fuller discussion of flux limiters, and how they stack up against Feautrier/tangent-ray

transport, to a later work.

10.4. Consequences of Various Physical Terms

The neutrino radiation fields depend upon terms that incorporate various physical effects. It is conceptually useful to gauge these terms by their influence on the emergent spectra and on the heating rate. Examples of effects that may or may not be included in simpler schemes are the final–state electron blocking term for the charged–current absorption process (§6.1), stimulated absorption corrections (§5), weak magnetism and recoil (§6.1), and the velocity advection, aberration, and Doppler shift terms in the transport equation (eqs. 2 and 4). The ν_e and $\bar{\nu}_e$ neutrino spectra and the net gain for Model BM, with and without the blocking, weak magnetism and recoil, or the stimulated absorption terms, are depicted in Figures 26 and 16, respectively. The blocking correction to the emergent ν_e luminosity is $\sim 15\%$ and that due to stimulated absorption is $\sim -3.5\%$. The blocking and stimulated absorption corrections to the emergent $\bar{\nu}_e$ neutrino luminosity are of opposite sign and approximately equal to -6.0% and 3.5%, respectively. Blocking and stimulated absorption shift the emergent ν_e and $\bar{\nu}_e$ spectra in opposite directions by as much as $\sim$20% and $\sim -8\%$, respectively, due to blocking and $\sim -5.5\%$ and $\sim 6.5\%$, respectively, due to stimulated absorption. Blocking increases the net gain by 10–20%, while stimulated absorption decreases it by less than 5%.

In these Model BM calculations, the effects of weak magnetism and recoil on the emergent ν_e and $\bar{\nu}_e$ neutrino spectra and luminosities are small ($\leq 2.0\%$). This is due to the shift in Y_e during our relaxation step that compensates for what would otherwise be a slight decrease/increase in the $\bar{\nu}_e/\nu_e$ luminosity relative to the value for a frozen model. Similarly, with relaxation, the effect of weak magnetism/recoil on the net gain is almost completely cancelled. Even without relaxation, the increase in the net gain that one would anticipate due to an increase in the $\bar{\nu}_e$ luminosity would be countered by the concommitant decrease in the absorption cross section in the gain region. This result suggests that self–consistent calculations are necessary to accurately gauge the true effect of weak magnetism/recoil. For a frozen model without Y_e relaxation, weak magnetism alters the $\bar{\nu}_e$ luminosity by 10–20%.

The winds that emerge from protoneutron stars after their envelopes supernova are powered by neutrino energy deposition in the expanding gas. Just as with the supernova itself, the wind mass and enthalpy fluxes, velocities, entropies, and compositions are influenced by details of neutrino–matter coupling and neutrino transport. The distribution of the heating determines the magnitude, spatial extent, and timescale of acceleration. In turn, the degree of r–processing in the ejecta is a function of the expansion timescale and the asymptotic Y_e and entropy (Woosley and Hoffman 1992; Qian and Woosley 1996). Hence, it is important to gauge the relative strengths of the various terms that determine the degree and distribution of neutrino–matter heating.

The effect of the velocity terms on the emergent ν_e and $\bar{\nu}_e$ spectra for Model W is depicted in

Figure 27. Model W is the post–explosion wind model from Burrows, Hayes, and Fryxell (1995), in which the velocities at large radii are $\sim 30,000\,\mathrm{km\,s^{-1}}$. Of course, at small radii they are zero. As Figure 27 shows, the velocity effects collectively boost the emergent spectra of Model W by ∼15%, with a corresponding boost in the ν_e and $\bar{\nu}_e$ luminosities by 15% and 13%, respectively. Due to the smaller velocities in the important accretion regions in Model BM, the velocity corrections for that model are much smaller ($\leq 5\%$). Figure 28 shows the net gain in Model W for our fiducial model, as well as without blocking, velocity corrections, or weak magnetism/recoil corrections and implies that various terms not easily or often included in flux–limited or energy–integrated transport can each make a $\sim 10\%$ difference in the parameters of the wind. Note that though the weak magnetism/recoil corrections for Model BM are small, those for Model W are not.

The anisotropy of neutrino–nucleon scattering and the difference between the transport and the total cross sections (eq. 17; §6.3 and §6.4) can in principle translate into larger flux factors and, hence, greater net gain. Backscattering increases J_ν for a given H_ν and delays the transition from isotropic to forward–peaked radiation fields. However, since absorption plays an important role for the ν_e and $\bar{\nu}_e$ neutrinos and their scattering albedos are not very large, the backscatter effect is muted. The upshot is that anisotropy accounts for only $\sim 2\%$ of the net gain and results in shifts of less than 1% in the ν_e or $\bar{\nu}_e$ spectra.

10.5. Determinants of the Emergent ν_μ Spectrum

The ν_μ and ν_τ neutrinos and their antiparticles carry away from the protoneutron star more than 50% of its total binding energy. Since they do not participate in charged–current interactions, they energetically decouple at smaller radii and, hence, at larger temperatures, than the other neutrino species. This results in a harder spectrum (Figure 10) and the hardness hierarchy alluded to in §10.2. The fact that there are four species is primarily responsible for their major cooling role. Neutrino–matter energy coupling is affected by the inverse production processes of pair annihilation (§7 and §8) and nucleon–nucleon bremsstrahlung (§9), as well as by neutrino–nucleon (§6.5) and neutrino–electron scattering. The proper treatment of energy redistribution by scattering is deferred to a later publication. However, it is clear that scattering generically softens the ν_μ spectra.

Ignoring the potential effects of neutrino oscillations (§10.2.1), the emergent ν_μ spectra have a direct bearing on the process of neutrino nucleosynthesis (Woosley *et al.* 1990) and on the suitability of various underground detectors that rely on neutral–current spallation processes with high energy thresholds. In both cases, the relevant neutral–current interaction cross sections are stiffly increasing functions of neutrino energy, with thresholds above ~ 15 MeV (Haxton 1990). Hence, they are most sensitive to the ν_μ component and its precise spectrum. In the past, people had thought that the ν_μ spectra were hard, with effective Fermi–Dirac temperatures of $\sim 8-9$ MeV and average energies of $\sim 25-30$ MeV. However, the ν_μ energy spectrum on Figure 10 can be very approximately fit with a temperature of 7 MeV.

One ambiguity that we address here, parametrized with the ζ in §9, is the actual magnitude of the bremmstrahlung rate. In Figure 10, ζ was set equal to one. The factor ζ incorporates a correction for our approximations to the propagator terms and to the nuclear matrix element. Using Hannestadt and Raffelt (1998) and our own estimates of the correct propagator terms, we derive that above 10^{13} g cm^{-3} ζ is above 0.7 and that at and around 10^{11} g cm^{-3} ζ is near 0.2. This translates into an "average" ζ of ~ 0.5 for protoneutron stars. Figure 29 depicts the consequences of varying ζ from 0 to 1 in steps of 0.2 for the emergent ν_μ energy spectrum. Due to the presence of an absorption term for every emission term (Kirchhoff's Law; eq. 36), the strength of the spectrum is not strictly linear in ζ. As Figure 29 demonstrates, nucleon–nucleon bremsstrahlung is softer than e^+e^- annihilation and can dominate as the ν_μ neutrino source at low energies. Though the emergent spectra are softer, due to the extra source the spectra are also brighter at every energy. Hence, the inclusion of nucleon–nucleon bremsstrahlung increases the flux, while decreasing the average and peak neutrino energies. At 10 MeV, the ν_μ spectrum can be more than a factor of *two* stronger with bremsstrahlung than without. For energies above $\sim$ 35 MeV, e^+e^- annihilation still dominates the emergent spectrum. In Figure 29, the lowest curve corresponds to a pure e^+e^- annihilation source. Note that it is demonstrably harder than when ζ is large and that it alone is "pinched." Though it still remains to be determined whether nucleon–nucleon bremsstrahlung in supernovae is in fact important for ν_μ spectrum formation, Figure 29 suggests that it could well be, particularly at lower neutrino energies. Since energy transfer due to neutrino–matter scattering and gravitational redshifts will only further soften the emergent spectra, we conclude that ν_μ spectra are indeed softer than traditionally quoted.

Note that the thermalization depth effect is difficult to handle with flux limiters when the scattering albedo is large. The albedo for ν_μ neutrinos is above 0.95 throughout most of the object. As a result, only full transport can properly handle the enhancement in the effective absorption path due to the frustrated escape caused by scattering. Also shown on Figure 29 is an emergent ν_μ spectrum with the scattering cross sections very artificially cut by one half. This curve demonstrates the severe dependence of the spectra on the basic numbers associated with the neutrino–matter interaction. It suggests that if we did not have a fairly good handle on the basic interactions of neutrinos with nucleons our predictions would be quite different, and perhaps would be quite wrong.

11. Conclusions

We have constructed and described an implicit, multi–group, multi–angle, multi–species neutrino transfer code to be used in the context of core–collapse supernovae and protoneutron stars. The basic algorithm embodies the Feautrier and tangent–ray approaches to spherical atmospheres and is conceptually equivalent to various Boltzmann solvers. It is capable of resolving angular distributions and of calculating angular moments to great precision and employs accelerated $\mathbf{\Lambda}$ iteration to achieve rapid convergence. In this paper, we discussed or derived

various formulations for the relevant neutrino cross sections and sources. In particular, we derived the rate of nucleon–nucleon bremsstrahlung and its neutrino source spectrum and provided simple forms for the neutrino–nucleon dynamic structure factors. Focusing on "neutrino atmospheres," we presented the energy spectra, Eddington factors, angular distributions, phase space densities, and neutrino heating rates for typical post–bounce structures. The influence on these quantities of various terms in the transport equation and in the microphysics were examined and the character of the neutrino radiation fields and spectra was scrutinized. One goal has been to provide a detailed snapshot of the neutrino radial, angular, energy, and species distributions in a typical post–bounce environment and to explore the factors that determine the heating rates in the semi–transparent gain region, so central to the viability of the neutrino–driven mechanism of supernova explosions. To this end, we focused on the decoupling transition of the emergent neutrinos. For comparison with already–published work, we highlighted a background model from Messer *et al.* (1998).

The tool that we have developed is meant to explore supernova explosions, protoneutron star cooling, the neutrino signature of core–collapse, neutrino shock break–out, and post–explosion winds, among other things. It is also easily converted into a photon transport code for the study of classical supernova light curves. However, we have yet to generalize the scheme for use in multi–dimensional supernova simulations or in the general relativisitic context, nor have we parallelized it for use on shared–memory machines. Hence, much technical work remains.

Supernova theory has been evolving for thirty years and in that time our understanding of the neutrino and its interactions has changed substantially. There are now indications from atmospheric and solar neutrino experiments that lepton number is not strictly conserved and that neutrinos may mix. The potential role of neutrino oscillations in supernovae remains unexplored (§10.2.1). Heating in the protoneutron star mantle is a subtle sum of competing effects. We have investigated in this paper but a few of these. This effort to fully characterize the neutrino radiation fields is part of a larger effort, as yet unfinished, to understand the mechanism of supernova explosions and their systematics. However, when this puzzle box is eventually opened, precise neutrino transport will certainly be one of the keys.

We are pleased to acknowledge Ray Sawyer, Georg Raffelt, Dimitri Mihalas, Tony Mezzacappa, Chuck Horowitz, John Hayes, and Steve Bruenn for useful contributions and guidance. In addition, we extend special thanks to Jorge Horvath for his help with the bremsstrahlung calculations and to Steve Bruenn and Tony Mezzacappa for providing some of their output in electronic form. This work was supported by the NSF under grant AST96-17494 and by the DOE under grant W-7405-ENG-48.

REFERENCES

Aufderheide, M., Fushiki, I., Fuller, G., and Weaver, T. 1994, ApJ, 424, 257

Bethe, H. and Wilson, J.R. 1985, ApJ, 295, 14

Bludman, S.A. and Schinder, P.J., 1988, ApJ, 326, 265

Bowers, R.L. and Wilson, J.R. 1982, ApJS, 50, 15

Brinkmann, R. and Turner, M.S. 1988, Phys. Rev. D, 38, 2340

Bruenn, S.W. 1985, ApJS, 58, 771

Bruenn, S.W. and Mezzacappa, A. 1997, Phys. Rev. D, 56, 7529

Burrows, A. 1997, to be published in the proceedings of the 5'th CTIO/ESO/LCO Workshop entitled "SN1987A: Ten Years Later," eds. M.M. Phillips & N.B. Suntzeff, held in La Serena, Chile, February 24–28, 1997.

Burrows, A. 1998a, in the proceedings of the 9'th Workshop on Nuclear Astrophysics, held at the Ringberg Castle, Germany, March 23–29, ed. E. Müller and W. Hillebrandt, p. 76

Burrows, A. 1998b, in the 18'th Texas Symposium on Relativistic Astrophysics, ed. A. Olinto, J. Frieman, & D. Schramm (World Scientific Press), p. 709

Burrows, A., Hayes, J., and Fryxell, B.A. 1995, ApJ, 450, 830

Burrows, A. and Lattimer, J. M. 1986, ApJ, 307, 178

Burrows, A., Mazurek, T.J., and Lattimer, J.M. 1980, ApJ, 251, 325

Burrows, A. and Sawyer, R.F. 1998, Phys. Rev. C, 58, 554

Burrows, A. and Sawyer, R. 1999, Phys. Rev. C, 59, 510

Cannon, C.J. 1973a, J. Quant. Spectrosc. Rad. Transf., 13, 627

Cannon, C.J. 1973b, ApJ, 185, 621

Colgate, S.A. and White, R.H. 1966, ApJ, 143, 626

Colella, P. and Woodward, P. 1984, J. Comp. Phys., 54, 174

Cernohorsky, J. and Bludman, S. 1994, ApJ, 433, 250

Dicus, D.A. 1972, Phys. Rev. D, 6, 941

Eastman, R. and Pinto, P. 1993, ApJ, 412, 731

Flowers, E., Sutherland, P., and Bond, J.R. 1975, Phys. Rev. D, 12, 316

Freedman, D. Z. 1974, Phys. Rev. D, 9, 1389

Fryxell, B.A., Müller, E., and Arnett, D. 1991, ApJ, 367, 619

Fuller, G. 1982, ApJ, 252, 741

Fuller, G., Fowler, W. A., Newman, M. 1980, ApJS, 42, 447

Hannestad, S. and Raffelt, G. 1998, ApJ, 507, 339

Haxton, W. 1990, Phys. Rev. Lett. , 60, 1999

Herant, M., Benz, W., Hix, R.J., Fryer, C., and Colgate, S.A. 1994, ApJ, 435, 339

Horowitz, C.J. 1997, Phys. Rev. D, 55, 4577

Janka, H.-T. 1991, Astron. Astrophys. , 244, 378

Janka, H.-T. and Müller, E. 1994, Astron. Astrophys. , 290, 496

Janka, H.-T., Keil, W., Raffelt, G., and Seckel, D. 1996, Phys. Rev. Lett. , 76, 2621

Lamb, D.Q. and Pethick, C.J. 1976, ApJ, 209, L77

Leinson, L.B., Oraevsky, V.N., and Semikoz, V.B. 1988, Phys. Lett. B, 209, 80

Lichtenstadt, I., Ron, A., Sack, N., Wagschal, J. J., Bludman, S. A., 1978, ApJ, 226, 222

Mayle, R., Wilson, J.R., and Schramm, D.N., 1987, ApJ, 318, 288

Messer, O.E.B., Mezzacappa, A., Bruenn, S.W., and Guidry, M.W. 1998, ApJ, 507, 353

Mezzacappa, A., *et al.* 1998, ApJ, 495, 911

Mezzacappa, A. and Bruenn, S.W. 1993a, ApJ, 405, 637

Mezzacappa, A. and Bruenn, S.W. 1993b, ApJ, 405, 669

Mihalas, D. 1980, ApJ, 238, 1034

Mihalas, D. and Mihalas, B. 1984, *Foundations of Radiation Hydrodynamics*, New York, Oxford University Press.

Myra, E. and Burrows, A. 1990, ApJ, 364, 222

Olson, G.L., Auer, L.H., and Buchler, J.R. 1986, J. Quant. Spectrosc. Rad. Transf., 35, 430

Qian, Y.-Z. and Woosley, S.E. 1996, ApJ, 471, 331

Raffelt, G. and Seckel, D. 1998, Phys. Rev. Lett. , 69, 2605

Reddy, S., Prakash, M., and Lattimer, J.M. 1998, Phys. Rev. D, 58, no. 013009

Scharmer, G.B. 1981, ApJ, 249, 720

Schinder, P.J. 1990, ApJS, 74, 249

Sehgal, I. 1974, Nucl. Phys., B70, 61

Suzuki, H. 1993, in *Frontiers of Neutrino Astrophysics*, ed. Y. Suzuki and K. Nakamura (Tokyo: Universal Academy Press), p. 219

Suzuki, Y. 1998, Space Science Reviews, 85, 91

Totsuka, Y. *et al.* 1998, to appear in the proceedings of the 19'th Texas Symposium on Relativistic Astrophysics and Cosmology, held in Paris, France, Dec. 14–18, eds. J. Paul, T. Montmerle, and E. Aubourg (CEA, Saclay)

Tubbs, D.L. and Schramm, D.N. 1975, ApJ, 201, 467

Vogel, P. 1984, Phys. Rev. D, 29, 1918

Weaver, T.A. and Woosley, S.E. 1995, ApJS, 101, 181

Woosley, S.E., Hartmann, D., Hoffman, R., and Haxton, W.C. 1990, ApJ, 356, 272

Woosley S.E. and Hoffman, R.D. 1992, ApJ, 395, 202

Yamada, S. 1998, in preparation

Yamada, S., Janka, H.-T., and Suzuki, H. 1999, submitted to ApJ

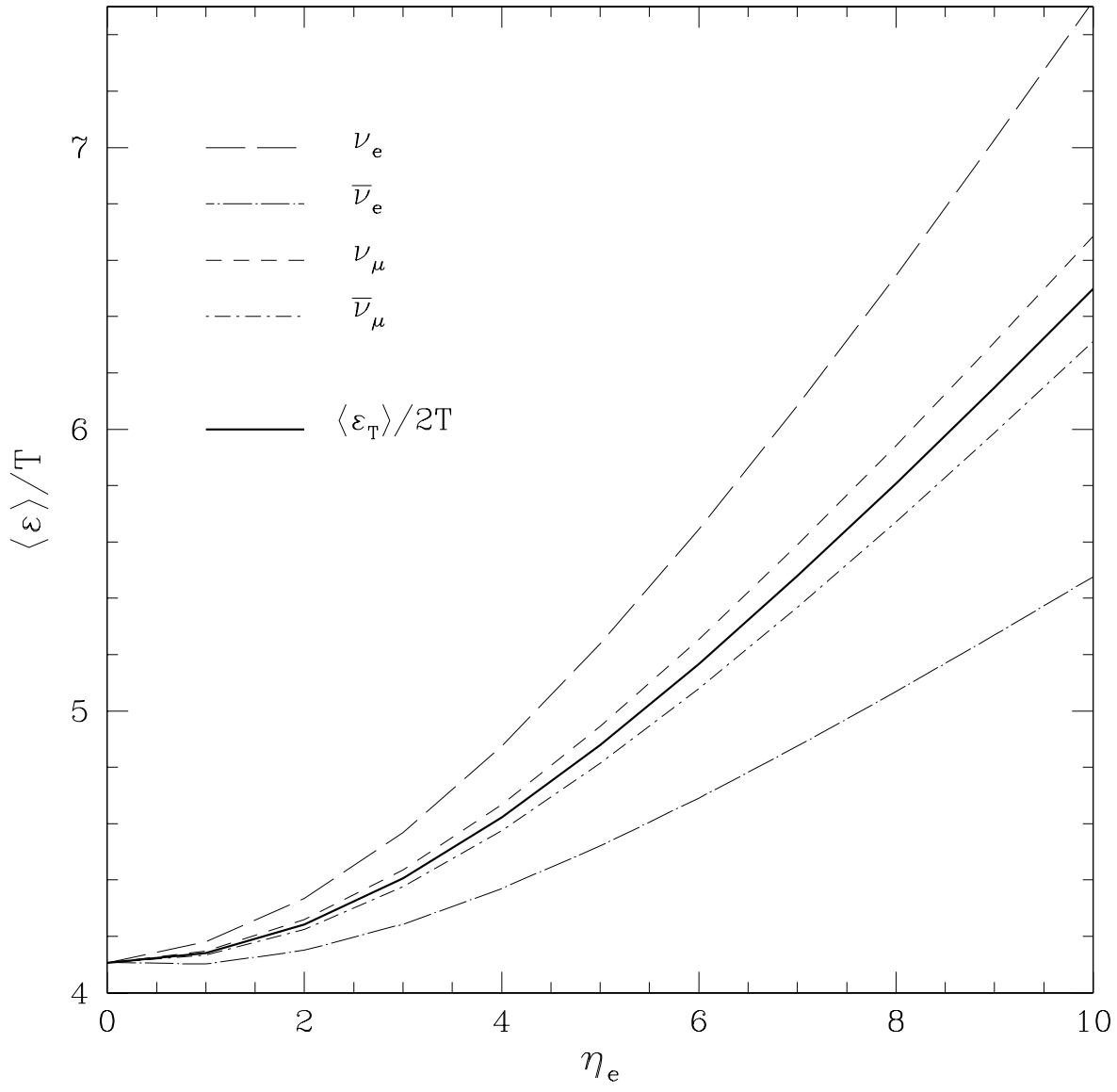

Fig. 1.— The dimensionless average neutrino energy, $\langle\varepsilon\rangle/T$, for all neutrino species from e^+e^- annihilation. We plot $\langle\varepsilon_T\rangle/2T$ to show more clearly that $\langle\varepsilon_{\nu_e}+\varepsilon_{\bar{\nu}_e}\rangle = \langle\varepsilon_{\nu_\mu}+\varepsilon_{\bar{\nu}_\mu}\rangle = \langle\varepsilon_T\rangle$ for all η_es and that these results are independent of temperature.

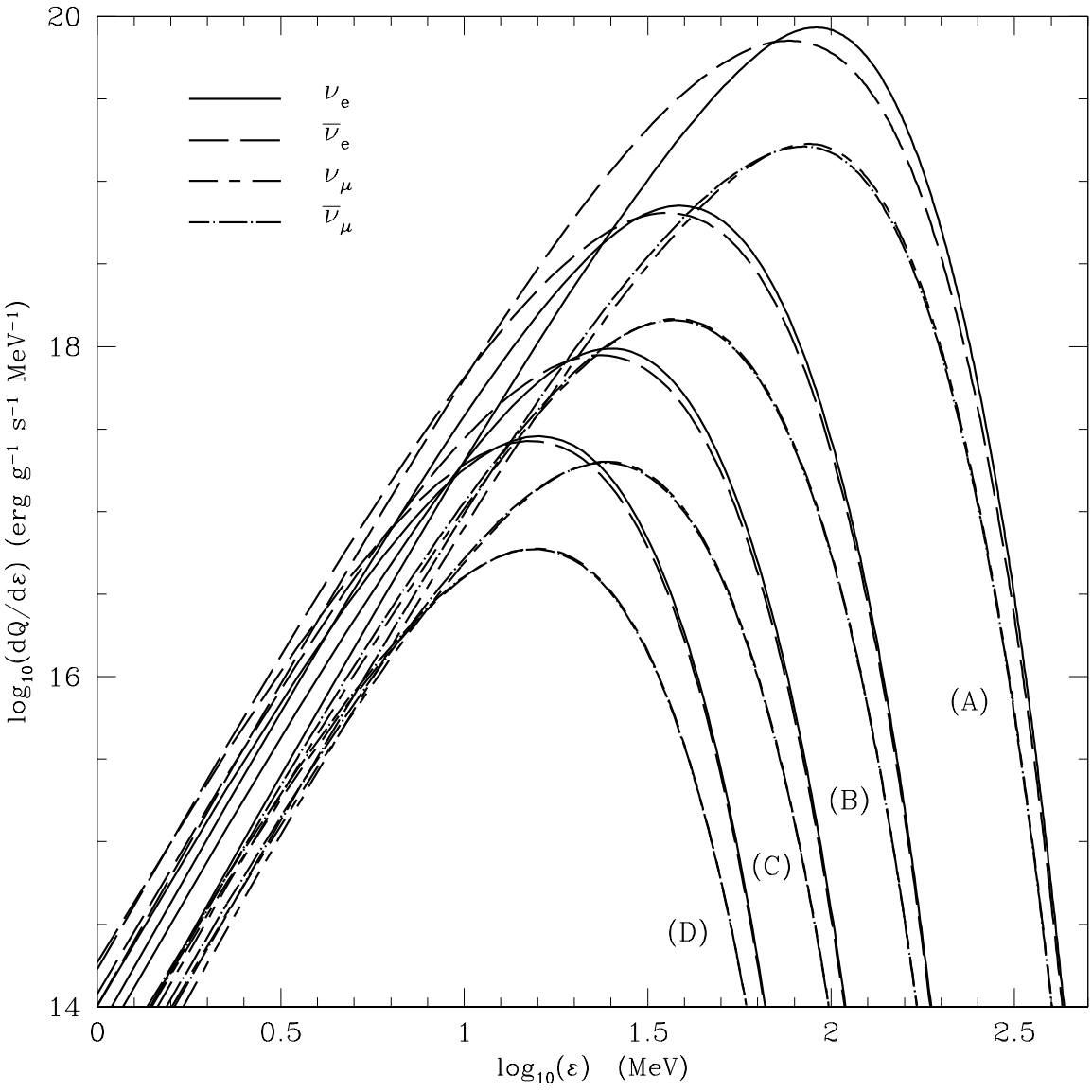

Fig. 2.— The e^+e^- annihilation source spectra for ν_e, $\bar{\nu}_e$, ν_μ, and $\bar{\nu}_\mu$ neutrinos, at a variety of radii in our Model BM from Bruenn and Mezzacappa. Each location is characterized by (A) $R = 14.1$ km, $T = 16.6$ MeV, Y_e=0.23, and $\rho = 2.6 \times 10^{13}$ g cm^{-3}, (B) $R = 34.5$ km, $T = 8.4$ MeV, Y_e=0.11, and $\rho = 2.4 \times 10^{12}$ g cm^{-3}, (C) $R = 46.8$ km, $T = 5.5$ MeV, Y_e=0.10, and $\rho = 6.3 \times 10^{11}$ g cm^{-3}, and (D) $R = 67.0$ km, $T = 3.6$ MeV, Y_e=0.14, and $\rho = 8.6 \times 10^{10}$ g cm^{-3}. Note that the particle and antiparticle spectra are not the same, though the differences between the $\bar{\nu}_\mu$ and ν_μ spectra are smaller than the corresponding differences between the $\bar{\nu}_e$ and ν_e spectra.

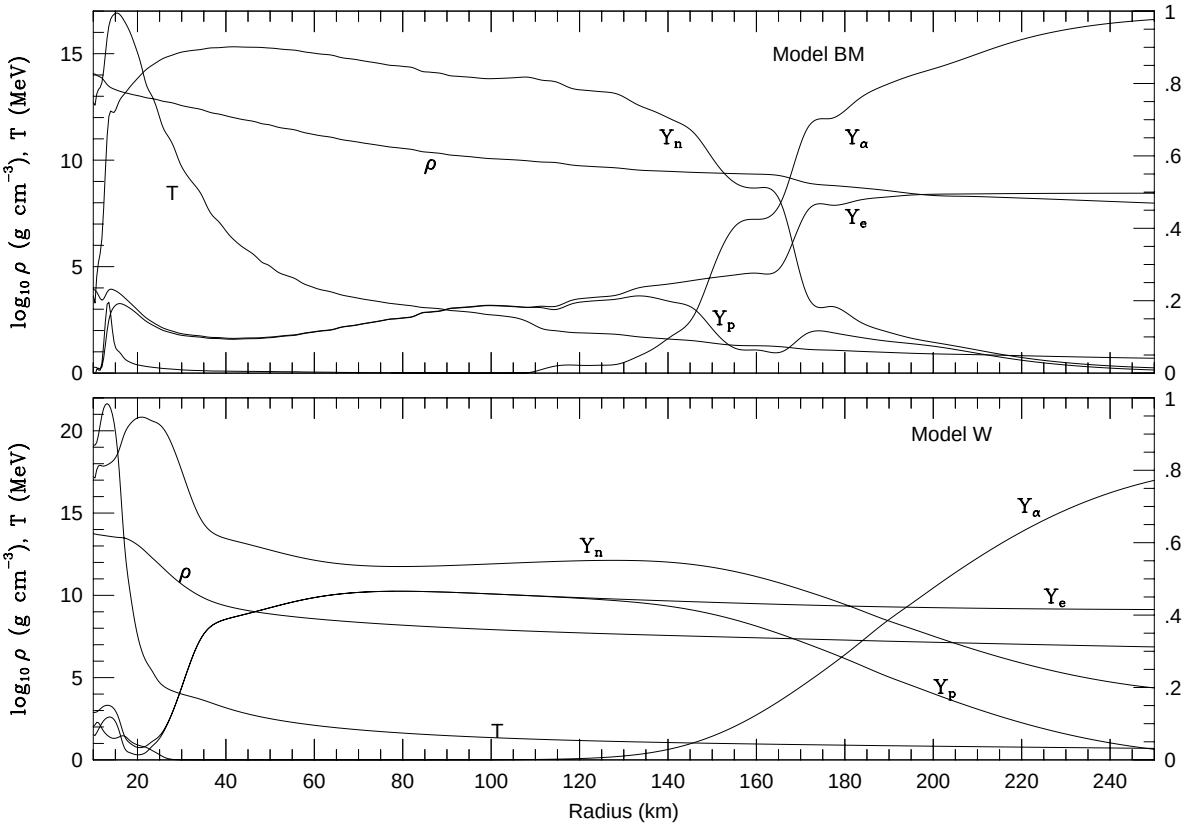

Fig. 3.— The temperature (T), density (ρ), electron fraction (Y_e), proton fraction (Y_p), neutron fraction (Y_n), and alpha fraction (Y_α) for Models BM (top panel) and W (bottom panel). In Model BM, the shock is located at 170 km, but in Model W there is no shock on the grid.

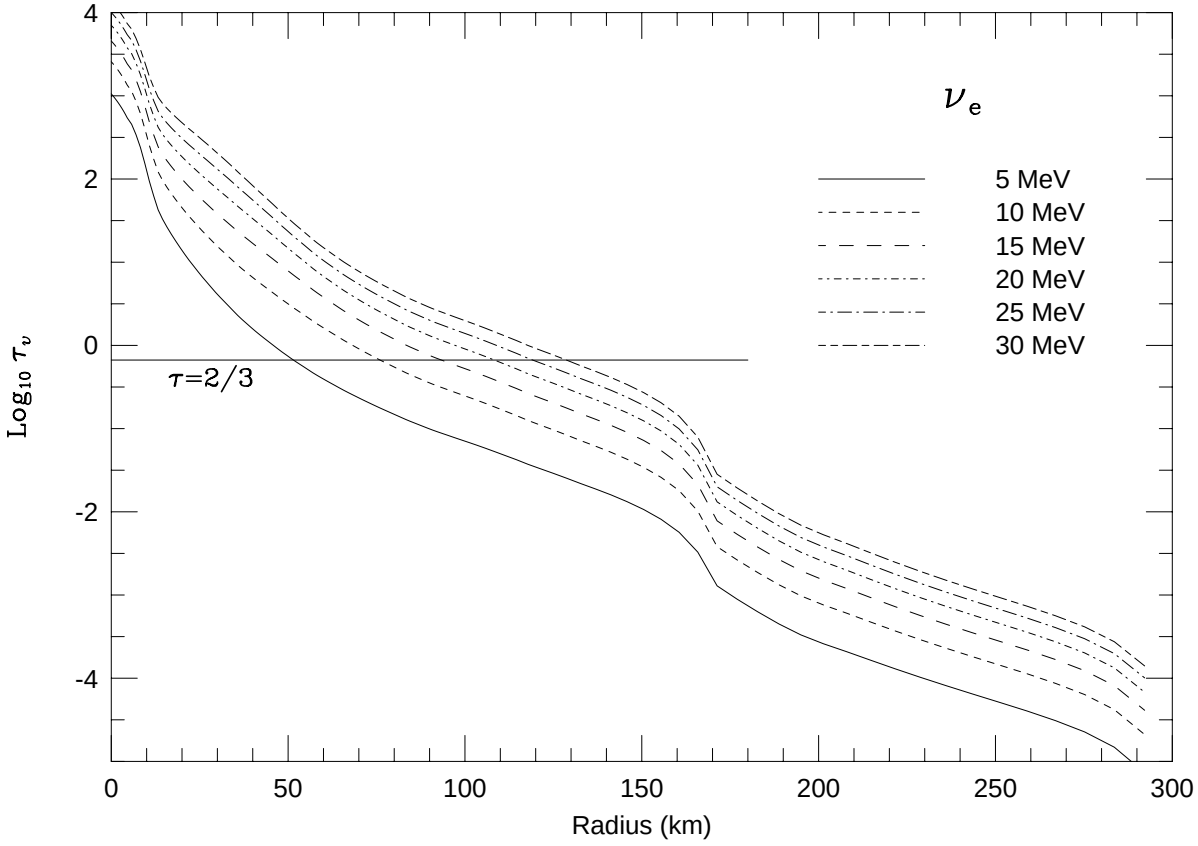

Fig. 4.— The ν_e neutrino optical depth (τ_{ν_e}) versus radius (in kilometers) for Model BM, at various particle energies. As the energy of the neutrino increases the degree of transparency decreases. The dip in the optical depth at 170 km is where the shock (and, hence, a density jump) is located. The solid horizontal line shows where $\tau_{\nu_e} = 2/3$.

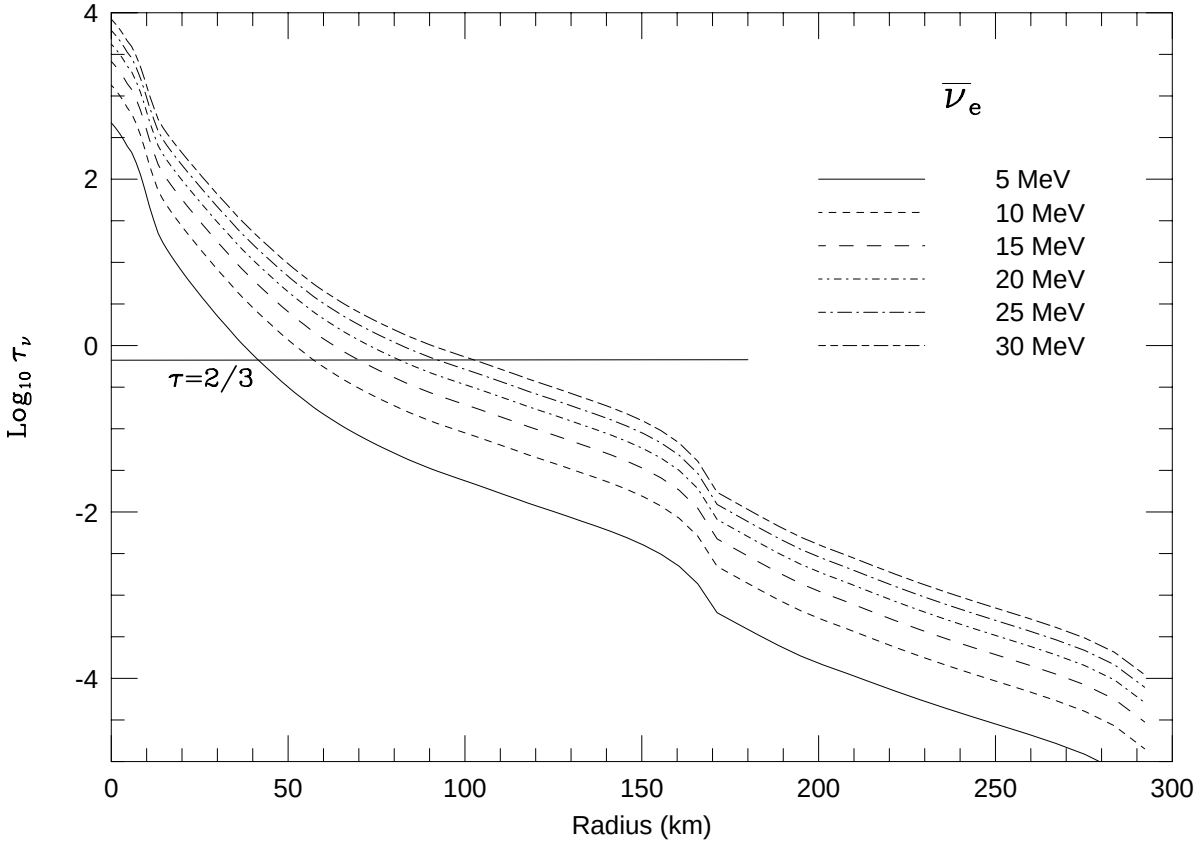

Fig. 5.— Same as Fig. 4, but for $\bar{\nu}_e$ neutrinos.

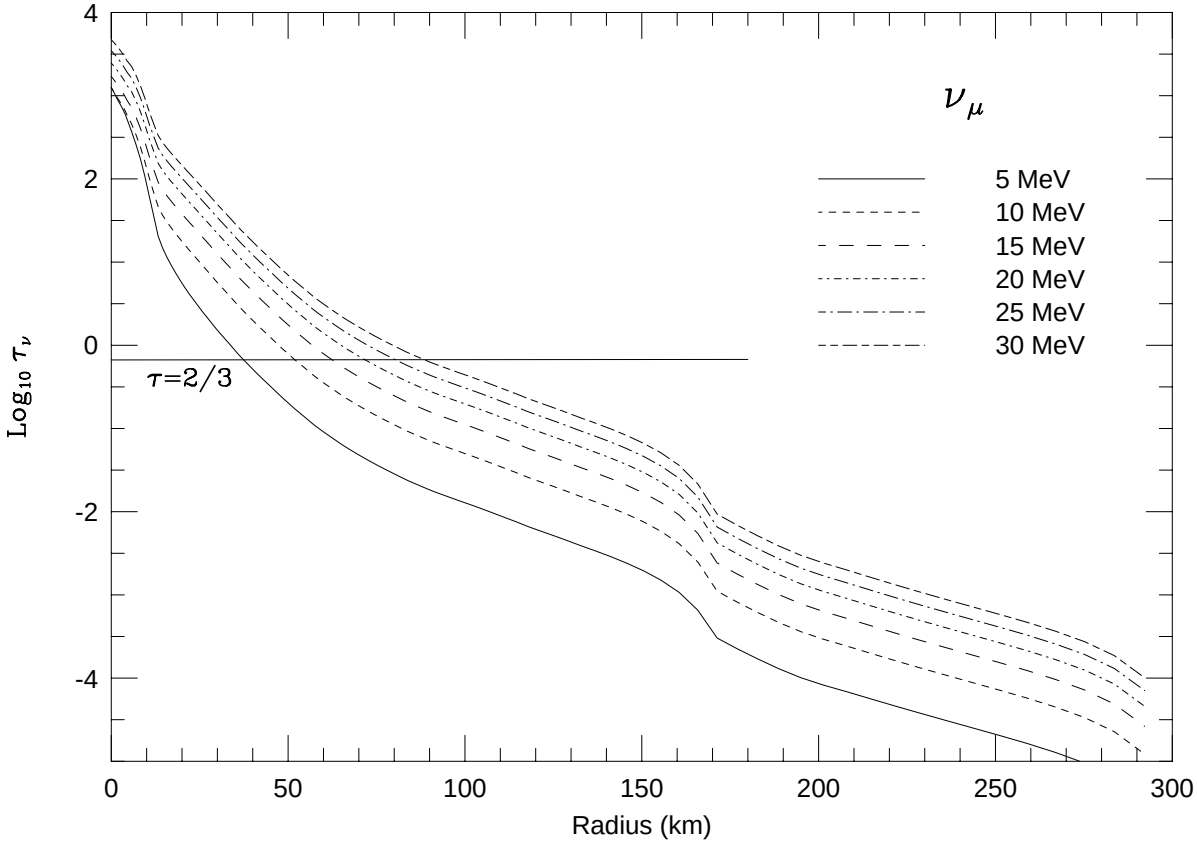

Fig. 6.— Same as Fig. 4, but for "ν_μ" neutrinos.

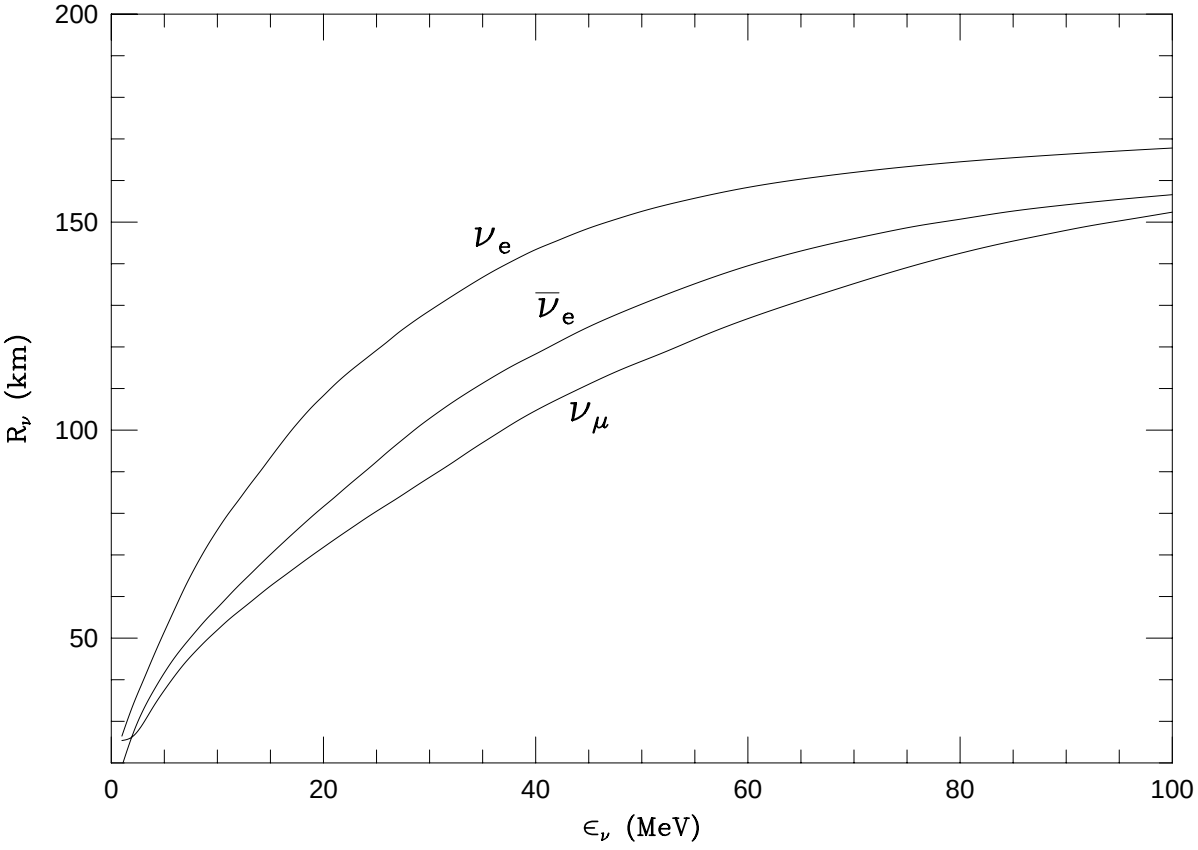

Fig. 7.— The neutrinosphere radii versus neutrino energy for ν_e, $\bar{\nu}_e$, and "ν_μ" neutrinos. For a given neutrino energy, the "ν_μ" neutrinos decouple first, resulting in a $\tau = 2/3$ radius that is smaller than that for either ν_e or $\bar{\nu}_e$ neutrinos. The hierarchy in decoupling radii of $\nu_e > \bar{\nu}_e > \nu_\mu$ is manifest.

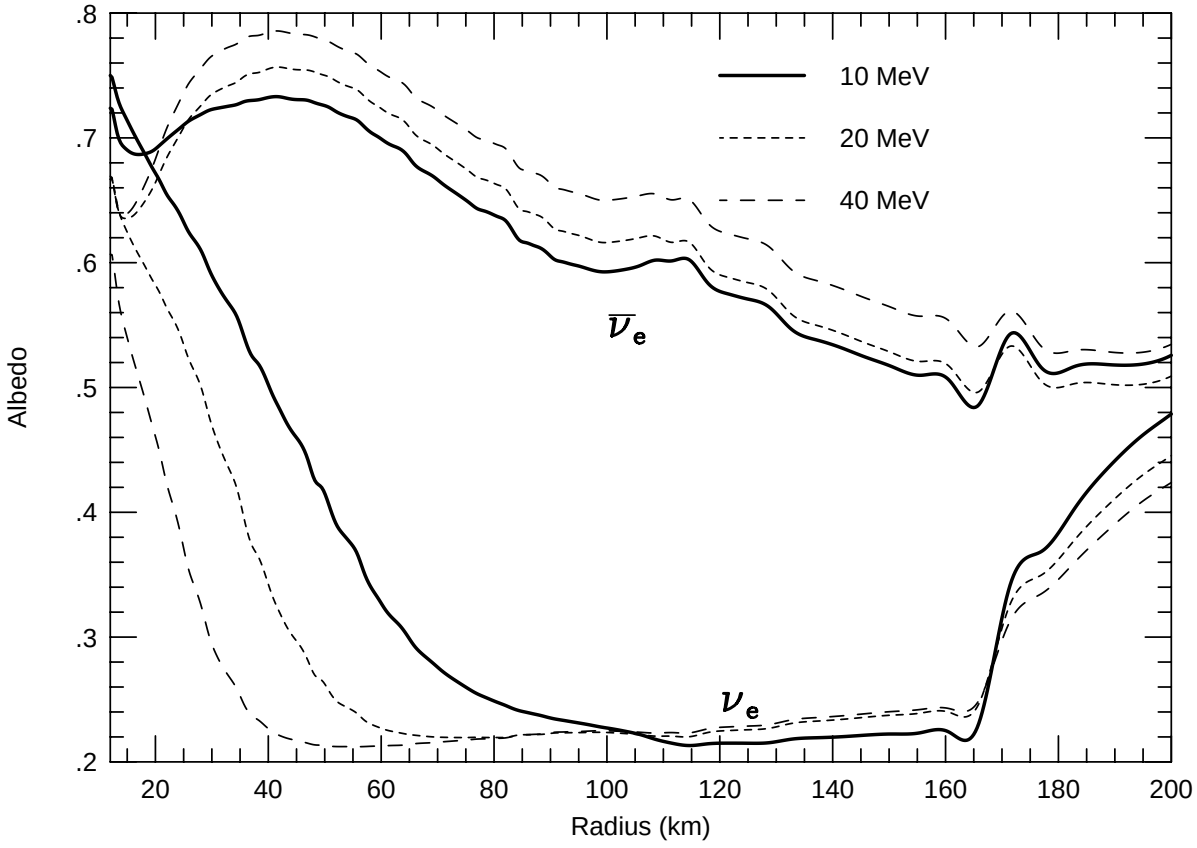

Fig. 8.— The ν_e and $\bar{\nu}_e$ scattering albedos versus radius for neutrino energies of 10, 20, and 40 MeV. The shock is at ∼170 km. The increases in the ν_e albedo at small radii can be traced to e^- blocking of ν_e absorption on neutrons, predominantly.

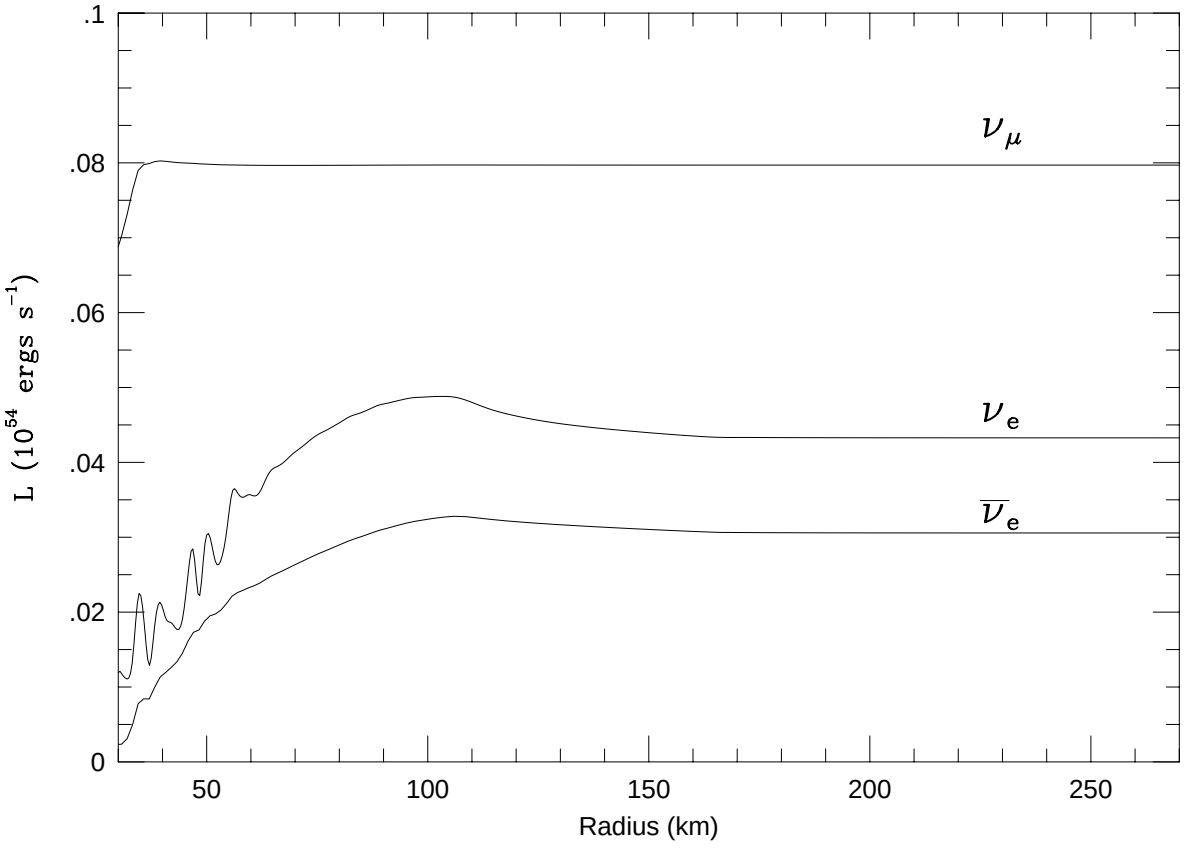

Fig. 9.— Model BM ν_e, $\bar{\nu}_e$, and ν_μ luminosities versus radius (in km). The "ν_μ" luminosity is the sum of the ν_μ, $\bar{\nu}_\mu$, ν_τ, and $\bar{\nu}_\tau$ neutrino luminosities. The modest peaks mark the inner radius of the gain region, in which, due to net absorption, the luminosity slope is gently negative.

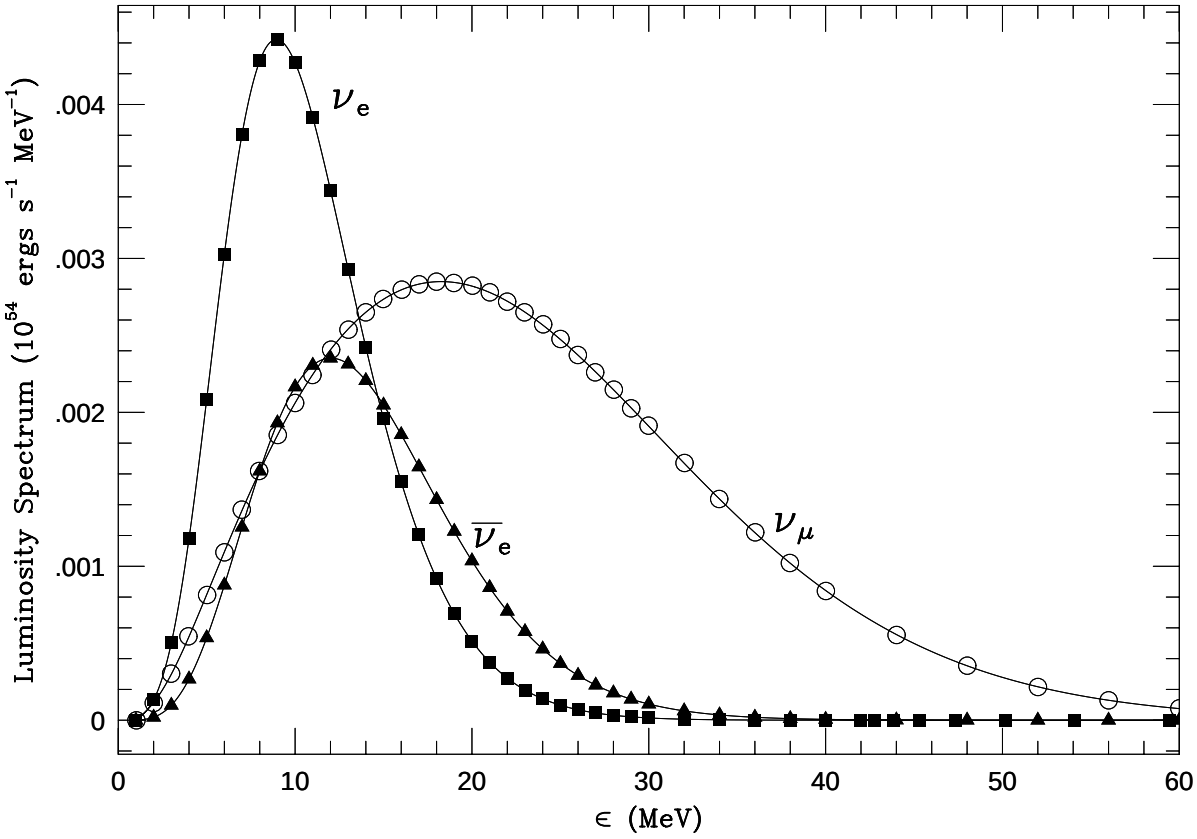

Fig. 10.— The Model BM emergent neutrino luminosity spectra for the three neutrino types. The symbols indicate the positions of the energy groups (ν_e - filled squares; $\bar{\nu}_e$ - filled triangles; ν_μ - open circles).

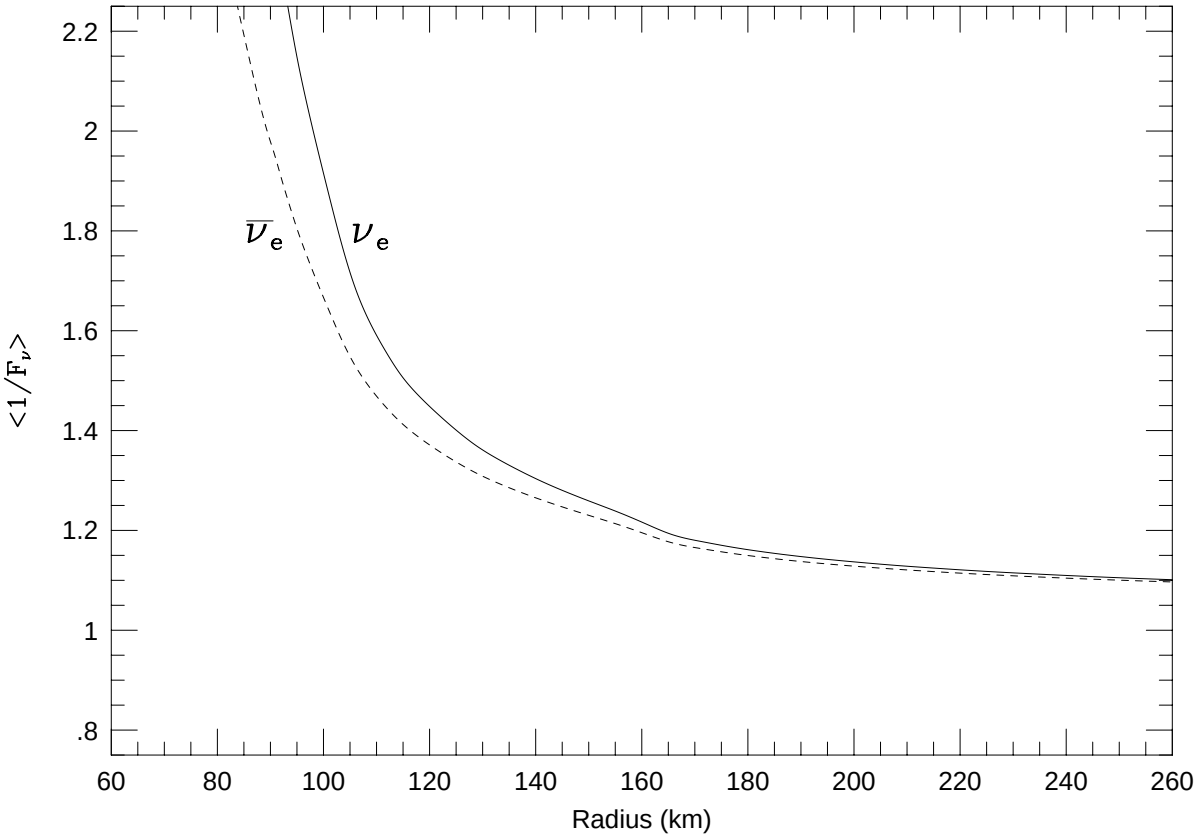

Fig. 11.— The energy–integrated flux factor ($\langle 1/F_\nu \rangle$) as a function of radius for ν_e and $\bar{\nu}_e$ neutrinos. The sharp increase in $\langle 1/F_\nu \rangle$ at 110 km occurs just inside the gain radius, where the neutrinos are starting to decouple from the matter. At large radii (off the plot), the flux factors approach the unity expected for the free–streaming regime.

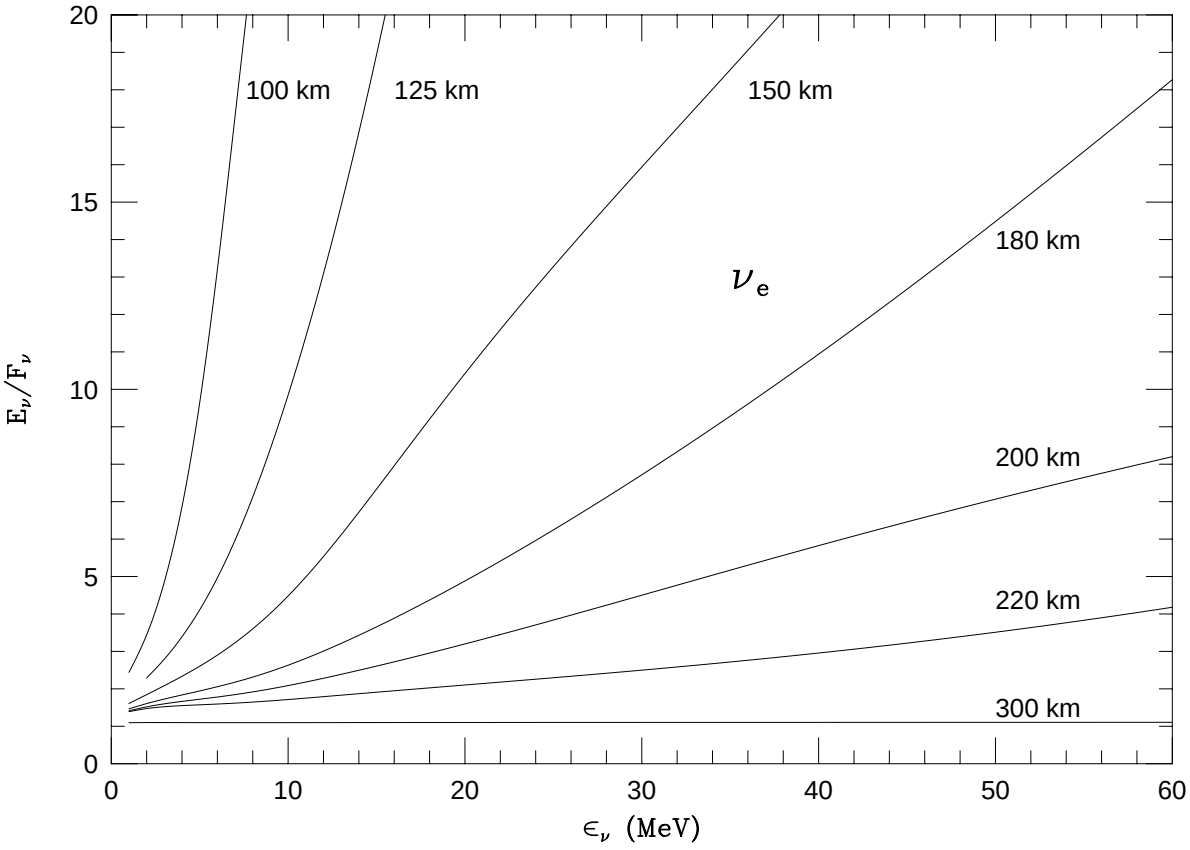

Fig. 12.— The Model BM ratios of the ν_e neutrino energy density to the ν_e energy flux for radii of 100, 125, 150, 180, 200, 220, and 300 km.

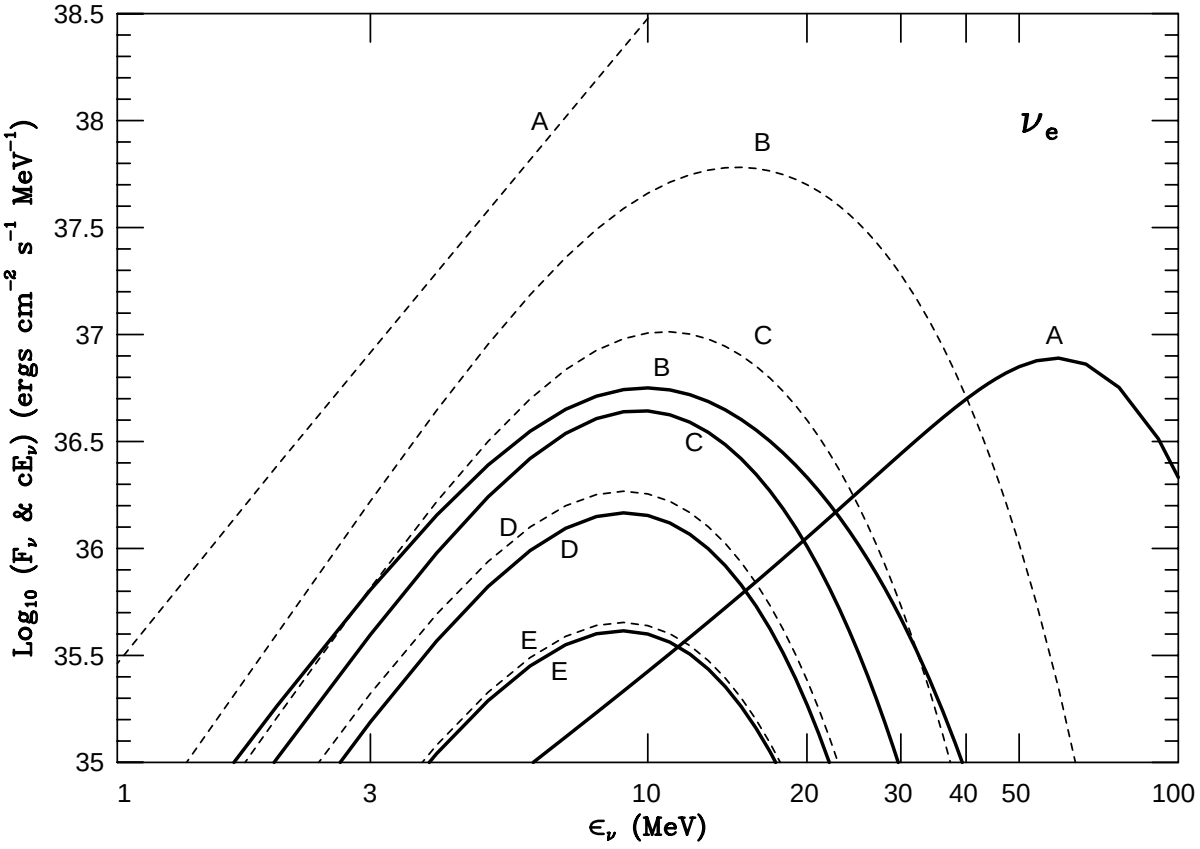

Fig. 13.— The ν_e neutrino energy flux (F_ν, solid) and energy density (cE_ν, dashed) spectra at various radii. A, B, C, D, and E denote radii at 50, 130, 200, 250, and 300 km. At depth, the spectra are very different, but they converge at large distances from the neutrinospheres. At these large distances, the unintegrated flux factor, F_ν/cE_ν, is unity.

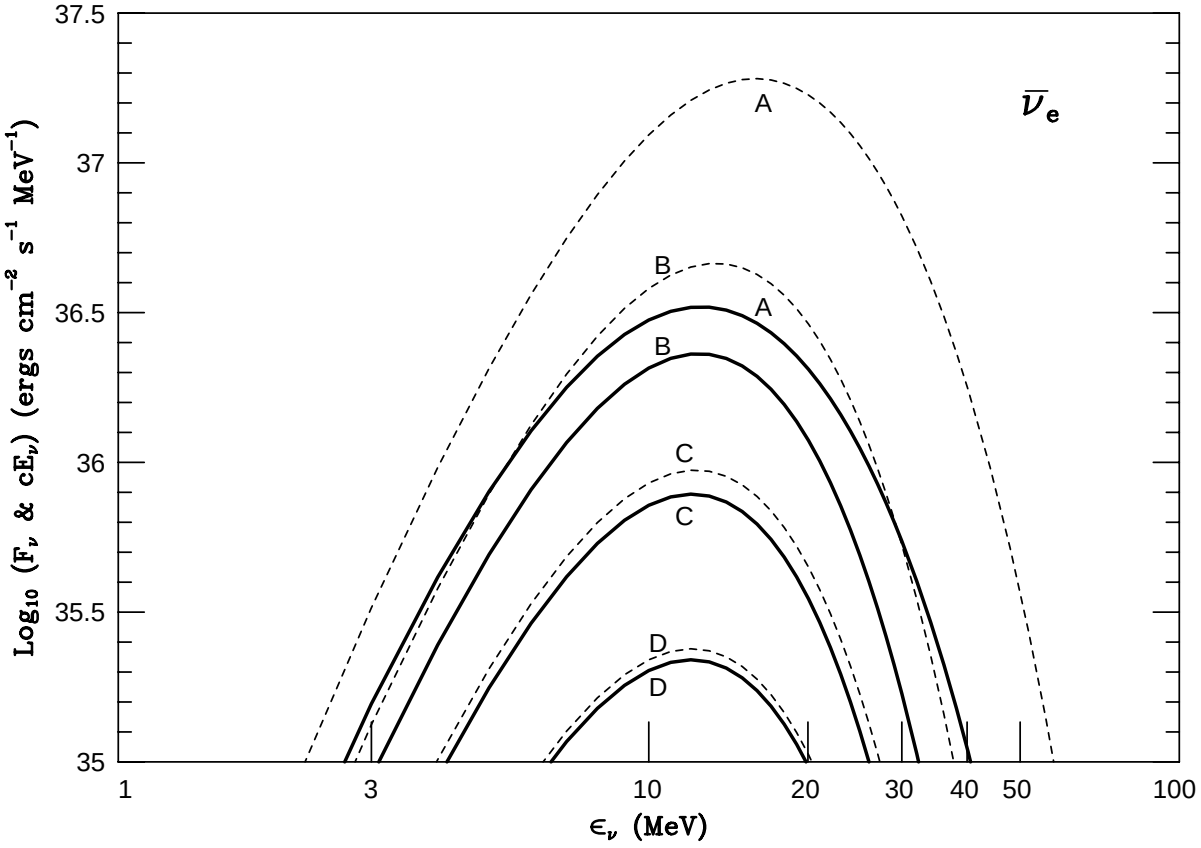

Fig. 14.— The $\bar{\nu}_e$ neutrino energy flux (solid) and energy density (dashed) spectra at various radii. A, B, C, and D denote radii at 130, 200, 250, and 300 km and the energy density has been multiplied by c. This plot is similar to Figure 13, but is for $\bar{\nu}_e$ neutrinos.

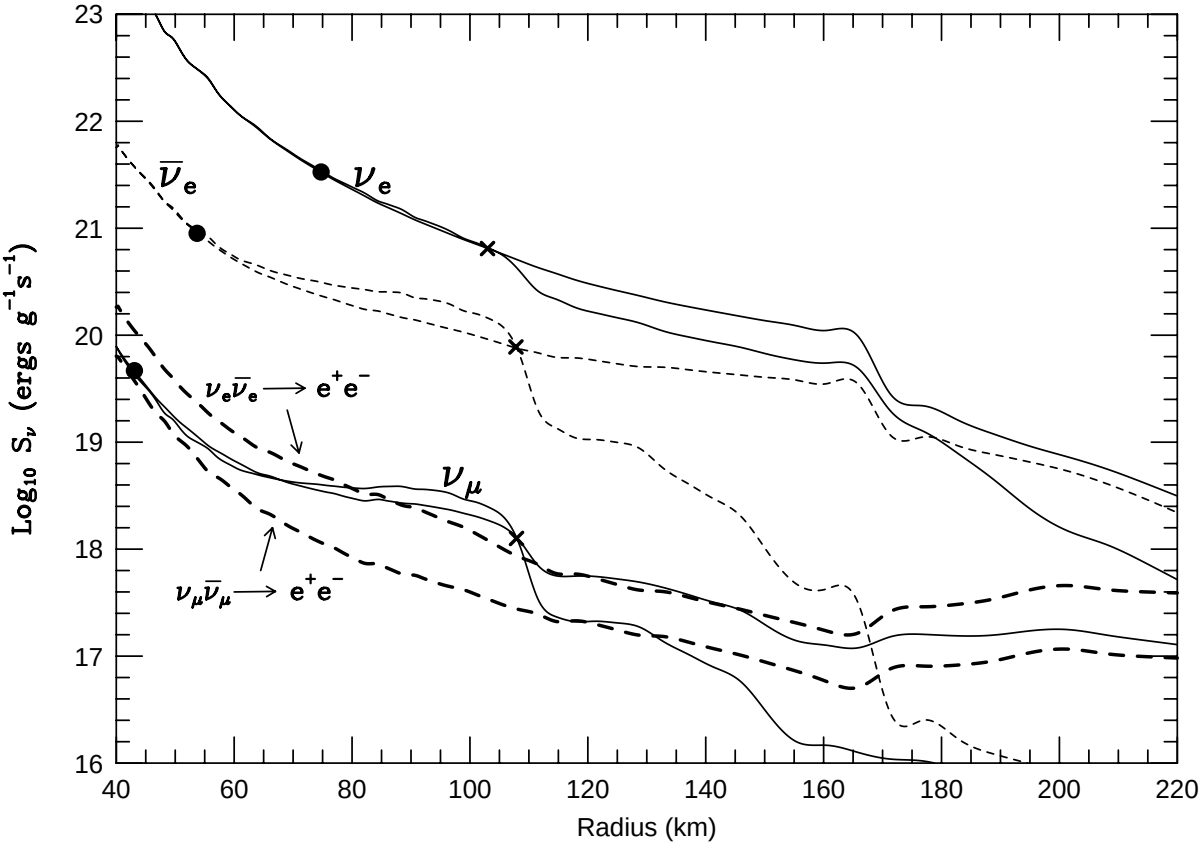

Fig. 15.— Model BM heating and cooling rates (in ergs g^{-1} s^{-1}) versus radius (in km). The heating and cooling rates for the three neutrino species are shown, along with the $\nu - \bar{\nu}$ annihilation energy deposition rates. The solid points indicate where radiative equilibrium is achieved for each neutrino species. The X's indicate the positions of the gain radii for the respective neutrino types. The top two solid lines are the heating and cooling curves for the ν_e neutrinos. The dashed lines are the heating and cooling curves for the $\bar{\nu}_e$ neutrinos. The bottom two solid lines are the heating and cooling curves for ν_μ neutrinos. The bold dashed curves are the heating rates for the $\nu_e\bar{\nu}_e \rightarrow e^+e^-$ process (top) and both the $\nu_\mu\bar{\nu}_\mu \rightarrow e^+e^-$ and $\nu_\tau\bar{\nu}_\tau \rightarrow e^+e^-$ processes (bottom).

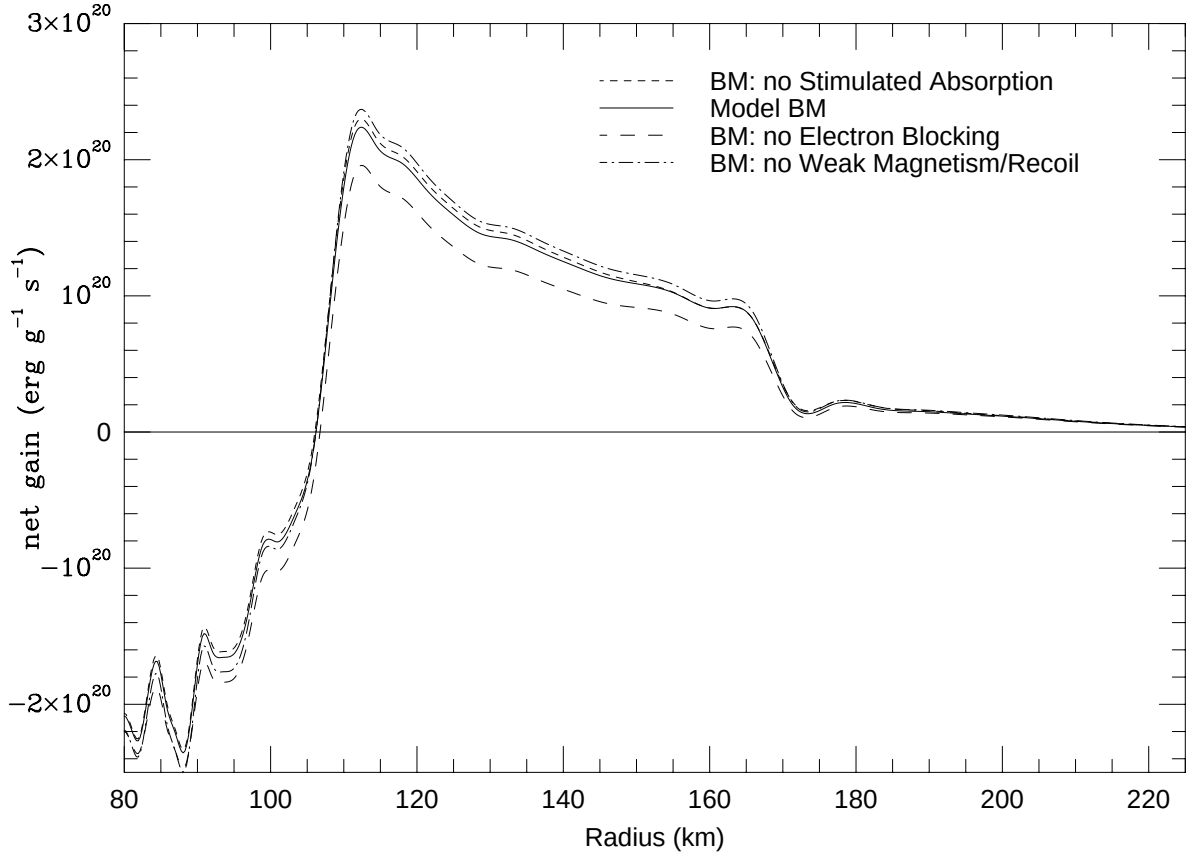

Fig. 16.— The net heating rate (net gain) for various BM models versus radius. The fiducial model (solid) is compared to models with no stimulated absorption (short-dashed line), with no e^- blocking (long-dashed line), or with no weak magnetism/recoil (dot-dashed line). The absence of either stimulated absorption or weak magnetism/recoil would result in an increase in neutrino absorption and, thus, a greater heating rate. The absence of e^- blocking would result in a decrease in the net gain.

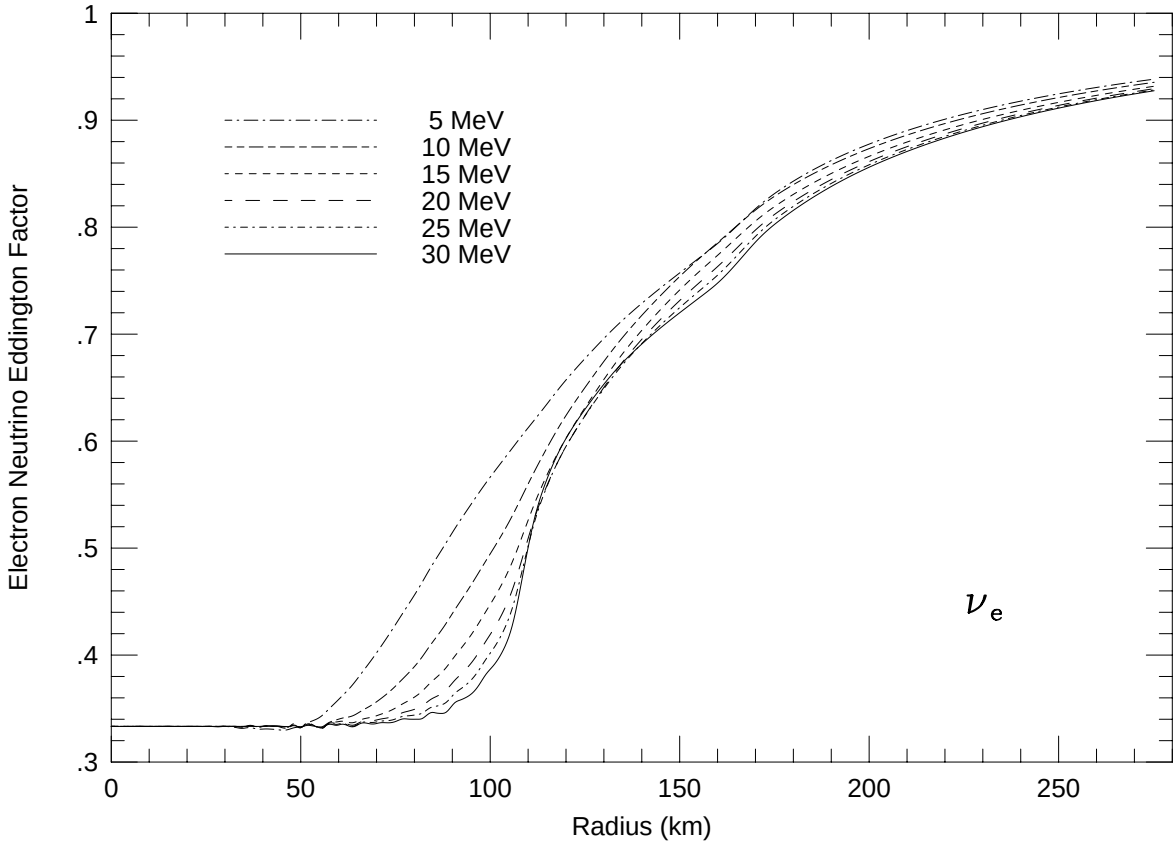

Fig. 17.— The Eddington Factor for ν_e neutrinos versus radius (in km) at various ν_e neutrino energies. At depth, in the diffusive region the Eddington fators converge to 1/3. At large radii, the Eddington factors approach unity. The low–energy neutrinos are the first to decouple and their Eddington factors approach unity faster than those of the higher–energy neutrinos.

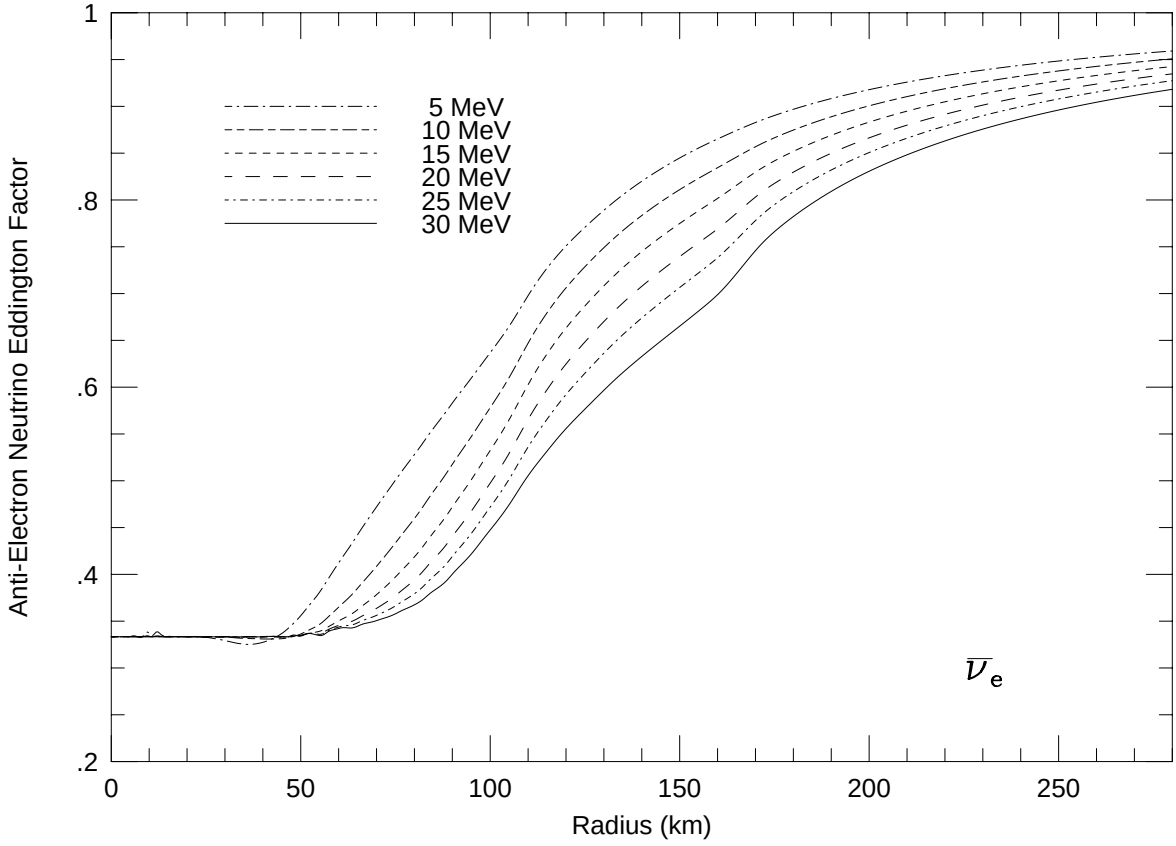

Fig. 18.— Same as Fig. 17, except for $\bar{\nu}_e$ neutrinos.

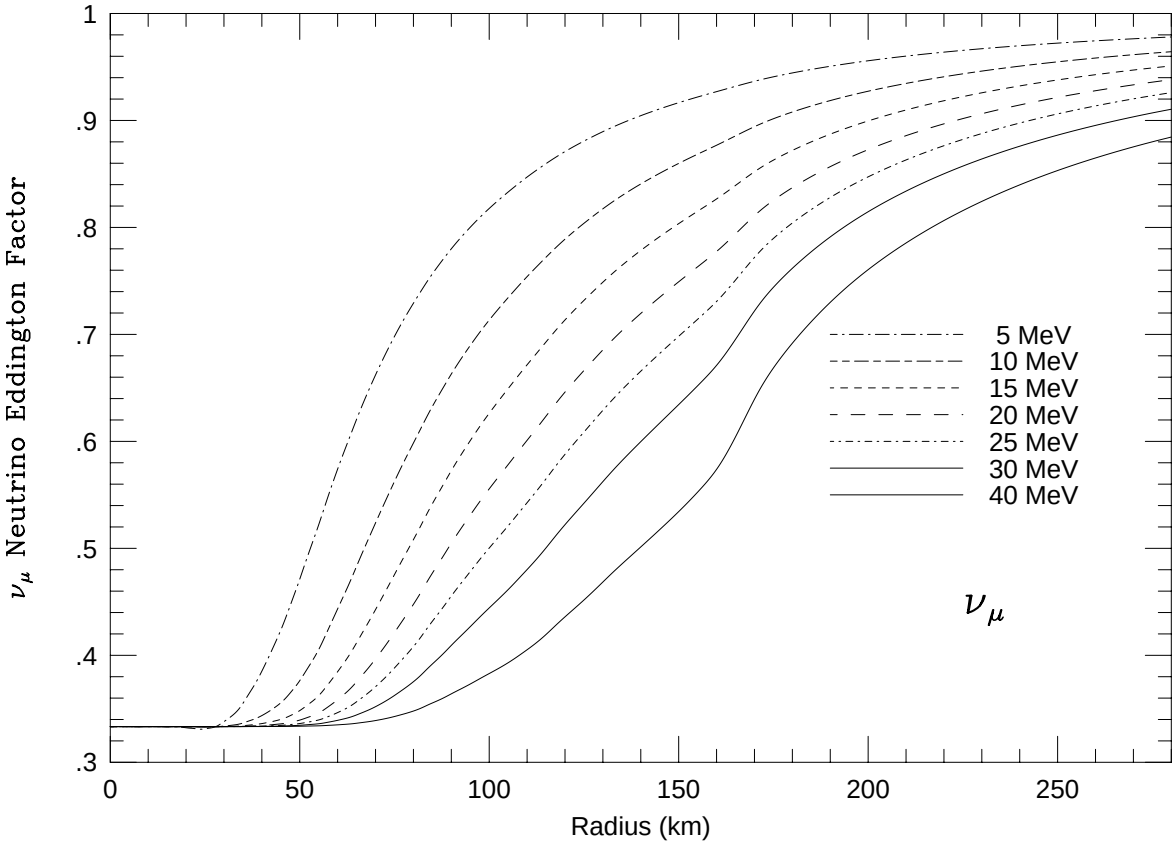

Fig. 19.— Same as Fig. 17, except for the ν_μ neutrinos.

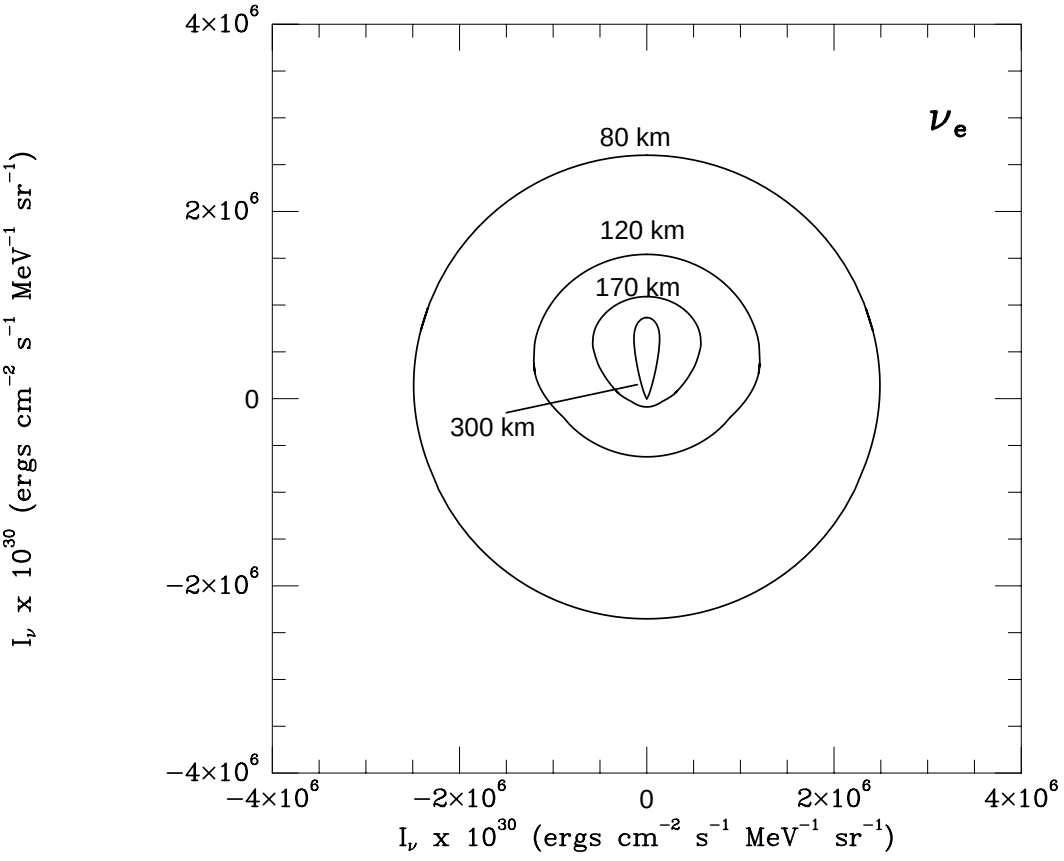

Fig. 20.— Polar plots of the specific intensity (I_ν) of ν_e neutrinos with an energy of 15 MeV. Shown are angular distributions at radii of 80, 120, 170, and 300 km. In the interior, the radiation fields are isotropic and strong. At large radii, the distribution becomes more forward–peaked and geometric dilution decreases I_ν.

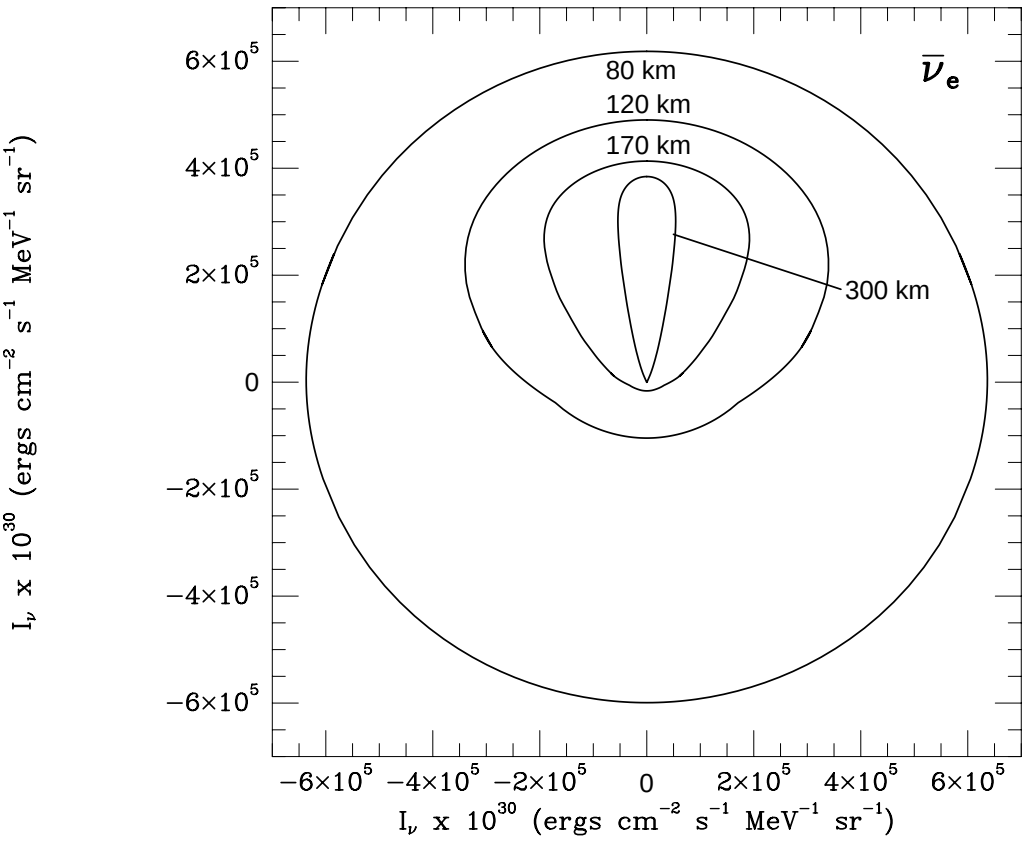

Fig. 21.— Same as Fig. 20, except for $\bar{\nu}_e$ neutrinos.

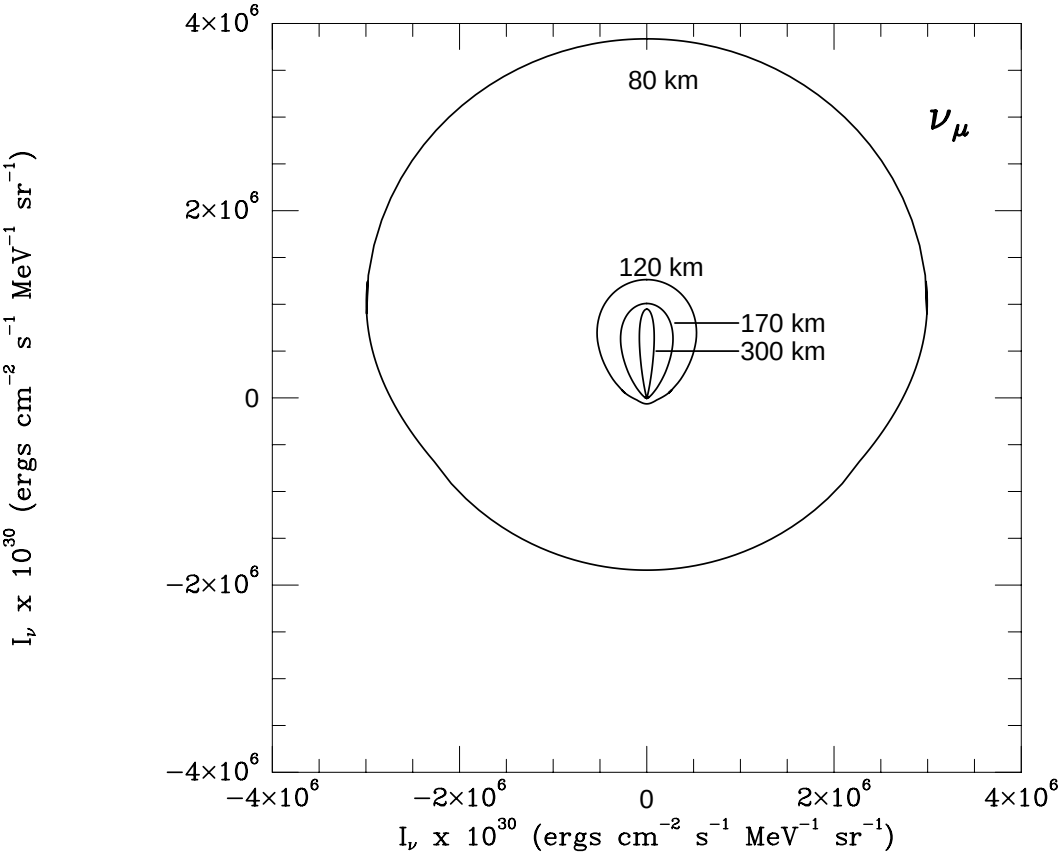

Fig. 22.— Same as Fig. 20, except for ν_μ neutrinos.

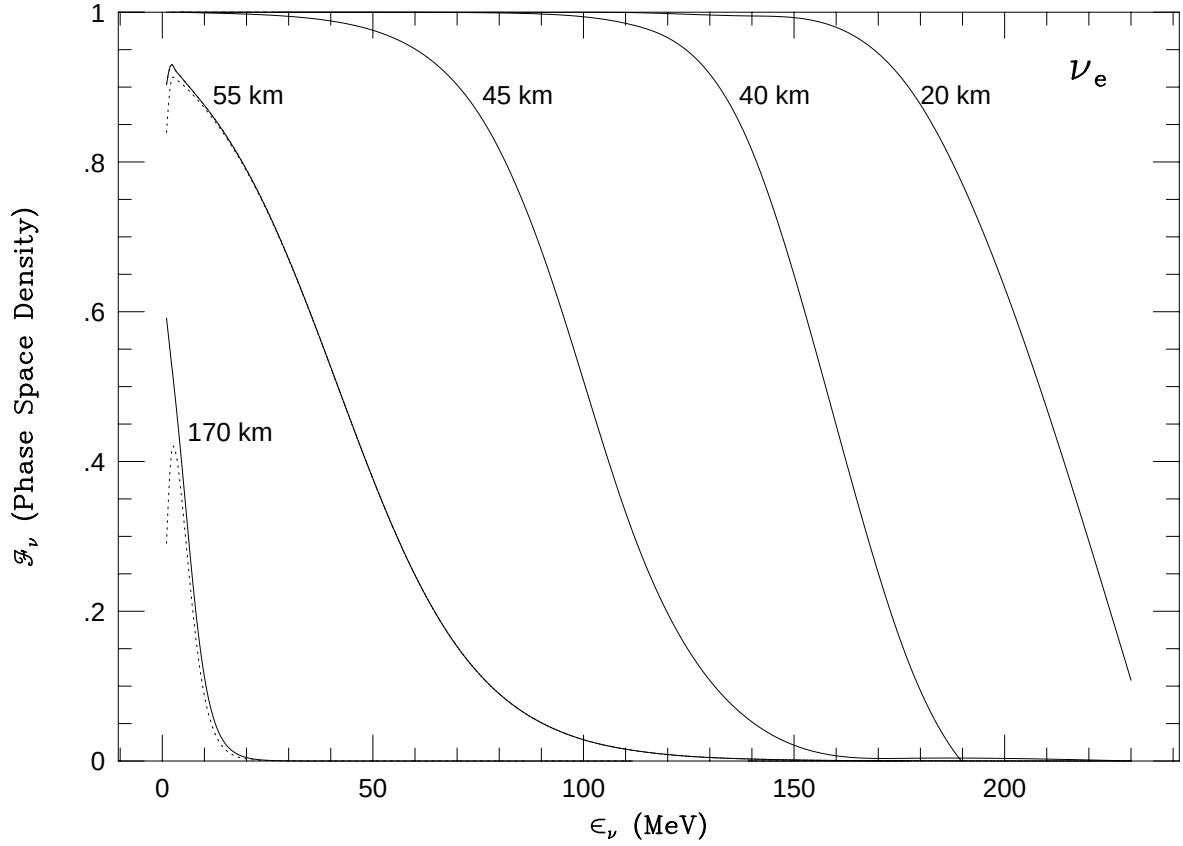

Fig. 23.— The phase–space density ($\mathcal{F}_\nu$) for the ν_e neutrinos versus neutrino energy in MeV, for various radii from 20 km to 170 km. The solid lines are for the forward direction and the dashed lines are for the transverse direction (at $\sim 90^\circ$ to the radial direction). At small radii, the ν_e neutrinos are degenerate, but at larger radii, and generally at larger energies, they quickly become non–degenerate. Note that at small energies, "larger" radii, and large angles, the degeneracy of the ν_e neutrinos diminishes.

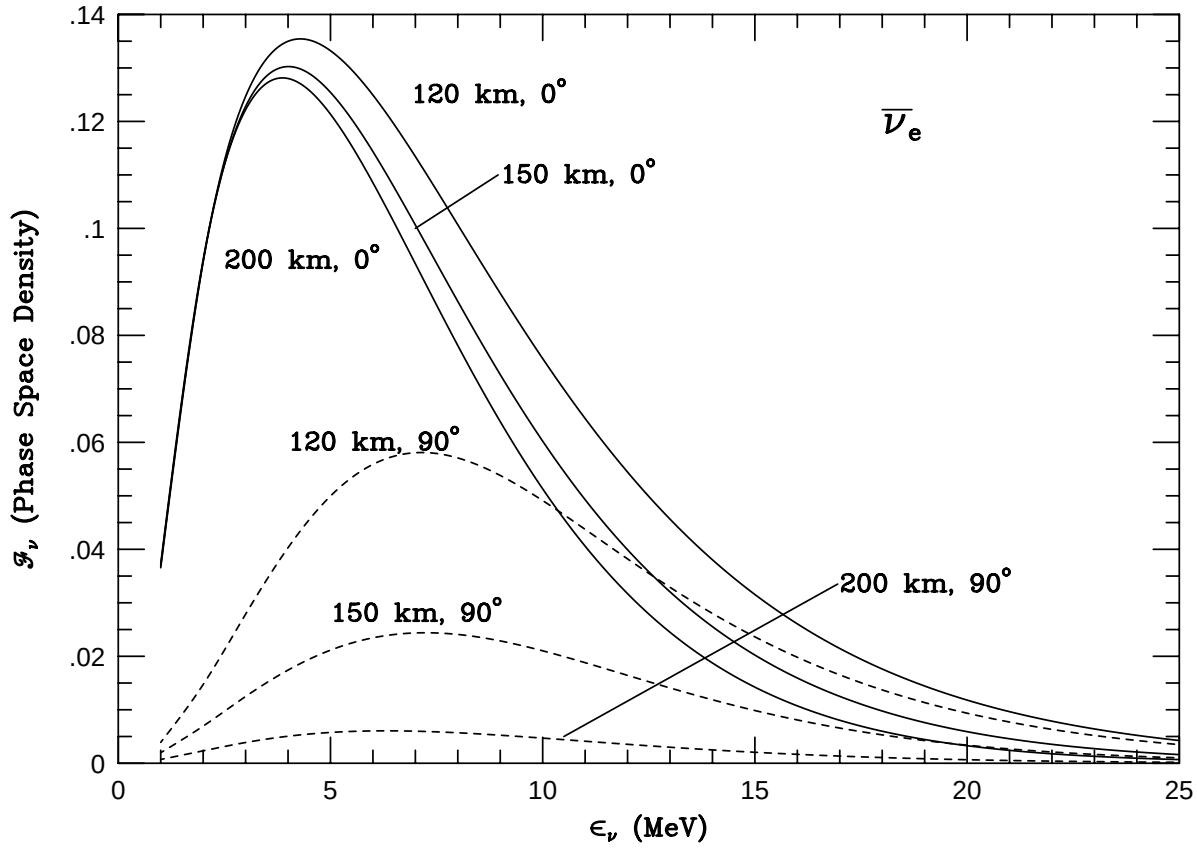

Fig. 24.— The phase–space density ($\mathcal{F}_\nu$) for the $\bar{\nu}_e$ neutrinos versus neutrino energy in MeV, at radii of 120, 150, and 200 km. The solid lines are for the forward direction and the dashed lines are for the transverse direction (at $\sim 90°$).

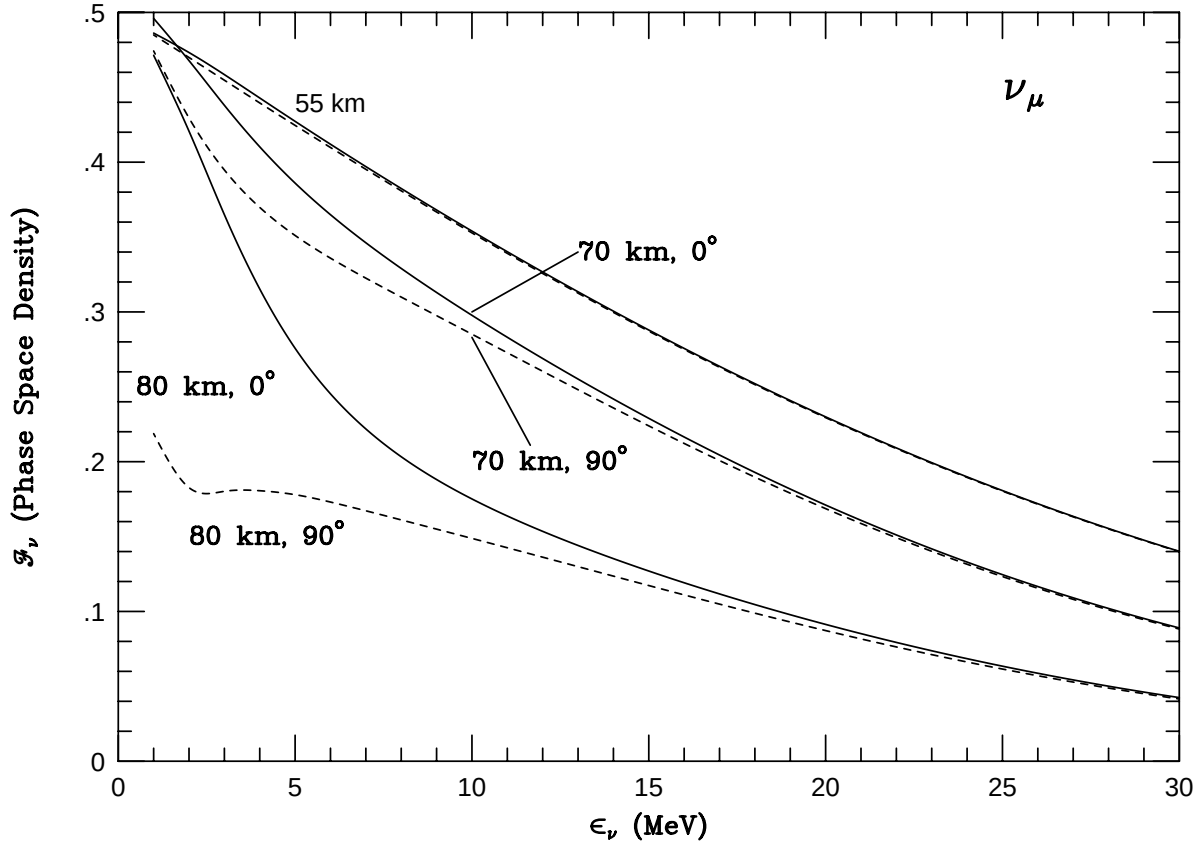

Fig. 25.— The phase–space density ($\mathcal{F}_\nu$) for the ν_μ neutrinos versus neutrino energy in MeV, at radii of 55, 70, and 80 km. The solid lines are for the forward direction and the dashed lines are for the transverse direction (at $\sim 90°$). At depth, and at lower energies, ν_μ neutrino degeneracy ($\mathcal{F}_\nu$) approaches 0.5, as expected for the situation with no net ν_μ lepton number and, hence, zero chemical potential.

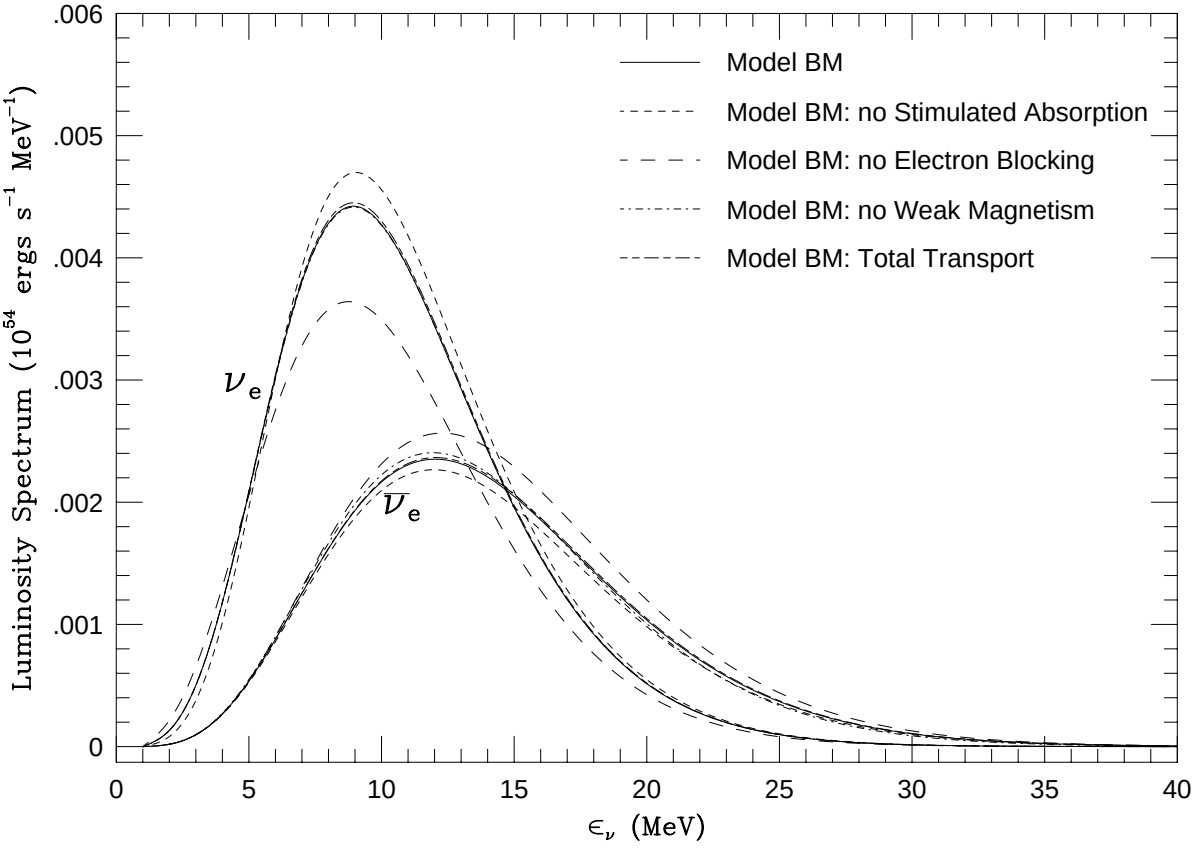

Fig. 26.— The emergent luminosity spectrum for both the ν_e and $\bar{\nu}_e$ neutrinos for our fiducial Model BM (solid line), compared with models without stimulated absorption (small–dashed line), e^- blocking (long–dashed line), or weak magnetism/recoil (dot–dashed line). Also included is a model for which the total scattering cross section is substituted for the transport cross section (short dash-long dash).

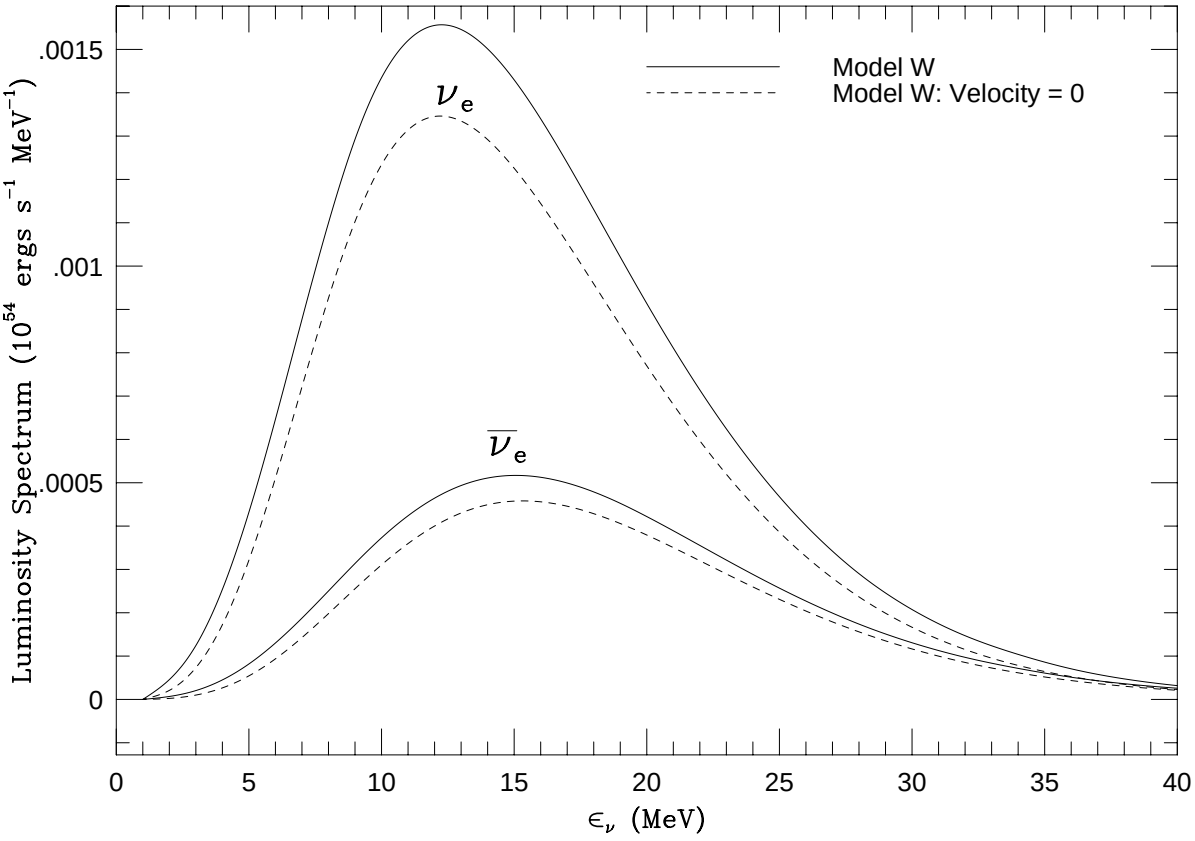

Fig. 27.— The emergent ν_e luminosity spectrum for the wind Model W with a velocity field (solid line) and without a velocity field (dashed line), versus energy in MeV. The velocity terms boost the spectrum that emerges from a protoneutron star with a wind by ∼15%.

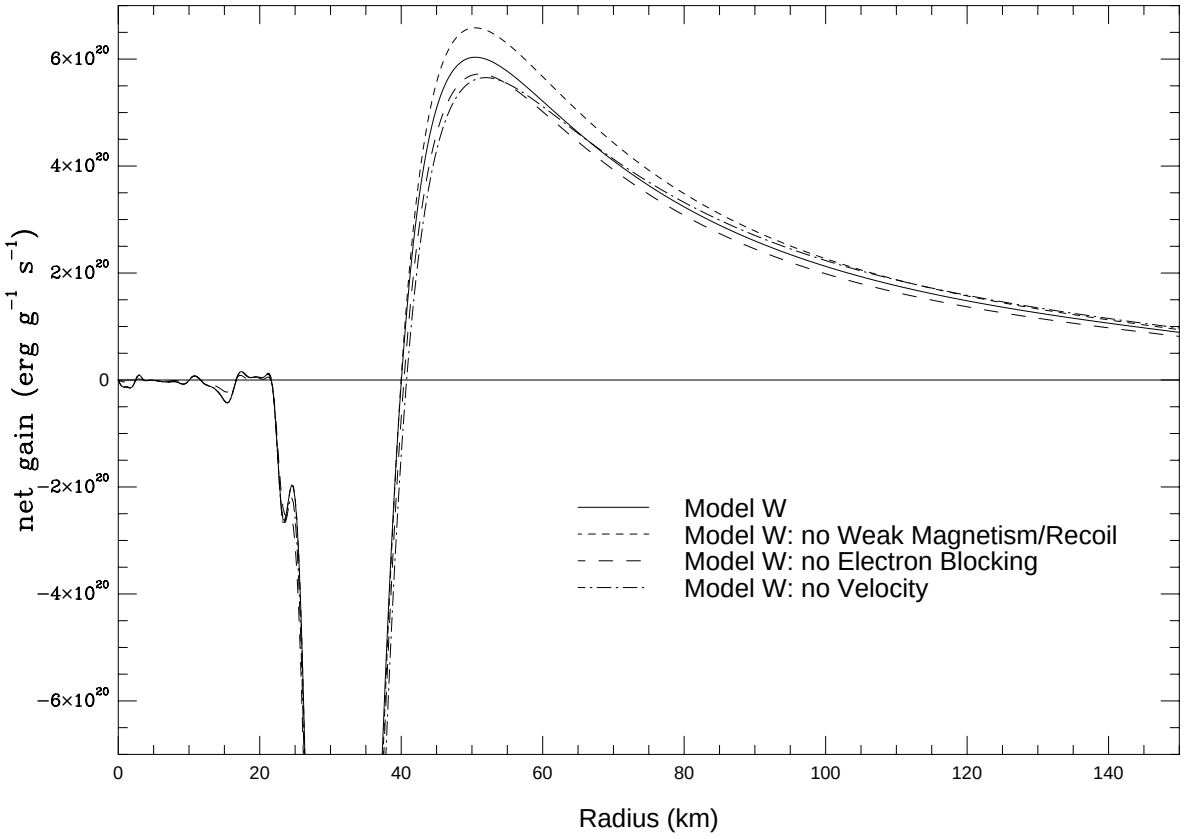

Fig. 28.— The net heating rate (net gain) versus radius (in km) for wind Model W. The fiducial model (solid) is compared with models for which either weak magnetism/recoil (short-dashed line) or e^- blocking (long–dashed line) is ignored. Also included is a model for which the velocities were set equal to zero (dot–dashed).

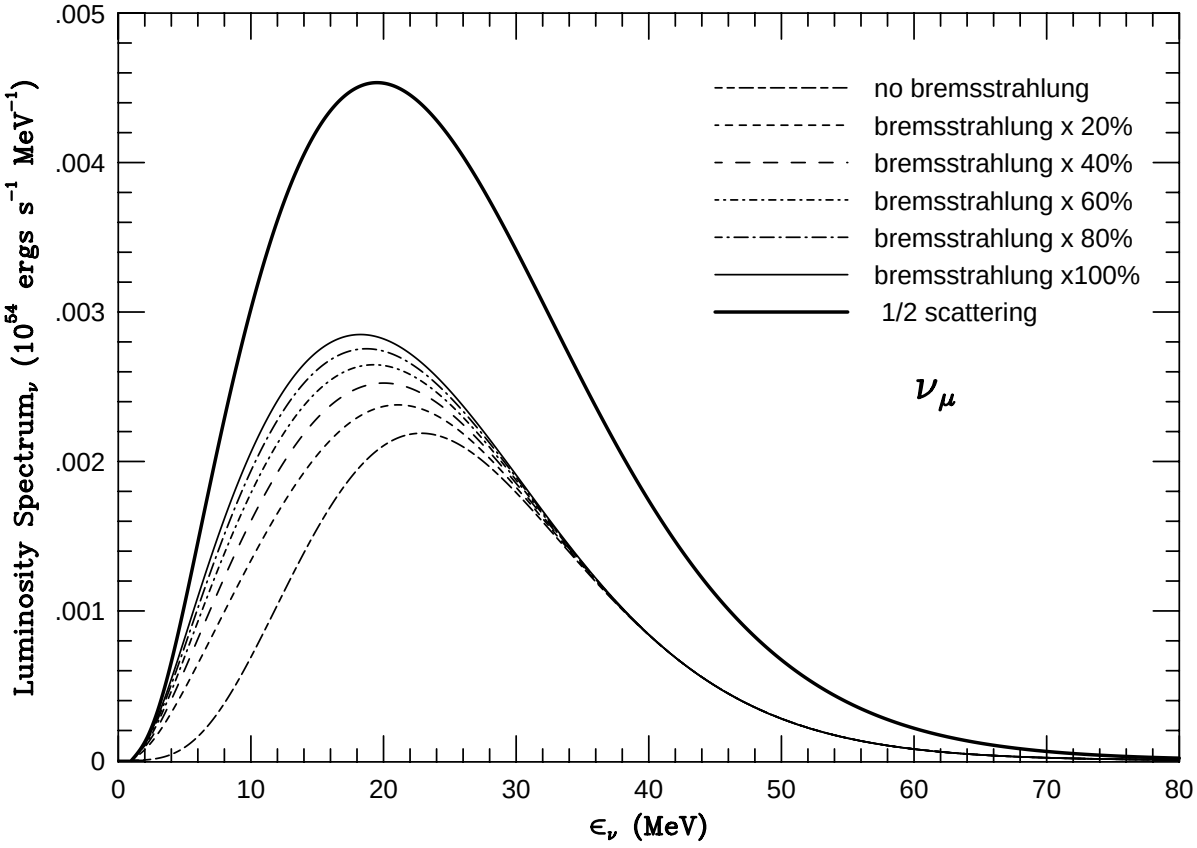

Fig. 29.— The emergent ν_μ luminosity spectra for Model BM for bremsstrahlung factors, ζ, of 0.0, 0.2, 0.4, 0.6, 0.8, and 1.0. Also included is the ν_μ spectrum with the ν_μ–nucleon scattering cross section artificially decreased by 50%.